

Scuola di Scienze
Dipartimento di Fisica e Astronomia
Corso di Laurea Magistrale in Fisica

**Emulation of neutrino-induced muon
tracks in a neutrino telescope using the
test-bench of the data acquisition system of
the KM3NeT.**

Relatore:
Prof.ssa Annarita Margiotta

Presentata da:
Francesco Filippini

Correlatore:
Dr. Tommaso Chiarusi

Abstract

Oggi l'astronomia multimessaggero offre l'opportunità di investigare, in un modo mai fatto prima, l'universo. In questo quadro l'astrofisica a neutrini e i conseguenti telescopi a neutrini forniscono uno sguardo privilegiato e complementare rispetto alle altre branche di osservazione e nel prossimo futuro permetteranno di gettare luce e di misurare, con estrema precisione, il flusso di neutrini di origine cosmica di alta energia. Questa tesi si sviluppa all'interno dell'esperimento KM3NeT, una rete di rivelatori in costruzione nelle acque abissali del Mar Mediterraneo, che raggiungerà le dimensioni finali di più di un km³ di acqua instrumentata. Nello specifico la tecnologia necessaria alla costruzione di questi detectors deve essere testata e validata in maniera molto accurata, data la completa inaccessibilità dei siti di installazione. Per questo motivo sono nati diversi laboratori, all'interno della collaborazione, che rappresentano un punto nodale per lo sviluppo, il mantenimento e i test di tutti gli apparati e la strumentazione distribuita in fondo al mare. Fra questi laboratori vi è la Bologna Common Infrastructure (BCI) test-bench, in cui è stata riprodotta l'elettronica e tutto il sistema di acquisizione dati di un'intera stringa di KM3NeT. Questa tesi è basata sul lavoro di sviluppo delle schede OctoPAES, in grado di emulare segnali di fotoni sui fotomoltiplicatori come se fossero stati generati dal passaggio di particelle reali, all'interno però di un ambiente controllato e accessibile come la BCI. Queste schede inoltre sono in grado di generare un flusso di dati manipolabile dall'esterno, capace quindi di evidenziare potenziali malfunzionamenti o punti critici dell'elettronica, del sistema di acquisizione dati e non solo.

Contents

Introduction	2
1 Neutrino astrophysics	4
1.1 Neutrino physics and interactions	5
1.1.1 Neutrino interactions	5
1.1.2 Neutrino oscillation	11
1.2 Cosmic rays and atmospheric neutrinos	13
1.2.1 Cosmic ray energy spectrum	14
1.2.2 Fermi acceleration mechanism	16
1.2.3 Acceleration mechanisms above the knee	19
1.2.4 GZK cut-off	20
1.2.5 Acceleration sites	21
1.2.6 Atmospheric neutrinos	23
1.3 Astrophysical neutrinos	25
1.3.1 Neutrino production mechanisms	25
1.3.2 Neutrino and gamma astronomy	27
1.3.3 Neutrino flux	27
1.3.4 State of the art of astrophysical neutrino detection	29
1.3.5 Gravitational wave in the multi-messenger scenario	31

2	Neutrino telescopes and KM3NeT	33
2.1	Detection principle	35
2.1.1	Cherenkov radiation	36
2.1.2	Light propagation	38
2.2	KM3NeT detector	38
2.2.1	Installation sites	39
2.2.2	Digital Optical Module (DOM)	41
2.2.3	Detection Unit (DU) and detector layout	44
2.3	Event signatures	46
2.3.1	Environmental background	50
2.3.2	Physical background	52
3	The Bologna Common Infrastructure test-bench for KM3NeT data acquisition system	54
3.1	Data Acquisition system	55
3.1.1	Control Unit	57
3.1.2	TriDAS	57
3.1.3	Quasi On-Line Analysis and Monitoring system	58
3.1.4	RAW DATA LAN	59
3.1.5	Data handling and timeslice	61
3.2	Algorithms for the event triggering	62
3.2.1	Muon Trigger and reconstruction algorithm	64
3.2.2	Shower trigger	67
3.3	BCI: experimental setup	69
3.4	OctoPAES	72
3.4.1	OctoPAES firmware and wiring topology	74
3.4.2	Online delay display tool	81

4	Emulating neutrino induced muon tracks with the OctoPAES boards	85
4.1	Micro-OOS issue	86
4.2	Muon emulation and MIF	90
4.2.1	MIF file	91
4.2.2	GUI for MIF creation	94
4.2.3	Time calibration	101
4.3	Characterisation of the micro-OOS issue at the BCI	104
4.4	Other developments: test with convolutional neural network	107
4.4.1	Regression on zenith angle for neutrino events	110
	Conclusions	116
5.1	Summary	116
5.2	Outlook	117

Introduction

Neutrino astronomy is the youngest branch of astroparticle physics whose aim is to detect neutrino fluxes predicted by various acceleration and propagation models for cosmic rays (CRs). Together with the study of gravitational waves, of CRs and with the detection of gamma-rays, it constitutes the so called *multi-messenger astronomy*. After 50 years since the proposal by Markov of exploiting deep-sea waters to detect cosmic neutrinos, IceCube neutrino telescope in the South Pole provided their first ever observation. These recent discoveries allowed to verify and put severe constraints on theoretical models and to assure the effectiveness of the experimental methodology used. The second generation of neutrino telescopes like KM3NeT, IceCube and GVD, under construction or development during these years, has the objective to identify, with a precision never had before, astrophysical sources able to produce high-energy neutrinos and to correlate their direction of flight with gamma-ray or gravitational wave counterpart. In particular, KM3NeT neutrino telescope will reach, in its final configuration, an instrumented volume greater than 1 km^3 , with hundred of thousands of optical sensors, becoming therefore the most sensitive high-energy neutrino telescope. In addition, being placed in the Northern hemisphere, it is able to look directly at the centre of our Galaxy, one of the most interesting and promising region where to find neutrino sources.

The thesis is organised as follows:

- the first chapter is focused on the explanation of the physical properties of neutrinos, of the CR spectrum and of the principal theoretical models today used to explain and predict upper bounds on neutrino fluxes. Also the recent IceCube observations are discussed;
- in the second chapter the detection principle used by neutrino telescopes to detect these elusive particles, the physical phenomena affecting the light propagation

and the principal constructive characteristics of the new KM3NeT detectors are exposed;

- in the third chapter the KM3NeT data acquisition system is described with particular attention to its peculiar design and to the trigger algorithms applied to filter the huge amount of data collected. Also, an important part is dedicated to the Bologna Common Infrastructure test-bench and to the introductory works made for the development of the OctoPAES boards;
- in the last chapter the principal objectives and results obtained within the work of this thesis are exposed: the study and development of the OctoPAES boards, the consequent evaluation of the micro Out Of Synchronisation (OOS) issue and the test of Deep Learning frameworks, under construction and development by the KM3NeT collaboration.

Chapter 1

Neutrino astrophysics

Neutrino astrophysics is a young discipline, born to extend the conventional astronomy, based on photons, with the detection of neutrinos, capable to bring completely new information on the source that generate them. During the previous century, great improvements in the survey of the sky came from the enlargement of the detectable electromagnetic spectrum towards the infrared region and with the study of radio emission of peculiar sources. Although these steps forward, that still today produce interesting pictures of the Universe, there are intrinsic limits within this type of observations due to the nature of the photon itself. In fact, it is impossible to observe directly the innermost structure of celestial objects, neither the galactic nuclei that are opaque to photons. Moreover starting at an energy of 10-15 TeV the photons start to interact with the Cosmic Microwave Background (CMB) causing the creation of electron-positron pair. In order to overcome these limits, the study of Cosmic Rays (CRs) and of neutrinos was undertaken, allowing to study the most energetic phenomena occurring in the Universe, through complementary information with respect to what is brought by photons. Furthermore neutrino properties make it a peculiar messenger capable to escape from densest environment without interacting with the Galactic and extra-Galactic magnetic fields. In this chapter the experimental and theoretical status of the high-energy as-

particle physics is summed up, with particular attention to neutrino properties and neutrino astronomy.

1.1 Neutrino physics and interactions

Neutrinos are elementary particles, with no electric charge and with spin=1/2. The existence of neutrinos was hypothesized, for the first time, by W. Pauli in 1930 to explain the spectrum of the electrons in the β -decay [1]. Then four years later, E. Fermi proposed a mathematical theory, in analogy with the electrodynamics (QED), capable to explain the β -decay, and renamed the particle, previously introduced by Pauli, as *neutrino*. Only about twenty years later, Reines and Cowan detected the first neutrinos, confirming therefore their existence [2]. Since then, many experimental efforts were carried out, and two further neutrino flavours have been discovered, named muon neutrino [3] and tau neutrino [4]. All neutrino flavours are described within the Standard Model (SM) of particle physics, where they are grouped into three families with the corresponding charged lepton: *electron* (e), *muon* (μ) and the *tau* (τ). In the SM neutrinos are assumed to be massless, but in order to explain the recent observation of neutrino oscillation [5], the existence of a mass for the neutrino field must be postulated.

1.1.1 Neutrino interactions

The neutrino interaction is described with impressive accuracy within the Standard Model: having electric and colour charge = 0, neutrinos interact only via weak interaction. The interaction term of the SM electroweak lagrangian for neutrinos can be

explicitly written as:

$$\mathcal{L}_{I,L}^{CC} + \mathcal{L}_{I,\nu}^{NC} = -\frac{g}{2\sqrt{2}} \left(j_{W,L}^\rho W_\rho + h.c. \right) - \frac{g}{2\cos\theta_W} j_{Z,\nu}^\rho Z_\rho \quad \text{with :} \quad (1.1)$$

$$j_{W,L}^\rho = 2 \sum_{\alpha=e,\mu,\tau} \bar{\nu}_{\alpha L} \gamma^\rho l_{\alpha L} = \sum_{\alpha=e,\mu,\tau} \bar{\nu}_\alpha \gamma^\rho (1 - \gamma^5) l_\alpha \quad (1.2)$$

$$j_{Z,\nu}^\rho = \sum_{\alpha=e,\mu,\tau} \bar{\nu}_{\alpha L} \gamma^\rho \nu_{\alpha L} = \frac{1}{2} \sum_{\alpha=e,\mu,\tau} \bar{\nu}_\alpha \gamma^\rho (1 - \gamma^5) \nu_\alpha \quad (1.3)$$

with $j_{W,L}^\rho$ and $j_{Z,\nu}^\rho$ the leptonic charged current and neutral current terms, ν_α and l_α the spinorial field for neutrinos and charged leptons and W_ρ and Z_ρ the two fields associated with the gauge bosons. Moreover the subscript L or explicitly writing the left-handed projector $\frac{(1-\gamma^5)}{2}$ in eq.(1.1) means that weak interaction is maximally parity violating [6], making interact only left-handed fermions and right-handed antifermions. For further details on SM and weak interaction see [7][8].

Neutrino-nucleon interaction

The interaction processes of neutrinos with ordinary matter are mainly divided into two categories: *Charged Current* (CC) and *Neutral Current* (NC), that can be described as follows:

$$\nu_l + X \rightarrow l^\pm + Y \quad (CC) \quad (1.4)$$

$$\nu_l + X \rightarrow \nu_l + Y \quad (NC) \quad (1.5)$$

with the exchange in the first case of a W^\pm gauge boson and in the second of a Z^0 gauge boson.

At this point the charged lepton (only in CC channel) and the hadrons, originated from the interaction, can generate an electromagnetic or an hadronic cascade (described in the next chapter).

Considering the generalised Feynman diagram shown in Fig.1.1, with particular at-

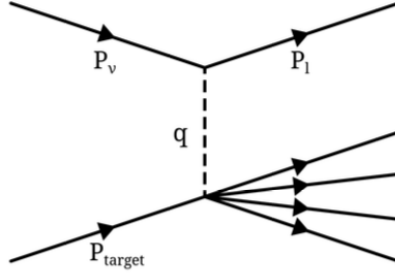


Figure 1.1: Feynman diagram of a generic neutrino-nucleon interaction, producing in the final state a neutral (NC) or a charged (CC) lepton. Attention paid to the kinematical variables. Figure taken from [9].

tention to the kinematics of the process, the following Lorentz invariants can be derived:

$$s = (p_\nu + p_{\text{target}})^2 \quad (\text{center of mass energy}), \quad (1.6)$$

$$Q^2 = -q^2 = -(p_\nu - p_l)^2 \quad (\text{four momentum transferred}), \quad (1.7)$$

$$y = \frac{q \cdot p_{\text{target}}}{p_\nu \cdot p_{\text{target}}} \quad (\text{inelasticity}), \quad (1.8)$$

$$x = \frac{Q^2}{2 \cdot p_{\text{target}} \cdot q} \quad (\text{Bjorken scaling variable}), \quad (1.9)$$

$$W^2 = (q + p_{\text{target}})^2 \quad (\text{invariant hadronic mass}) \quad (1.10)$$

In the lab frame, where the target is at rest, the inelasticity or *Bjorken* y can be rewritten in this way

$$y = \frac{E_\nu - E_l}{E_\nu} \quad (1.11)$$

putting in evidence the physical meaning of this variable: the fraction of neutrino energy transferred to the target. The neutrino-nucleon cross section can be now described in function of the two Bjorken invariants x and y :

$$\frac{d^2\sigma_{CC}}{dxdy} = \frac{2G_F^2 m E_\nu}{\pi} \left(\frac{M_W^2}{Q^2 + M_W^2} \right)^2 [x q(x, Q^2) + x \bar{q}(x, Q^2)(1 - y^2)] \quad (1.12)$$

$$\frac{d^2\sigma_{NC}}{dxdy} = \frac{G_F^2 m E_\nu}{2\pi} \left(\frac{M_Z^2}{Q^2 + M_Z^2} \right)^2 [x q(x, Q^2) + x \bar{q}(x, Q^2)(1 - y^2)] \quad (1.13)$$

where m is the target mass, $G_F \sim 1.16 \times 10^{-5} \text{ GeV}^{-2}$, and q and \bar{q} are the structure functions for quarks and anti-quarks. Integrating out the cross sections shown in the previous equations, for neutrino energies above 100 GeV, the following ratio is obtained:

$$\frac{\sigma_{CC}}{\sigma_{CC} + \sigma_{NC}} \approx 0.7 \quad (1.14)$$

This means that the charged current interactions represents around the 70 % of all the neutrino-nucleon interactions.

An interesting and useful approximation is the one in which the target can be considered to be massless. At sufficiently high energies, this is valid for modeling deep inelastic scattering, where the neutrino scatter off a free constituent quark. At the same time, assuming a small four momentum transferred compared to W^\pm mass and a large centre of mass energy s respect to the mass m_l of the lepton, the boson propagator effects and production thresholds, on the cross section calculations, can be neglected. Integrating out the Bjorken variables from eq.(1.13), in the case of neutrino-fermion (equivalent to antineutrino-antifermion) charged current, the differential and total cross section takes this form:

$$\frac{d\sigma_{CC}(\nu f)}{d\Omega} = \frac{G_F^2 s}{4\pi^2}, \quad \sigma_{CC}(\nu f) = \frac{G_F^2 s}{\pi} \quad (1.15)$$

From eq.(1.15) three important observations can be derived:

- cross section depends linearly on s . If we consider the rest frame of the target, with mass m , the relation $s = m(m + 2E_\nu)$ holds, so that the cross section increases linearly with neutrino energy (E_ν);
- the cross section grows linearly with the mass of the target m ;
- the cross section doesn't depend on the neutrino-target scattering angle in the centre of mass frame.

A similar evaluation can be made for neutrino-antifermion (equivalent to antineutrino-fermion) charged current interaction, being careful to the initial helicity states. Due to weak interaction properties we have an initial state with total angular momentum $J = 1$, leading to a preference direction due to angular momentum conservation along the interaction axis. The cross section for the process $\nu_l + \bar{f}$, respect to eq.(1.15), includes an extra factor $[1 + \cos(\theta^*)]^2$. In the centre of mass frame the inelasticity y is connected to θ^* with the relation $y = [1 - \cos(\theta^*)]/2$. The differential and total cross sections can be now rewritten in this form:

$$\frac{d\sigma_{CC}(\nu\bar{f})}{d\Omega} = \frac{G_F^2 s}{16\pi^2} [1 - \cos(\theta^*)]^2, \quad \frac{d\sigma_{CC}(\nu\bar{f})}{dy} = \frac{G_F^2 s}{\pi} (1 - y)^2, \quad \sigma_{CC}(\nu\bar{f}) = \frac{G_F^2 s}{3\pi} \quad (1.16)$$

Comparing the total cross sections for $\nu + f$ and $\nu + \bar{f}$ we can see that the second process is suppressed by a factor 3, only for helicity considerations. In Fig.1.2 is shown the behaviour of the total cross section for neutrino-nucleon and antineutrino-nucleon at high energies, in which the dominant process is the deep inelastic scattering [10].

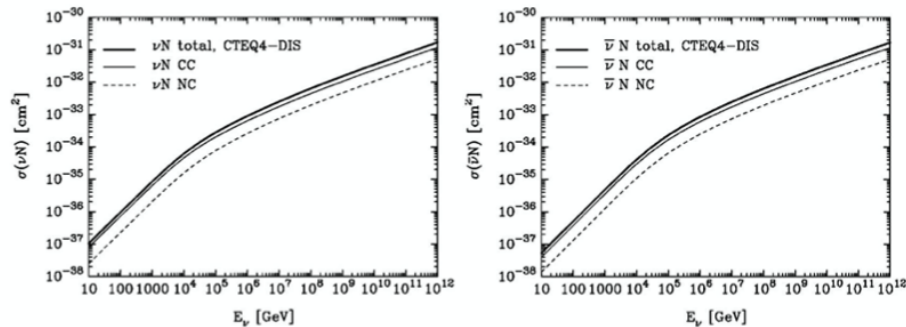


Figure 1.2: **left:** neutrino-nucleon cross section; **right:** antineutrino-nucleon cross section. In both, total cross section (bold line), and the single components: CC (solid line) and NC (dashed line) are shown. Figure taken from [10].

Neutrino-electron interaction

As analysed above, the total cross section is linearly dependent on the mass of the target. This produces a suppression of three orders of magnitude for the neutrino-electron process with respect to the neutrino-nucleon one. This is a general behaviour over a wide energy range, except in a precise interval, $E_\nu = 5.7 \div 7.0$ PeV, where it presents the resonance production of a real W^- boson, as in the process: $\bar{\nu}_e + e^- \rightarrow W^-$ [10]. The peak of the resonance, as shown in Fig.1.3 is at an energy around $E_\nu \sim 6.3$ PeV, and is called *Glashow resonance*. This process was postulated in the late 1960s

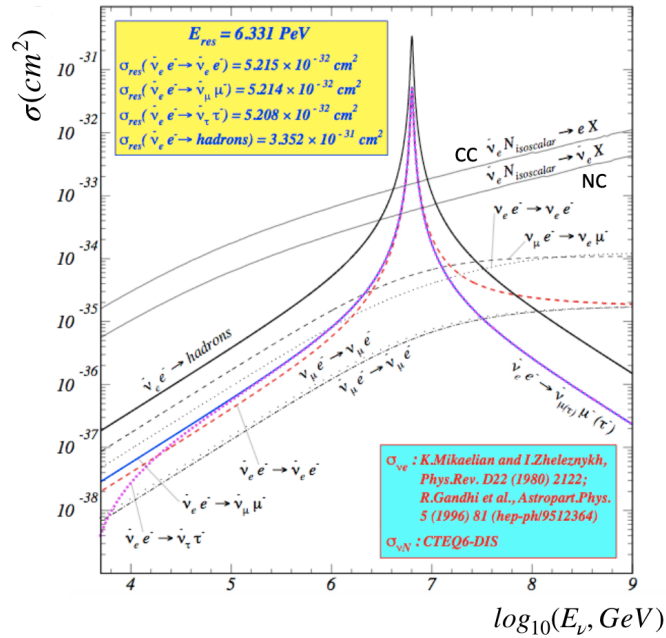


Figure 1.3: The glashow resonance, peaked at an energy around 6.3 PeV.

but still remains unobserved. The biggest challenge is the building of detectors capable to reveal neutrinos at such high energies. Nowadays with the construction of neutrino telescopes, capable to detect high-energy astrophysical neutrinos, observation becomes feasible. Recent studies by the KM3NeT collaboration show what is the sensitivity for

the detection of the process with KM3NeT-ARCA telescope, with one year of observation [11].

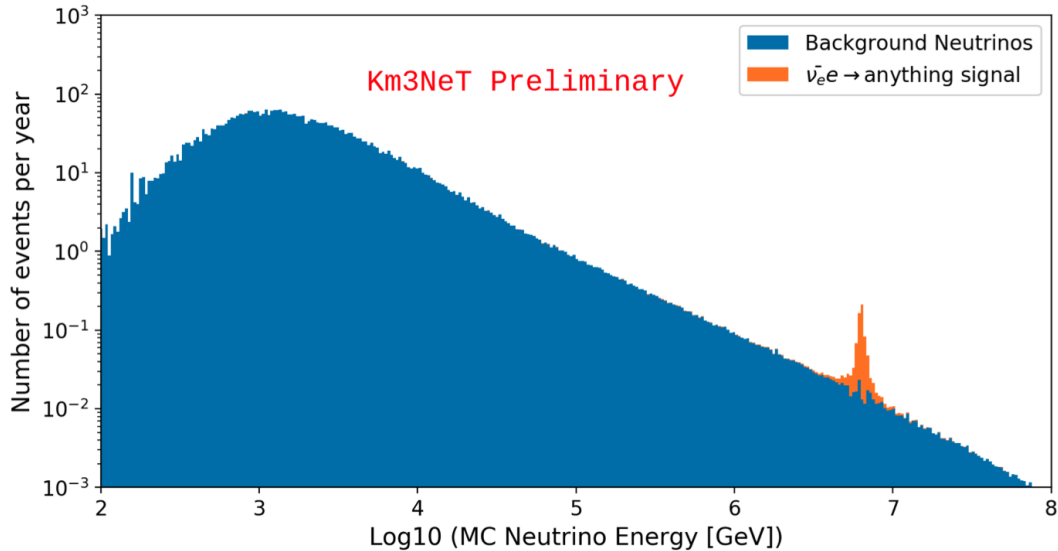


Figure 1.4: Expected event rate in one building block of KM3NeT-ARCA after one year of observation. The orange peak corresponds to the Glashow resonance events only. Blue histogram contains all other neutrino interactions in the detector. Figure taken from [11].

1.1.2 Neutrino oscillation

In this section I will briefly describe the neutrino oscillation phenomenon, and its implications on neutrino astronomy. The oscillation of the neutrino flavour originates from the fact that flavour eigenstates do not coincide with mass eigenstates. In fact pure flavour eigenstates, originated from weak interaction processes, are mixture of at least three mass eigenstates with unequal mass. This difference will lead, during the propagation in vacuum, to a periodic change in the probability that a flavour eigenstate α will be detected as another flavour eigenstate β , with $\alpha \neq \beta$. The following section is inspired by [12].

Three family formalism

A neutrino with flavour α and momentum \vec{p} , created in CC or NC processes, can be described as follows:

$$|\nu_\alpha\rangle = \sum_k U_{\alpha k}^* |\nu_k\rangle, \quad \alpha = e, \mu, \tau \quad (1.17)$$

where $|\nu_k\rangle$ are the orthonormal massive neutrino states and $U_{\alpha k}$ is the mixing matrix, also known as *Pontecorvo-Maki-Nakagawa-Sakata* (PMNS) matrix [13][14]. The matrix U can be parametrized by 3 mixing angles θ_{ij} and a complex phase δ , encoding the possible CP violation (recent results on δ value, reported by T2K experiment can be found at [15]):

$$U = \begin{pmatrix} 1 & 0 & 0 \\ 0 & c_{23} & s_{23} \\ 0 & -s_{23} & c_{23} \end{pmatrix} \begin{pmatrix} c_{13} & 0 & e^{i\delta} s_{13} \\ 0 & 1 & 0 \\ -e^{i\delta} s_{13} & 0 & c_{13} \end{pmatrix} \begin{pmatrix} c_{12} & s_{12} & 0 \\ -s_{12} & c_{12} & 0 \\ 0 & 0 & 1 \end{pmatrix} \quad (1.18)$$

The unitarity of the mixing matrix U transposes the mass eigenstate orthonormality property also to the flavour eigenstates:

$$\langle \nu_\alpha | \nu_\beta \rangle = \delta_{\alpha\beta} \quad (1.19)$$

In eq.(1.17) it is not set an upper limit on the number of massive neutrino states. The number of active flavour neutrinos is three, so the number of massive neutrino states must be greater or equal to three. However, the massive neutrino states are eigenstates of the Hamiltonian \mathcal{H} , with eigenvalue E_k , with energy given by the usual relativistic dispersion relation. Therefore the Schrödinger equation can be written:

$$i \frac{d}{dt} |\nu_k(t)\rangle = \mathcal{H} |\nu_k(t)\rangle \quad (1.20)$$

that gives us, as result, the usual evolution in time of the neutrino mass eigenstates as plane wave. At this point the time evolution of flavour eigenstates is given by:

$$|\nu_\alpha(t)\rangle = \sum_k U_{\alpha k}^* e^{-iE_k t} |\nu_k(t)\rangle \quad (1.21)$$

Considering the initial condition $|\nu_\alpha(t=0)\rangle = |\nu_\alpha\rangle$, and eq.(1.17), the evolved flavour eigenstate, at a generic time t in function of the initial flavour eigenstate, is given as follows:

$$|\nu_\alpha(t)\rangle = \sum_{\beta=e,\mu,\tau} \left(\sum_k U_{\alpha k}^* e^{-iE_k t} U_{\beta k} \right) |\nu_\beta\rangle \quad (1.22)$$

The probability of the transition $\nu_\alpha \rightarrow \nu_\beta$, as a function of time can be written in this form:

$$P_{\nu_\alpha \rightarrow \nu_\beta}(t) = |A_{\nu_\alpha \rightarrow \nu_\beta}|^2 = \sum_{k,j} U_{\alpha k}^* U_{\beta k} U_{\alpha j} U_{\beta j}^* e^{-i(E_k - E_j)t} \quad (1.23)$$

For ultra-relativistic neutrinos the relation $E_k - E_j \sim \frac{\Delta m_{kj}^2}{2E}$ holds, and the propagation time can be replaced with the distance between the source and the detector L ($t = L$ in natural units) leading to:

$$P_{\nu_\alpha \rightarrow \nu_\beta}(L, E) = \sum_{k,j} U_{\alpha k}^* U_{\beta k} U_{\alpha j} U_{\beta j}^* \exp\left(-i \frac{\Delta m_{kj}^2 L}{2E}\right) \quad (1.24)$$

The amplitude of the oscillation is specified by the elements of the mixing matrix, while the phase of the oscillation is determined by the square mass differences Δm_{kj}^2 . The neutrino oscillation produces a change in the ratio of neutrino flavours, when propagates towards the detector. In fact neutrinos produced in astrophysical environments, from π or K decay have a ratio $\nu_e : \nu_\mu : \nu_\tau = 1 : 2 : 0$ at the source, which is changed during the path. At Earth is expected to be $\nu_e : \nu_\mu : \nu_\tau = 1 : 1 : 1$.

1.2 Cosmic rays and atmospheric neutrinos

The Cosmic Rays (CRs) are an isotropic flux of protons and heavier nuclei hitting the upper shell of the Earth atmosphere. The name ‘‘Cosmic Rays’’ was used for the first time by Robert Millikan in 1925, after several studies and experiments carried out, since the beginning of the century, by V.F. Hess. Although the study and knowledge on

CRs have advanced a lot in the last century, there are however still some open questions on the nature and the source that generates these energetic particles. In fact, being mainly composed by protons, having an electric charge = +1, they interact with the Galactic and extra-Galactic magnetic fields, making back-propagating the particle to its source impossible. Therefore, during the years, other methods and other messengers, like neutrinos, were studied in order to put constraints and gather some complementary information on the source that generate them.

1.2.1 Cosmic ray energy spectrum

The energy spectrum of primary cosmic rays, shown in Fig.1.5, measured through direct and indirect techniques spans from $\sim 10^9$ eV to more than 10^{20} eV, is of non-thermal origin and follows a broken power law [16]:

$$\left[\frac{dN_P}{dE} \right]_{obs} = K E^{-\alpha} \quad (cm^{-2} sr^{-1} s^{-1} GeV^{-1}) \quad (1.25)$$

Fitting the experimental points with the power law written above, we obtain $\alpha = 2.7$ for energies below 3×10^{15} eV. Above this value, the spectral index become $\alpha = 3.1$: this change in spectral index is also known as *knee*. At energies of the order of 10^{19} eV, the spectrum flatten again, reaching an index $\alpha = 2.7$ and this feature is called *ankle*. The acceleration of CRs and the consequent spectrum measured at Earth can be explained through different models and acceleration mechanisms: till the knee the longest-established model is the *Fermi acceleration mechanism*, discussed in the next section. There are instead still lots of uncertainties on the acceleration mechanisms at energies between 10^{15} eV and 10^{19} eV. After the ankle, considering the energy of the CR and the mean value of the Galactic magnetic field $\langle B \rangle \sim 4 \mu G$, the Larmor radius can be evaluated and compared to the longitudinal and transversal dimensions of our Galaxy, reaching the conclusion that this part of the spectrum has an extra-Galactic origin. Simulated trajectories of CRs during their propagation in our Galaxy

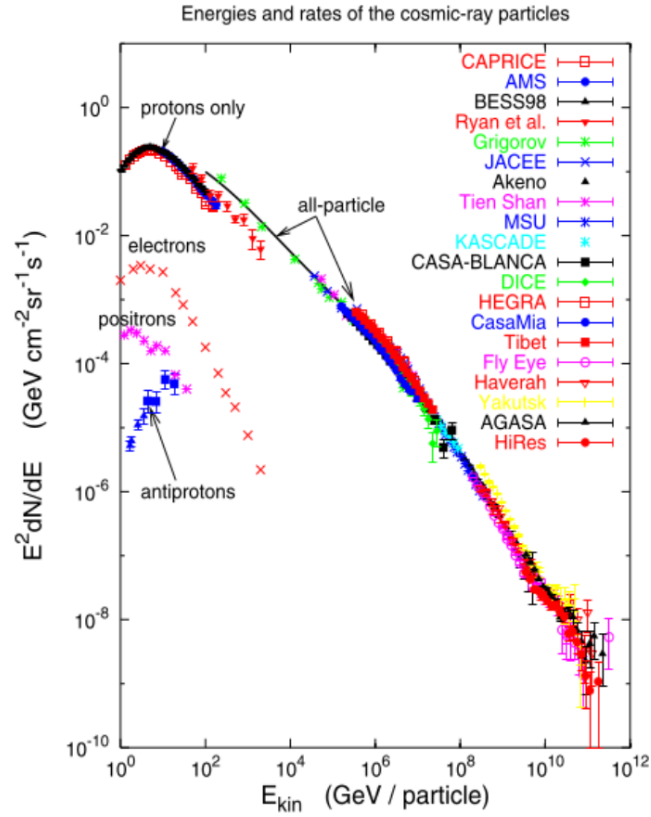


Figure 1.5: CRs differential energy spectrum, measured from multiple experiments. Note that the spectrum is remarkable continuous over the whole energy interval. The black solid line represents a E^{-3} spectrum. Figure taken from [17]

are shown in Fig.1.6 for different CR energies. Up to energies of 10^{14} eV, the CR spectrum is directly measured through balloons or satellites, providing also relevant information about the chemical composition of primary CRs. These measurements show that CRs are composed by $\sim 90\%$ of protons, $\sim 9\%$ of helium nuclei and $\sim 1\%$ of heavier nuclei. Above $\sim 10^{14}$ eV, CR measurements are only accessible from ground detectors, capable to instrument a large area and reveal secondary particles contained in the shower generated by the interaction of primary CRs with the nuclei in the atmosphere. The difficulties related to these indirect measurements produce still some uncertainties on the precise

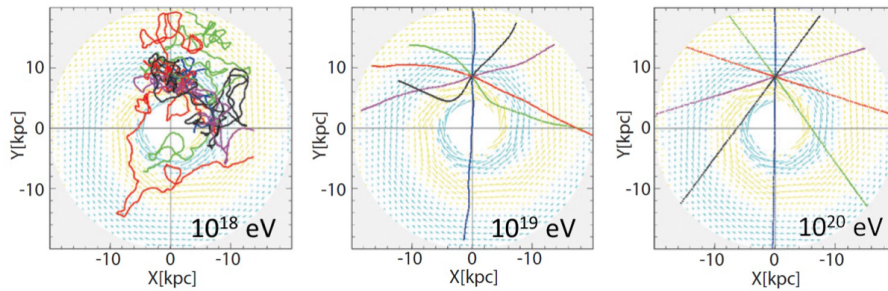


Figure 1.6: Simulated trajectory of CRs in the Galactic magnetic field. The three different energy regimes are chosen to put in evidence how CRs at energies $\sim 10^{19}$ eV travel along almost straight lines and are not trapped inside the galaxy.

determination of the chemical composition of CRs. For this reason in Fig.1.5 the CR spectrum is summed over all the possible mass numbers of primary CRs, resulting in an *all-particle* energy spectrum.

The content of the next section is get inspired by [18].

1.2.2 Fermi acceleration mechanism

The Fermi acceleration mechanism, formulated for the first time by E. Fermi in 1949 (second-order Fermi mechanism) [19], and corrected in 1954 (first-order Fermi mechanism), is the most accredited model to explain the acceleration of primary CRs till the knee. It explains the acceleration of charged particles in regions with very strong inhomogeneous magnetic fields. The idea at the base of the model can be easily illustrated using a toy model: two approaching trains. If a ball is thrown from the train B, moving with velocity V towards train A, at a speed v in the rest frame of the train B, the speed of the ball in laboratory frame will be $v_1 = v + V$ and $v_1^A = v + 2V$ in the frame of train A. If the collision is assumed to be elastic, the ball will bounce back with a velocity in the laboratory frame of $v_2 = v + 3V$. Considering the gain in each collision to be proportional to the train velocity V , if the process last long enough, the ball could reach

very high energies. Considering now protons or nuclei bouncing back and forth between two consecutive shock waves, originated in environments of disruptive events like stellar gravitational collapses, the similarity with the toy model exposed above can be caught.

Considering a relativistic regime, Lorentz transformations need to be applied to go from a reference frame S, the one of the observer, to the reference S', the one in which the shock wave or the magnetised cloud is at rest. Applying the transformations iteratively, for each collision, the final energy of the particle in the observer frame can be written as:

$$E^* \sim \left(1 + 2 \frac{Uv}{c^2} \cos\theta + 2 \frac{U^2}{c^2} \right) \cdot E \quad (1.26)$$

where U is the velocity of the cloud in S frame. The second term is equal to zero when averaged over all the possible directions. Furthermore energy is gained ($\cos\theta > 0$) for *head-on* collisions and lost for *catching* collisions: in this case the energy gained $\Delta E \propto (U/c)^2$ (second-order Fermi mechanism). Instead if it is assumed an astrophysical environment in which only head-on collisions occur, the quadratic term in U can be neglected, being $U/c \ll 1$, and approximate $v \sim c$ being in a ultra-relativistic regime. Now averaging the $\cos\theta$ over the range $[-\pi/2, \pi/2]$ in which only head-on collisions occur, we obtain:

$$\langle E^* \rangle = \left(1 + \frac{4U}{3c} \right) \langle E \rangle \equiv \mathcal{B} \langle E \rangle \quad (1.27)$$

$$\langle \Delta E \rangle = \left(\frac{4U}{3c} \right) \langle E \rangle \equiv \eta \langle E \rangle \quad (1.28)$$

Recollecting now the power law extracted experimentally from the CR spectrum, we need to consider also another factor: P_{esc} representing the possibility that, after a collision, the particle escapes the acceleration region, making it lose the successive iterations. If the mechanism is *efficient*, the P_{esc} is small. The probability that a particle remains inside the acceleration region after k collisions is $(1-P_{\text{esc}})^k$, and starting with N_0 particles with

initial energy E_0 , after k collisions there will be:

$$N = N_0 P^k \quad \text{particles with energy} \geq E = E_0 \mathcal{B}^k \quad (1.29)$$

Removing the k parameter from previous equation:

$$\frac{\ln(N/N_0)}{\ln(E/E_0)} = \frac{\ln P}{\ln \mathcal{B}} \quad (1.30)$$

the power law required is obtained:

$$\frac{N(\geq E)}{N_0} = \left(\frac{E}{E_0} \right)^{\ln P / \ln \mathcal{B}} \quad (1.31)$$

Supernova remnants (SNR) are the most accredited sites of acceleration of CRs in the region up to the knee. Applying the Fermi mechanism to this type of sources, it predicts a spectral index $\alpha = 2$ and fits correctly the energy power of 5×10^{40} erg/s required to accelerate Galactic CRs till the knee. The apparent tension with the spectral index measured from the CR spectrum ($\alpha = 2.7$) can be solved considering the Galactic diffusion of CRs, explained in the so called *leaky box* model [20]. Fig.1.6 shows charged CRs confined by Galactic magnetic fields, having a small probability to escape from the Galaxy itself. Increasing CR energy, the gyromagnetic or Larmor radius will increase, producing a larger probability for the CR to escape. Therefore an energy-dependent diffusion probability P can be defined, and measured experimentally through the ratio between light isotopes (Li, Be, B). It was found $P(E) \propto E^{\alpha_D}$, with $\alpha_D = 0.6$. The final differential flux of CRs at source is:

$$\left[\frac{dN_P}{dE} \right]_{source} \propto \left[\frac{dN_P}{dE} \right]_{obs} \cdot P(E) \propto E^{-\alpha} \cdot E^{\alpha_D} \propto E^{-\alpha_{CR}} \quad (1.32)$$

There is however some uncertainties on the nature of the knee in the CR spectrum. Some models lead back to astrophysical reasons, and to a dependence of the maximum obtainable energy in the acceleration sites on the nucleus charge Ze . This produces a different cut-off for every nucleus type, resulting in a proton-rich spectrum before the knee, and iron-rich after.

1.2.3 Acceleration mechanisms above the knee

The Fermi mechanism and SNR models can explain the CR flux till 10^{16} eV, but there is no preferred models for explaining the acceleration of CRs till 10^{19} eV. The idea is centred on the possibility, for already accelerated CRs, to suffer an additional acceleration due to, for example, neutron star strong variable magnetic field. In fact, in astrophysical environments the matter is in the form of plasma and no static electric fields can be generated. However, thanks to Faraday's law, variable magnetic fields can produce induced electric fields capable to accelerate charged particles. From simple dimensional arguments, the maximum obtainable energy from a pulsar¹ can be derived [18]:

$$\frac{\mathcal{E}}{R_{\text{pulsar}}} = \frac{1}{c} \frac{dB}{dt}, \quad (1.33)$$

$$E^{\text{max}} = \int Ze\mathcal{E}dx = \int Ze \frac{R_{\text{pulsar}}}{c} \frac{dx}{dt} dB = ZeR_{\text{pulsar}} B \frac{\omega_{\text{pulsar}} R_{\text{pulsar}}}{c} \quad (1.34)$$

Replacing the estimated values for the pulsar angular velocity ω_{pulsar} and radius R_{pulsar} , we obtain:

$$E^{\text{max}} \sim 5 \times 10^6 \text{erg} \sim 3 \times 10^{18} \text{eV} \quad (1.35)$$

Even if a small part of the total rotational energy of a single pulsar can be used to generate the entire power required from CR flux in the energy range knee- 10^{18} eV, theoretical details on the mechanisms are still not known. Another model that tries to explain the acceleration of CRs in this energy range exploits binary systems and still huge variable magnetic fields. These fields are produced by the huge amount of ionised

¹Pulsar is a rotating neutron star that emits a beam of electromagnetic radiation, typically along its magnetic axis. From simple arguments like angular momentum conservation, we can derive typical angular velocity and magnetic field of this object: $\omega_{\text{pulsar}} = 12\,500$ rad/s, $B_{\text{pulsar}} \sim 10^{12}$ G. Nowadays more than 2600 pulsar are known.

matter that falls from one object to the other, transforming in this case gravitational energy into electromagnetic energy and then in acceleration of charged particles.

1.2.4 GZK cut-off

With the discovery of the *Cosmic Microwave Background*(CMB), in 1966, independently G. Zatsepin, V. Kuz'min,[21] and K. Greisen [22] hypothesised the suppression of the Ultra High Energy Cosmic Rays (UHECRs) flux, due to the resonant production of pions in the interaction of protons with the CMB, through the following processes:

$$p^+ + \gamma_{cmb} \rightarrow \Delta^+ \rightarrow n + \pi^+ \quad (1.36)$$

$$\Delta^+ \rightarrow p + \pi^0 \quad (1.37)$$

$$\Delta^+ \rightarrow p^+ + \gamma \quad (1.38)$$

The neutral pions decay into gammas, while the charged ones decay mainly into $\mu^+\nu$. The decay of the neutron into a $p e \bar{\nu}_e$ produces, in all the final states, a proton with reduced energy due to the simultaneous pion production. What is expected therefore, is the suppression of the proton flux for energies above $E \sim 5 \cdot 10^{19}$ eV, value obtained from kinematics considerations. This suppression is also known as *GZK-cutoff*. Also the *energy loss length* $l_{p\gamma}$ can be estimated:

$$l_{p\gamma} = \frac{1}{\langle y \sigma_{p\gamma} n_\gamma \rangle} = \frac{1}{0.1 \cdot 250 \times 10^{-30} \cdot 400} = 10^{26} cm = 30 Mpc \quad (1.39)$$

where y is the Bjorken variable, introduced in the previous section. All protons originated at distances larger than ~ 30 Mpc from the Earth, are energy suppressed due to this effect. The estimate of the chemical composition of CRs, even at such high energies, is fundamental to confirm the existence of the GZK cut-off: in fact for heavier nuclei, with mass number A and energy E , the resonance production occurs through the interaction of a nucleon of energy E/A within the nucleus with the CMB. The threshold energy for heavier nuclei is therefore greater by a factor A . The Pierre Auger Observatory (PAO) has

already reported some interesting results [23] that shed some light on the composition of CRs in the most energetic part of their spectrum, but better resolution and improvements are expected in the next future.

1.2.5 Acceleration sites

Nowadays we know several sites where the acceleration of primary CRs may occur. In the following some are listed [16]:

- Supernovae Remnants (SNR): these are the most accredited sites responsible for the acceleration of CRs up to the knee, through Fermi mechanism. At the beginning of the collapse of a *core-collapse* or type II supernova, the reaction of electron capture on protons inside Fe nuclei is energetically favoured, producing neutron-rich nuclei in the core of the collapsing star. Some of the nuclei decay through β -decay producing a large fraction of $\bar{\nu}_e$. These particles are trapped inside the star due to high density reached in the process. When the core of the star reaches the nuclear density ($\rho \approx 10^{14}$ g/cm³) the in-falling material bounces back, producing a shock wave that triggers the supernova explosion. The nascent remnant will evolve into a neutron star or into a black hole, depending on the mass of the progenitor, above or below ~ 25 solar masses. $\bar{\nu}_e$ produced in the early stages are now capable to escape, causing the *neutrino burst*. 99% of the gravitational energy (3×10^{53} erg) is carried away by neutrinos, and only the remaining 1% is subdivided among photons and kinetic energy transferred to the expanding material, resulting however to be the perfect location for the acceleration of CRs. Most of the neutrinos are emitted with a thermal spectrum, with a mean energy around 15 MeV. The energetic balance is one of the most important arguments as proof of the acceleration mechanism in this type of sources. In fact considering the kinetic energy emitted ($\sim 10^{51}$ erg) and the number of observed SN explosions ($\sim 3/\text{century}$) we obtain an emission power in the Galaxy of $\sim 10^{40}$

erg/s, comparable to the power lost by the Galaxy itself through propagation and escape of CRs, resulting therefore in a stationary condition. Recent observations in gamma-ray astronomy by HESS collaboration [24], show strong evidence and also morphological characterisation of the production of gamma-rays in the SNR named RX J1713.7–3946;

- Pulsar wind nebulae (PWNe): also called Crab-like remnants, it is a SNR that differs from the previous one because a pulsar is present in the centre blowing winds and jets of material in the surrounding nebula. The radio, X and optical observations suggest an origin of the electromagnetic component through synchrotron radiation, even if an hadronic origin, with subsequent neutrino emission, is not still discarded. The neutrino flux calculated, thanks to the constraints imposed by gamma observations, for this type of sources can be detected by a km³ neutrino telescope;
- Microquasar: they are binary systems, emitting jets of relativistic particles revealed in the radio band. They result morphologically similar to AGN (see in the following) and are generally formed by a black hole and by an orbiting star that donates the material for the jets. They are considered to accelerate particles up to $\sim 10^{16}$ eV.

While the previous sources are typically acceleration sites within our Galaxy, the most energetic part of the CR spectrum seems to have an extra-Galactic origin. The most promising sources in this region of the spectrum therefore are:

- Active Galactic Nuclei (AGN): with this name it is denoted a particular class of galaxy, in which the central core emits jets of material, with a power of the order of $10^{42} \div 10^{43}$ erg/s. The first observation of these objects was made by the astrophysicist Carl Seyfert in 1943. The most accredited model nowadays foresees a supermassive black hole ($10^6 - 10^9$ solar masses) as central engine, with a

surrounding toroidal accretion disk. The ionised in-falling matter transforms the gravitational energy into strong magnetic fields that interact with the matter in the accretion disk, producing the characteristic jets. The estimate luminosity of this type of objects is 10^{46} erg/s. A particular class of AGN is called *blazars* which have their jet axes aligned with the observer direction;

- Gamma Ray Bursts (GRBs): they are flashes of γ -rays that last typically from milliseconds to tens of seconds. They are in fact classified according to their duration into long and short GRBs (threshold value is 2 s), and most of the energy is carried out by photons in MeV range. The origin of these GRBs is likely the collapse of massive stars to black hole or, thanks to recent observations, the merger of neutron stars or merger of black holes [25]. GRBs produce also optical, X-ray and radio emission after the initial burst, called *afterglow*, whose X-ray component was revealed for the first time by the Beppo-Sax satellite in 1997 [26]. The typical fluency for this type of objects is $10^{-7} \div 10^{-4}$ erg/cm², producing therefore the most energetic events in the cosmos, but there are still some uncertainties on the angular emission of the light, being isotropic or collimated into two jets. One of the most accredited model for the inner mechanism assumes that a *fireball* expands with ultra-relativistic velocities ($\Gamma \sim 10^{2.5}$) powered by radiation pressure. The accelerated protons lose energy through the photo-meson interaction with the surrounding ambient photons.

1.2.6 Atmospheric neutrinos

The interaction of primary CRs with the nuclei in the atmosphere produces lots of particles with the following reaction:

$$p + \mathcal{N} \rightarrow \pi^\pm(K^\pm) + \text{others} \quad (1.40)$$

with \mathcal{N} generic nucleus. The charged pions have a lifetime $\tau \sim 10^{-8}$ s and decay:

$$\pi^+(K^+) \rightarrow \mu^+ + \nu_\mu \quad (1.41)$$

In turn the muon decays in $\sim 10^{-6}$ s:

$$\mu^+ \rightarrow e^+ + \bar{\nu}_\mu + \nu_e \quad (1.42)$$

The proton interaction with the nuclei in the atmosphere produces, with quite the same probability, the following process:

$$p + \mathcal{N} \rightarrow \pi^0 + \text{others} \quad (1.43)$$

$$\pi^0 \rightarrow \gamma + \gamma \quad (1.44)$$

with a lifetime for the π^0 of the order of 10^{-16} s. Neutrinos produced in the shower are called *atmospheric neutrinos* and muons, analogously, *atmospheric muons*. These particles are the most abundant one at sea level due to their small energy loss and their relative long lifetime. They are in fact the only component, among the particles generated in the shower, that can traverse several meters of water equivalent, producing signals in a neutrino telescope. In particular, atmospheric muons produce the most abundant signal measured in underwater neutrino telescopes.

The complete description of the cascade development, starting from the CR interaction, is done through dedicated MonteCarlo and numerical simulations. These simulations take into account all the possible decays or interactions of the charged mesons produced and result into a flux, for the “atmospheric components” that follow a power law, related to the primary CRs spectrum by the following relation:

$$\Phi_\mu(E) \propto E^{-\alpha-1} \quad (1.45)$$

The atmospheric neutrinos were also the perfect probe to study and perform precise measurements of the phenomenon of neutrino oscillation. From an expect ratio at Earth of $\nu_e : \nu_\mu : \nu_\tau = 1 : 2 : 0$, the ratio $\nu_e : \nu_\mu : \nu_\tau = 1 : 1 : 1$ was observed.

1.3 Astrophysical neutrinos

The study and detection of cosmic neutrinos is intimately connected with the γ -ray astronomy and with the detection of CRs. In this section I will treat the main mechanisms for astrophysical neutrino production, even if the reference picture for the production is the same exposed for atmospheric processes, where now accelerated protons interact with the source matter itself. Therefore neutrino astronomy could be a privileged view for the discovery of sources of CRs, that till now are only matter of theoretical speculations.

1.3.1 Neutrino production mechanisms

Assuming that most of the observable astrophysical neutrinos are produced from CR collisions, we have seen how neutrinos can be produced through the pion decay:

$$p + \mathcal{N} \rightarrow X + \text{many} \times (\pi^+ + \pi^- + \pi^0) \quad (1.46)$$

It is important to evaluate the energy distribution of the produced pions. In fact, experimental observations show that the most energetic pion carries out 1/5 of the initial kinetic energy of the incident proton [27]. The pion decay produces high energy neutrinos and γ -rays through the reactions:

$$\pi^0 \rightarrow \gamma + \gamma, \quad \pi^\pm \rightarrow \mu^\pm + \bar{\nu}_\mu \quad \text{followed by} \quad \mu^\pm \rightarrow e^\pm + \nu_e + \bar{\nu}_\mu \quad (1.47)$$

The kinematics of the reaction for the neutral pion decay is such that each gamma brings 1/2 of the initial pion energy, while the produced particles in the charged pion decay chain bring 1/4 of the initial energy. At the end therefore a very simple derivation of the neutrino energy in function of the primary CR energy can be obtained:

$$E_\nu \sim \frac{E_\gamma}{2} \sim \frac{E_\pi}{4} \sim \frac{E_p}{20} \quad (1.48)$$

This relation remains unchanged even in the reactions:

$$p + \gamma \rightarrow \Delta^+ \rightarrow n + \pi^+ \quad \text{or} \quad \Delta^+ \rightarrow p + \pi^0 \quad (1.49)$$

For example a neutrino with energy $E_\nu = 100 \text{ TeV} - 10 \text{ PeV}$ corresponds to $E_p \sim 2 \text{ PeV} - 200 \text{ PeV}$, which is the region just around the knee of the CR spectrum. The two major mechanisms of high energy neutrino production described in eq.(1.46) and eq.(1.49) are referred to as pp -mechanism and $p\gamma$ -mechanism [28]. There are some differences between the two mechanisms:

- the $p\gamma$ is a process with a precise production threshold for the Δ resonance. Having for example a target gamma with an energy $\epsilon_\gamma \sim 0.1 \text{ keV}$, a proton must have energy:

$$E_p > \frac{m_\Delta^2}{4\epsilon_\gamma} = \left(\frac{100 \text{ eV}}{\epsilon_\gamma} \right) \times 4 \text{ PeV} \quad (1.50)$$

which, according to eq.(1.48), results into a neutrino energy of $\sim 200 \text{ TeV}$;

- The pp -mechanism is characterised by the hypothesis of limiting fragmentation [29], known as scaling. This hypothesis assures that secondary particle spectra correspond strictly to the primary distribution, which in this case is the power law of the CR spectrum.

The $p\gamma$ and pp -mechanisms are usually denoted as *hadronic mechanisms*. The γ -ray astronomy in the last years has played a crucial role in the multi-messenger observations, and has put severe constraints on the possible acceleration sites. This has been possible thanks also to the larger interaction cross section of photons that makes their detection easier with respect to neutrinos. γ -rays can be produced through the decay of the neutral pions, produced in the interaction of CRs, according to the hadronic model, but there is also a second mechanism that can produce gamma rays in astrophysical environments, called *leptonic mechanism*. This mechanism instead involves only electrons that are able to produce photons in the X-ray and γ -ray band through inverse Compton and through bremsstrahlung. Only the detection of neutrinos is therefore an inescapable proof of the possibility for a particular source to be the site where CRs are accelerated.

1.3.2 Neutrino and gamma astronomy

As explained in the previous section, the production of neutral secondary particles as neutrinos and gammas is strictly connected to the primary spectrum of CRs. At the same time the recent studies and results obtained by γ astronomy can put some constraints on the neutrino flux expected at Earth coming from identified sources. Specifically, if a Fermi acceleration mechanism produces a power law distributed spectrum, with $\alpha = 2$, thanks to measurements in γ -ray astronomy the normalization factor K (see eq.1.25) for the neutrino flux can be estimated:

$$E_{\gamma,\nu}^2 \frac{d\Phi_{\gamma,\nu}}{dE_{\gamma,\nu}} = 10^{-11} \text{ TeV cm}^{-2} \text{ s}^{-1} \quad (1.51)$$

However the differences between neutrinos and photons must be taken into account. Some of the emitted photons could be produced by leptonic processes, where no neutrinos are present in the final states. Furthermore γ -rays can be absorbed in the source, if thick, and during the propagation the following reaction can occur:

$$\gamma + \gamma_{\text{bkg}} \rightarrow e^+ + e^- \quad (1.52)$$

This process attenuates the photon flux starting from energies of hundreds of TeV, considering the infrared background light emitted from stars. At high energies therefore the connection between neutrinos and gamma-rays is not straightforward, and detailed numerical simulations are needed.

1.3.3 Neutrino flux

In Fig.1.7 different contributions, exposed in previous sections, are summed up. The *conventional atmospheric neutrino flux* considers only ν_μ and $\bar{\nu}_\mu$ contributions to the overall atmospheric neutrino flux. It includes also the *prompt* component, derived from the decay of charmed mesons. For energies below ~ 100 TeV, the experimental points

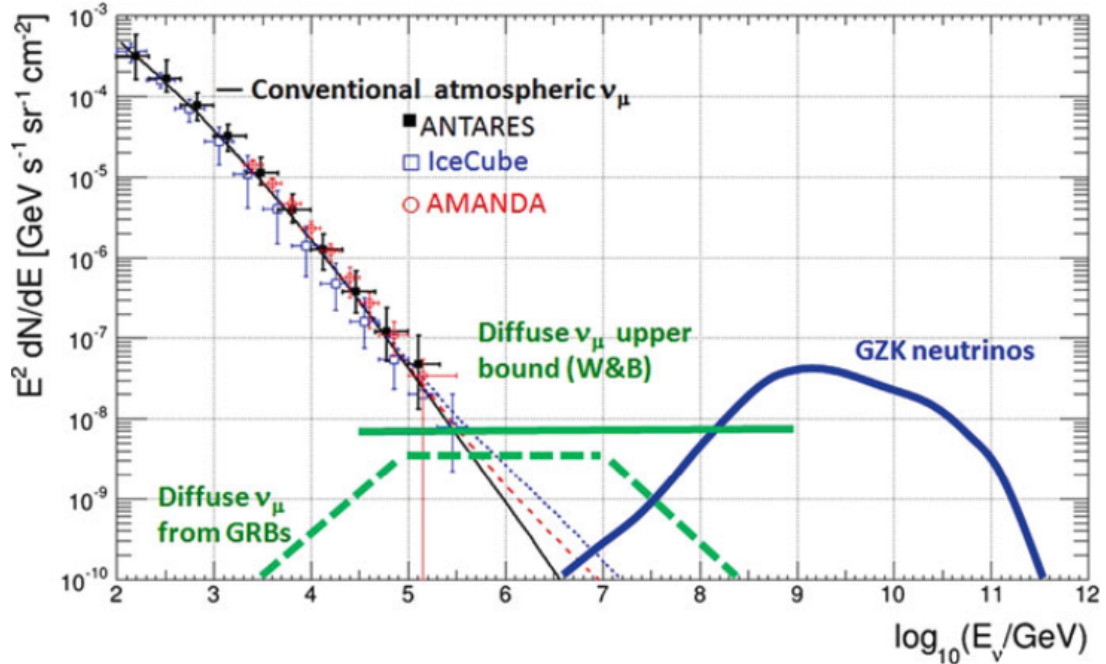


Figure 1.7: Expected neutrino flux estimated from different cosmic models and atmospheric neutrino background. The points are the measures of ν_μ and $\bar{\nu}_\mu$ flux. The black line is the expected atmospheric flux, in which the most energetic part includes also *prompt* neutrinos from the charmed mesons decay. The horizontal green line is the upper bound for the diffuse flux of astrophysical neutrino from Waxman and Bahcall model. The dashed green line is an upper bound for neutrinos originated in GRBs. The blue line instead represents the possible contribution of cosmogenic neutrinos, the ones originated by the GZK effect.

are distributed according to a power law, as in eq.(1.45), with spectral index $\alpha \sim 3.7$. In the PeV region the upper bound for an extra-Galactic diffuse neutrino flux is indicated, derived from [30]. The flux is estimated taking into account only the contribution of AGNs and GRBs. According to this assumption the maximum ν_μ flux can be written:

$$[E^2 \Phi_{\nu_\mu}(E)]_{\max} \approx 0.9 \times 10^{-8} \frac{\text{GeV}}{\text{cm}^2 \text{s sr}} \quad (1.53)$$

The all flavour upper bound ($\nu_e + \nu_\mu + \nu_\tau$) is three times larger than eq.(1.53). In the same energy region, with the green dashed line, the expected neutrino flux from the single GRB component is reported. According to the *fireball model*, shock waves emerge in the relativistic outflow of material, in which electrons are accelerated producing the electromagnetic radiation. In the same region also protons can be accelerated, producing, with the same mechanism, high energy neutrinos that accompany the electromagnetic burst. Also in this case it is possible to estimate the maximum neutrino flux [30]:

$$[E^2 \Phi_{\nu_\mu}(E)]_{\max}^{\text{GRB}} \approx 3 \times 10^{-9} \frac{\text{GeV}}{\text{cm}^2 \text{s sr}} \quad (1.54)$$

Astrophysical neutrinos can therefore be selected, over the background, outlining an excess of events from a given direction (point-like searches) or as an excess of high-energy events (diffuse search), considering that starting from ~ 100 TeV the diffuse astrophysical neutrino flux exceed the atmospheric one.

1.3.4 State of the art of astrophysical neutrino detection

Till now the IceCube detector was the only experiment capable to observe astrophysical neutrinos in two independent samples. The first one was an excess of high-energy events over the atmospheric background, detected between May 2010 and May 2013 [31]. The measurement had a statistical significance larger than 6 standard deviations with respect to the only-background hypothesis. The neutrino events were selected with the requirement that the interaction vertex was contained inside the instrumented volume of the detector. This first set of events was defined *High Energy Starting Events* (HESE). In Fig.1.8 the energy distribution and their $\sin(\text{declination})$ is shown. The poor angular resolution does not allow to accurately locate in the sky the source of these neutrino signals. The second data sample was still an excess of diffuse flux of astrophysical neutrinos. The selection procedure was carried out selecting CC upgoing muon neutrino events [32]. In this sample $\sim 500,000$ muon neutrino candidates were selected with a

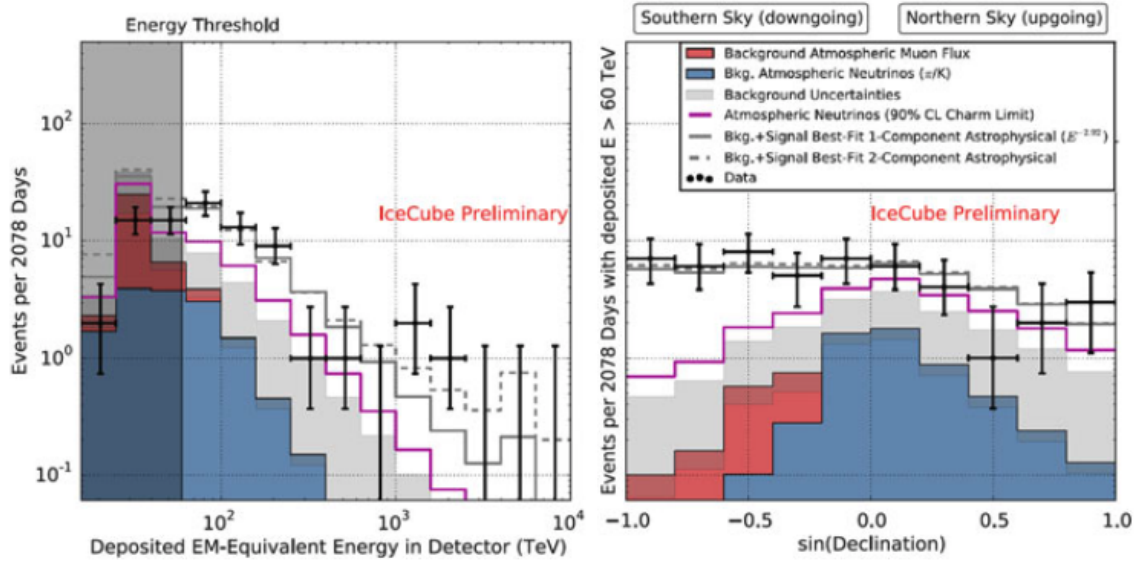


Figure 1.8: **left:** deposited energy, **right:** arrival direction in IceCube detector of the observed HESE events, compared with predictions (red atmospheric muons and blue the atmospheric neutrinos). The sample refer to 6 years of data. Figure taken from [31].

negligible contamination from atmospheric events. Also for this sample, the significance of the observation respect to the pure background hypothesis was at 6.7σ . The real breakthrough event for neutrino astronomy occurred in September 2017, when IceCube detected a muon-like event induced by a ~ 300 TeV neutrino, causing an alert for the searches of γ -ray counterparts. The Fermi-LAT satellite and the MAGIC gamma ray telescope reported a coincidence with neutrino direction of a known γ -ray source, the active galaxy TXS 0506+056 (object classified as a blazar). Neutrino correlation with the registered activity of TXS 0506+056 was classified as statistically significant at the level of 3σ [33].

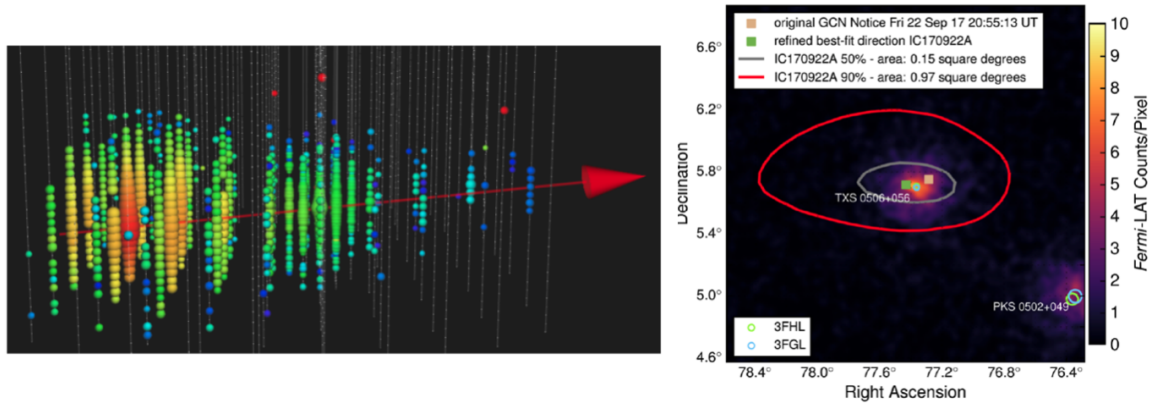


Figure 1.9: **left:** event display of the high-energy neutrino detected by IceCube collaboration; **right:** spatial coincidence with the neutrino direction found from FERMI-LAT and MAGIC. Figures taken from [33].

1.3.5 Gravitational wave in the multi-messenger scenario

With the first detection of Gravitational Wave (GW) by the Ligo collaboration in September 2015 [34], a new window on the Universe was opened. Since that moment, lots of other GWs have been detected, but probably the most important one was detected in August 2017 by the VIRGO/Ligo collaboration [35]. The first coincidence signal of a GW and its electromagnetic counterpart was announced on 2017 October 16. The astrophysical event, at the origin of the GW, was the coalescence of two neutron stars ~ 40 Mpc away from the Earth. From the study of the electromagnetic *follow-up* in the following days the signatures of synthesised materials, like gold and platinum, was revealed, resolving a long lasting mystery on the nature of the heaviest elements of the periodic table. Also the neutrino signal counterpart was searched by IceCube, ANTARES and Pierre Auger Observatory collaborations but no statistically significant excess was found [36]. After this event, several joint analyses have been conducted by the ANTARES collaboration, together with IceCube and other cosmic ray and γ -ray experiments, considering five events (GW150914, GW151226, LVT 151012, GW170104,

and GW170817), producing no statistical evidence of neutrino involvement [37]. The multi-messenger observations conducted till now, considering both the neutrino- γ and the GW- γ coincidences have replied to important unanswered questions in astrophysics and in particle physics. The possibility in the future, with the advent of the second generation neutrino telescopes, of the detection of a coincidence between GWs and neutrinos would shine a unique light on source properties. Main candidates for a possible coincidence are GRBs from core-collapse supernova and binary coalescence of at least one non black-hole object [38]. Furthermore the possible coincident detection can put severe constraints on neutrino mass ordering, and, in the most optimistic scenario, even on the absolute mass of the neutrino itself, thanks to the measurement of the difference between the arrival time of GW and of the incoherent neutrino wave packet. Just to mention, lots of efforts are spent, not only on the experimental site trying to detect these coincidence signals, but also under the theoretical point of view. Several papers, for example, studied the modification of neutrino oscillation when interacts with static gravitational fields. A recent study tries to infer what could be the impact, on astrophysical neutrino mixing, of the interaction with a time dependent gravitational field, as that produced by a GW [39].

Chapter 2

Neutrino telescopes and KM3NeT

The idea of a telescope based on the detection of secondary particles produced in neutrino interactions was suggested by Markov and Zheleznykh in 1960 [40]. The necessity of big instrumented volume detectors, due to the small neutrino cross section ($\sigma \sim 10^{-38} E_\nu/GeV$), was solved exploiting large and transparent medium given by nature. This type of detectors registers the Cherenkov light, induced along the path of charged secondary particles, with a large array of photosensitive devices. Using the arrival time of the Cherenkov photons and the position of the photosensors, the direction and energy of the incoming neutrino, as well as other parameters of the neutrino interaction, can be reconstructed.

In the mid-70s the DUMAND collaboration started a pioneering project to deploy a neutrino telescope offshore Hawaii Island [41]. Unfortunately, the technology was not yet mature and the tentative was abandoned. This marked the starting point of a series of other projects: AMANDA at the South Pole [42], which was the precursor of the present large detector IceCube [43]; Baikal, under the water of the lake Baikale, at present expanding towards a km^3 structure, named GVD [44]. In the Mediterranean Sea, the ANTARES experiment [45], located offshore the French southern coasts, is the precursor of the future KM3NeT/ARCA and ORCA detectors that will reach a km^3 instrumented

volume. While the last two are in the Northern hemisphere, looking at the centre of our Galaxy, IceCube telescope is in the Southern hemisphere. They share the same detection principle, and the main difference consists in the photocathode area density, optimised for the targeted physics goal, which determines neutrino energy threshold. The overall structure of this section and partly also the content is inspired by PhD theses [46–48].

2.1 Detection principle

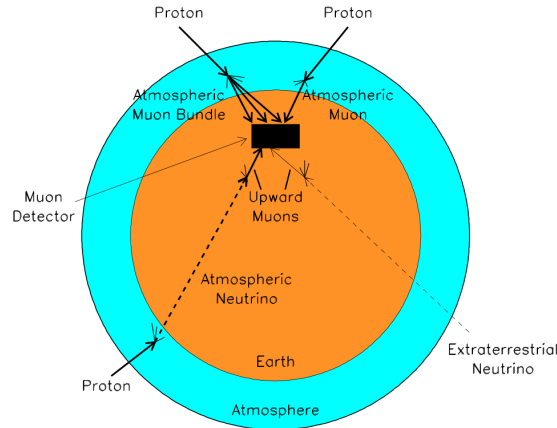


Figure 2.1: Illustration of the possible origin of events and background inside the telescope.

The detection principle in an underwater neutrino telescope is the collection of optical photons, induced along the path of the secondary particles generated in the interaction of neutrinos with the rock under the telescope or with water surrounding it. Depending on the flavour of neutrinos and on the interaction channel, charged (CC) or neutral (NC), different final states are possible. However high-energy muons produced in ν_μ charged current interactions represent the *golden channel* for the identification of neutrino sources, since they are highly penetrating particles (range in water for 1 TeV muon is several kilometres) and their direction can be reconstructed with high accuracy. Electron neutrinos can be identified through the detection of the particle showers initiated by the charged lepton. Theoretical expectations on neutrino fluxes, see Fig.1.7, and neutrino cross sections suggest that a detection area of the order of 1 km² is necessary in order to have a rate of some events/year. These detectors must be shielded from the intense flux of atmospheric muons, originated in the upper parts of the atmosphere over

the detector. At Earth level, the atmospheric muon flux is about 10^{11} times larger than the one of atmospheric neutrinos. For this reason the detector must be placed under thousands of metres of water or ice. Even at such depths, the atmospheric muon flux is six orders of magnitude larger than that of muons induced by atmospheric neutrinos, and is able to generate in the telescope a top-bottom signal: these are called *downgoing events*. In order to reject part of this overwhelming background, a geometrical selection of the events upward going is applied onto the tracks, after their reconstruction, because only neutrinos can cross the Earth producing charged particles coming from below. In this case the telescope registers a bottom-top signal, producing what are called *upgoing events*. Muons are absorbed within a path of about 50 km of water, and they are not able to traverse the entire Earth diameter ($\sim 13\,000\text{km}$).

Even *upgoing* events suffer background due to misreconstructed downgoing events.

2.1.1 Cherenkov radiation

The Cherenkov radiation is generated by the passage of charged particles through a dielectric medium with refractive index n , with a velocity greater than the speed of light in that medium (c/n). The charged particles polarise the molecules along the trajectory, and only when the electrons come back to their ground state, they emit a coherent radiation. The light is emitted at a characteristic angle θ_{ch} , as depicted in Fig.2.2. The opening angle depends on the particle velocity $\beta = v/c$ and on the refractive index n of the medium:

$$\cos(\theta_{ch}) = \frac{c/n}{\beta c} = \frac{1}{\beta n} \quad (2.1)$$

In water $n \approx 1.35$ and the Cherenkov angle for relativistic particles ($\beta \approx 1$) is $\theta_{ch} \approx 42^\circ$. The number of emitted photons per path length dl and wavelength interval $d\lambda$ is given by the Frank-Tamm formula:

$$\frac{d^2 N}{dld\lambda} = \frac{2\pi\alpha z^2}{\lambda^2} \left(1 - \frac{1}{\beta^2 n(\lambda)^2} \right) \quad (2.2)$$

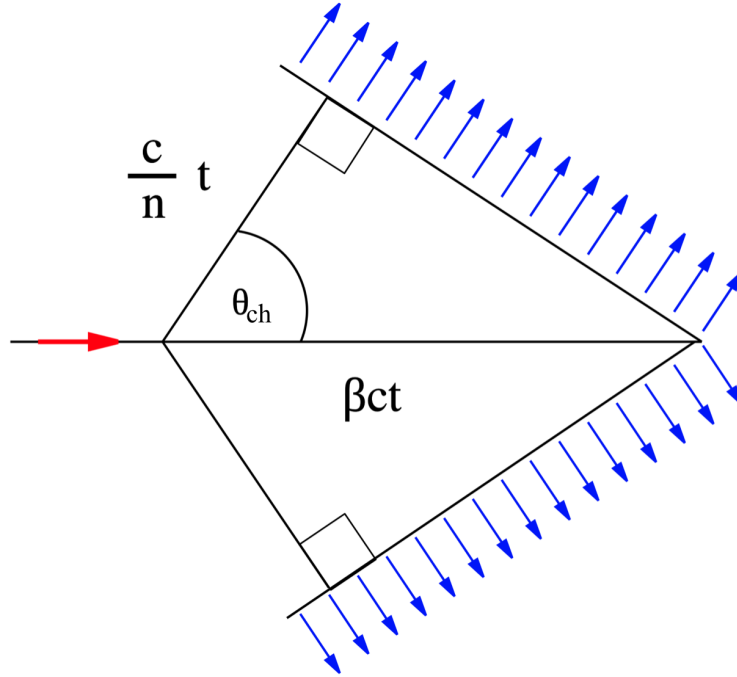


Figure 2.2: The outlined angle is θ_{ch} . The red arrow represents the propagation direction of the charged particle. The blue arrows show the propagating wave front of the produced light.

where α is the fine-structure constant. In the wavelength range from 300 nm to 600 nm, in which the water is transparent, the number of photons per particle path length is approximately:

$$\left. \frac{dN}{dl} \right|_{water} = 340 \text{ cm}^{-1} \quad (2.3)$$

Cherenkov radiation however occurs only for $\beta > 1/n$. Therefore the energy threshold E_{th} , for a particle with rest mass m_0 is:

$$E_{th} = \frac{m_0}{\sqrt{1 - 1/n^2}} \quad (2.4)$$

In water this corresponds to a threshold kinetic energy ($T_{th} = E_{th} - m_0$) $T_{th}^e \approx 0.25$ MeV for electrons, $T_{th}^\mu \approx 53$ MeV for muons and $T_{th}^p \approx 460$ MeV for protons.

2.1.2 Light propagation

Once the light is produced, other physical effects influence the signature of Cherenkov light: absorption and scattering in water. While the first one affects the number of photons, the latter influences the direction and arrival time of photons on the photosensors. In order to describe properly these two effects, two key parameters must be introduced, the absorption length $\lambda_{abs}(\lambda)$ and the scattering length, $\lambda_s(\lambda)$. The absorption parameter corresponds to the total photon path length after which the survival probability is reduced by $1/e$. Optically pure seawater shows the highest transparency for photon wavelength of about ~ 400 nm, where typical values of $\lambda_{abs} \approx 60$ m are reached. When one considers scattering, λ_s and the angular distribution of the momentum of the outgoing particles must be taken into account, because both contribute to the definition of an effective scattering length. The scattering typically occurs on water molecules (‘Rayleigh scattering’) and on larger particulates (‘Mie scattering’), resulting in a small total scattering angle over the detectable wavelength range. The effective scattering length is defined as:

$$\lambda_s^{eff} = \lambda_s / [1 - \langle \cos(\theta_s) \rangle] \quad (2.5)$$

where $\langle \cos(\theta_s) \rangle$ is the average scattering angle. In seawater typical values of $\lambda_s \approx 55$ m and $\lambda_s^{eff} \approx 265$ m have been measured for photon wavelength of 470 nm.

2.2 KM3NeT detector

KM3NeT¹ is a research infrastructure housing the next generation neutrino telescopes. Once completed, it will host a network of Cherenkov detectors, reaching, in its final configuration, an instrumented volume of several cubic kilometres of sea water. It is located at the bottom of the Mediterranean Sea, and its design was driven by the expe-

¹KM3NeT is an acronym for ‘Cubic Kilometre Neutrino Telescope’

rience gathered with the first generation neutrino telescopes, especially ANTARES. This detector in fact has demonstrated the feasibility of the Cherenkov technique in deep sea for neutrino detection. KM3NeT comprises two different instrumented regions, placed in separate locations: KM3NeT/ARCA², off-shore Sicily coasts, whose goal is the search of neutrinos generated from astrophysical sources, and KM3NeT/ORCA³, off-shore the French Southern coasts that will study neutrino properties exploiting atmospheric neutrinos generated in the Earth's atmosphere. Both detectors will use the same technology and neutrino detection principle, namely a 3D array of photosensors capable to detect Cherenkov light produced along the path of relativistic particles emerging from neutrino interactions. The main difference is the density of photosensors, which is optimised for the study of neutrinos in the few-GeV (ORCA) and TeV-PeV energy range (ARCA), respectively. The facility will also house instrumentation for Earth and Sea sciences for long-term and on-line monitoring of the deep sea environment and the sea bottom at depth of several kilometres [49]. The following sections were inspired by [46].

2.2.1 Installation sites

The Mediterranean Sea offers optimal conditions to host an underwater neutrino telescope. Several sites were studied and characterised, and the deploy feasibility evaluated through different criteria such as: distance from the coast, sufficient depth in order to reduce the atmospheric muon background, good optical properties of the water, low level of bio-luminescence, low rates of sedimentation and stable low sea current velocities. The three locations selected are shown in Fig.2.3.

KM3NeT/ORCA Deployed at the KM3NeT-Fr installation site, about 40 km off-shore Toulon, France, the ORCA neutrino detector will achieve the angular and energy

²ARCA stands for Astroparticle Research with Cosmics in the Abyss

³ORCA stands for Oscillation Research with Cosmics in the Abyss

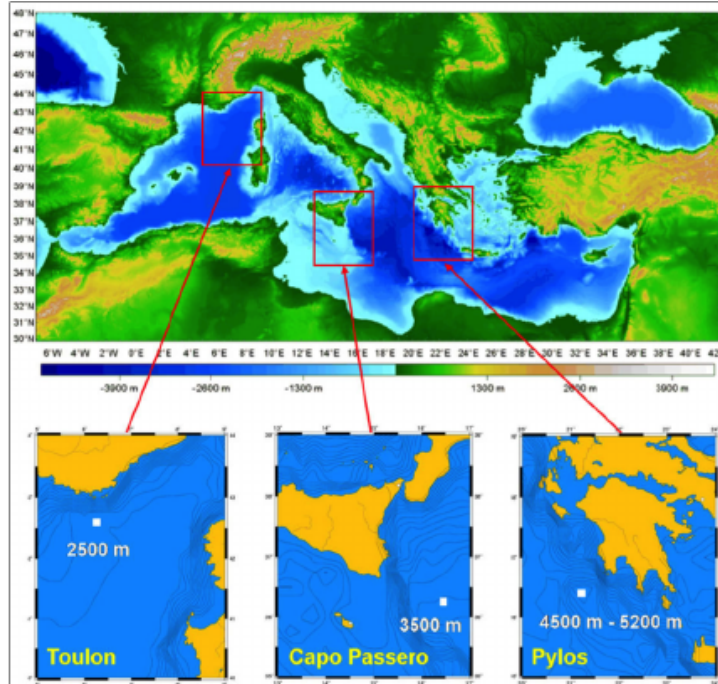


Figure 2.3: Map of the location of the 3 sites for the construction of the KM3NeT neutrino telescope in the Mediterranean Sea. KM3NeT-Gr is located off the coast of Pylos. At present, it is used only for validation and qualification. Taken from [50].

resolution required for resolving the neutrino mass hierarchy. The sensor modules are arranged on vertical detection units with a height of about 200 m and in the dense configuration required for detection of neutrinos with energies as low as about a GeV. During February 2020 sea campaign, 7-strings configuration with a horizontal spacing of about 20 m has been achieved. In the next construction phase (KM3NeT 2.0), full ORCA will comprise a building block of 115 detection units.

KM3NeT/ARCA instead is being installed at the KM3NeT-It site, about 100 kilometres off-shore the town of Portopalo di Capo Passero in Sicily, Italy. The detection units of the ARCA telescope will be anchored at a depth of about 3500 m. In its final configuration the ARCA telescope will consist of two building blocks of 115 vertical

detection units each, resulting in an instrumented volume of about 1 cubic kilometre – slightly larger than IceCube neutrino telescope. The construction of ARCA, at the end of Phase-1, will contain 24 detection units, reaching a volume of about 0.1 cubic kilometre.

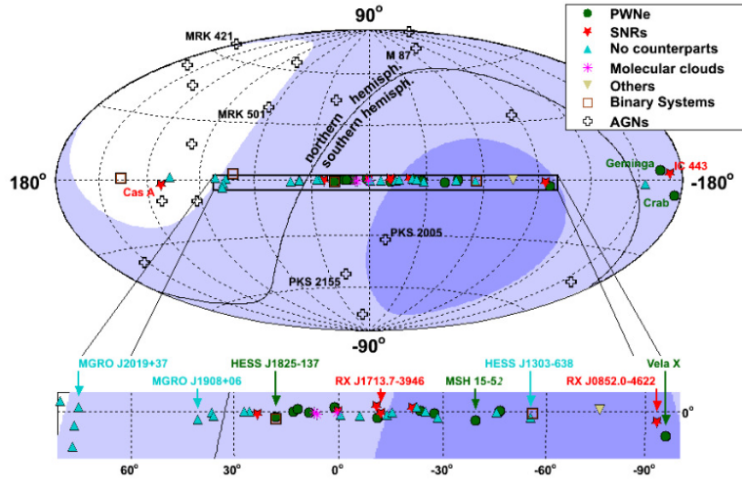


Figure 2.4: Sky coverage of KM3NeT detectors. Some known astrophysical objects are marked. Figure taken from [51].

Both sites are in the Northern hemisphere at a latitude between 36° and 43° North, allowing to observe upgoing events coming from most of the sky. Looking at the KM3NeT sky coverage, reported in Fig.2.4, most of the Galactic plane, including the Galactic centre, is visible. This is an advantage considering the sources hosted in the centre of our Galaxy, and KM3NeT is able to complement the field of view of IceCube telescope, located at the South Pole.

2.2.2 Digital Optical Module (DOM)

The ‘Digital Optical Module’ (DOM) developed by the KM3NeT collaboration is the active part of the neutrino telescope and consists of a transparent 17-inch diameter pressure-resistant glass sphere, housing 31 3-inch PMTs, their associated readout elec-



Figure 2.5: Photograph of the Digital Optical Module (DOM) of KM3NeT complete (left) and in assembly phase (right). Taken from [46].

tronics and additional sensors, as shown in Fig.2.5. The task of the DOM is to register the time of arrival of the Cherenkov light generated in the sea water inside or close to the detector; the modules also measure their geometrical position at the arrival time of the light. The PMTs have a standard bialkali photo-cathode with quantum efficiency of 28% at 404 nm and 20% at 470 nm. Moreover this multi-PMT configuration offers some advantages compared to more traditional designs based on large-area PMTs, such as: (i) maximisation of the photocathode area in a single sphere; (ii) small PMTs are less sensitive to Earth magnetic field, not requiring metal shielding; (iii) segmentation of the detection area, improving the discrimination between single-photon and multi-photon hits.

The PMTs are arranged in 5 rings of tubes at zenith angles of 50° , 65° , 115° , 130° and 147° , respectively. In each ring there are 6 PMTs and a single PMT is placed at the bottom, with a zenith angle of 180° : therefore 19 PMTs are placed in the lower hemisphere and 12 PMTs in the upper hemisphere of the DOM. Each PMT is surrounded by a reflector ring in order to increase the photon collection efficiency (20-40% depending on photon incident angle), and optical gel fills the cavity between PMT and glass sphere in order to assure optical contact. An active base is also attached to the PMT allowing to

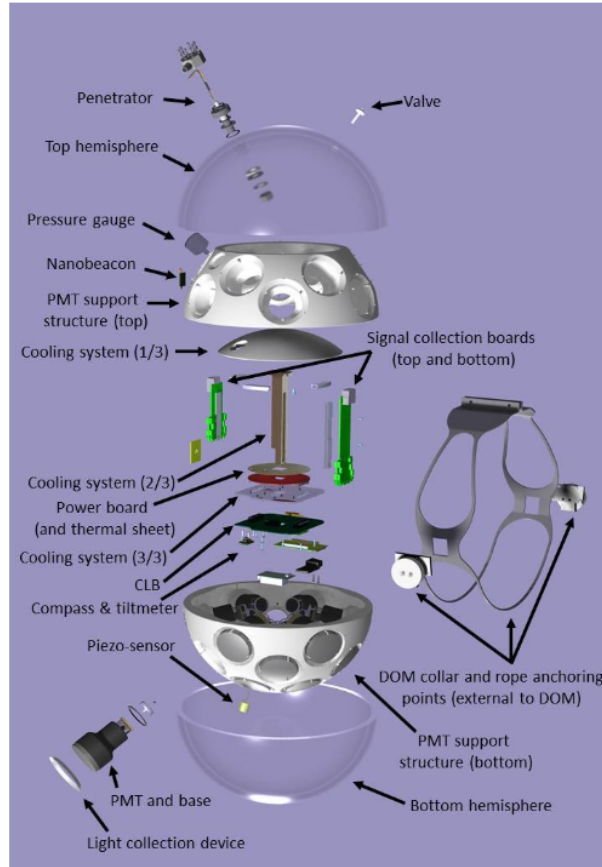


Figure 2.6: Exploded view of the KM3NeT DOM. Taken from [52].

control from shore the high-voltage power supply (~ 1000 V), and threshold settings for each tube. This board has been miniaturized in order to fit in the limited space available inside the glass sphere. When a photon hits the photomultiplier tube, a small electrical pulse is created. The pulse is then amplified and transformed into a square wave pulse, by the time-over-threshold (ToT) technique (the amount of light is transformed to an amount of charge which is translated to the length of the square wave pulse), and sent to the Field Programmable Gate Array (FPGA), hosted on the Central Logic Board (CLB), where its arrival time and its pulse length is registered and stored for a later transfer to shore. The internal structure of the DOM has been carefully designed to efficiently dissipate the heat generated from the electronics using a mushroom shaped

aluminium structure that transfers it to the sea via the glass sphere, see Fig.2.6. The DOM also contains other sensors used for calibration purposes: a compass to know the pointing direction of each photomultipliers; accelerometres to know tilt, pitch and yaw of the module; a piezo-acoustic sensor allows the determination of the position of the DOM exploiting a sonar technique. All these measurements are important as the DOMs move under the influence of sea currents. In ANTARES, this calibration devices can locate the photosensors with an uncertainty of less than 10 cm.

2.2.3 Detection Unit (DU) and detector layout

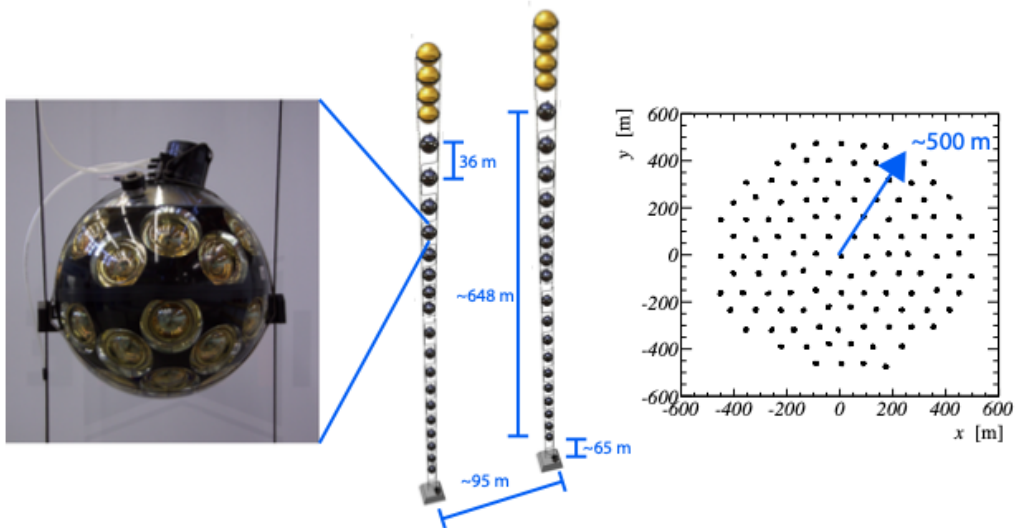


Figure 2.7: Schematic outline of a KM3NeT/ARCA building block. Taken from [53]

A collection of 18 DOMs connected to an electro-optical cable and arranged along a vertical structure with two ropes is called Detection Unit or DU (or string) for short. A detection unit has an anchor, which keeps it firmly connected to the seabed. Even though the DU design minimises drag and by itself is buoyant, additional buoyancy is introduced at the top of the string to reduce the horizontal displacement of the top in

case of large sea currents. A vertical electro-optical cable that contains two copper wires for the power transmission (400 VDC) and 18 optical fibres for the data transmission is attached to the ropes. The power conductors and optical fibres enter the glass sphere via a penetrator. The detection units are connected to junction boxes, fixed to the sea bed and equipped with several connectors, each of which can power several detection units in series. The underwater connection of the units to the junction boxes is via interlink cables running along the seabed. A main electro-optical cable connects the underwater detector to the shore station providing power and allowing the transmission of information from sea to shore (data) and viceversa (control). The KM3NeT fibre-optic network makes use of Dense Wavelength Division Multiplexing. This method allows for signals of many different carrier frequencies to pass through a single fibre. These fibres run a maximum of 100 kilometres to shore, where the frequencies are separated again. In this way each DOM has its own unique path. All the data acquisition system of the KM3NeT experiment will be explained in details in the next chapter [49]. KM3NeT is a three dimensional array of DOMs and the array configuration is defined by the number of strings, their horizontal spacing and vertical spacing between DOMs along the string. These parameters have been optimised using MC simulations [54], in order to obtain the maximum detection efficiency. For a given total number of optical modules, the detection efficiency gradually improves following the number of strings. At about 120 strings per building block and 18 optical modules per string, the detection efficiency remains constant. The ARCA and ORCA DUs have 18 DOMs on each string and 115 strings in each building block, optimised for the different physical goals: ARCA has an inter-DOM distance of 36 m along the string and the distance between units is about 100 m as shown in Fig.2.7, while in ORCA DUs the distance between DOMs is around 9 m and the horizontal spacing is 20 m.

2.3 Event signatures

The event signatures in a water/ice Cherenkov detector are split into two main categories: track-like events, originating from ν_μ charged current (CC) interaction and producing a muon that can propagate in water for several kilometres; shower-like events, originating from $\nu_e(CC)$, $\nu_\tau(CC)$ and ν_l neutral current (NC) that give rise to particles that propagate only for tens of metres. A schematic representation of different types of signatures in the detector is depicted in Fig.2.8.

Muon track The kinematics of the charge current interaction originating a muon is such that there is a small angle between neutrino and muon direction (see Fig.2.9). Therefore track-like events can be reconstructed with an accuracy better than one degree. Since the kinematic angle decreases with energy, the angular resolution is dominated by track reconstruction at energy above few TeVs. At energies of the order of 10 TeV or more, the angular resolution is about 0.3° , therefore neutrino and muon can be considered almost collinear. When a high energy muon propagates in a medium (like water or ice), the major energy losses are ionisation of the medium, radiative processes and, for a negligible fraction, Cherenkov radiation. The total energy loss for muons with energies above 1 TeV can be expressed as:

$$\frac{dE}{dx} = -\alpha(E) - \beta(E)E \quad (2.6)$$

where α refers to ionisation and β to the radiative loss. According to eq.(2.6), the range is computed as:

$$R = \frac{1}{\beta} \ln \left(1 + \frac{E_\mu \beta}{\alpha} \right) \quad (2.7)$$

After slowing down, the muon eventually decays at rest (muon lifetime $\sim 2.2 \mu\text{s}$) into two neutrinos and an electron that causes an EM shower. At energies greater than few TeVs the radiative processes, like bremsstrahlung and pair production, start to be dominant

Interaction		Particle signature	Detector signature
$\bar{\nu}_\mu$ CC		hadronic shower and μ track	track-like
		hadronic shower and μ track ($\tau^\pm \rightarrow \mu^\pm \bar{\nu}_\mu \bar{\nu}_\tau$, $\sim 17\%$ BR)	
$\bar{\nu}_\tau$ CC		hadronic and EM shower ($\tau^\pm \rightarrow e^\pm \bar{\nu}_e \bar{\nu}_\tau$, $\sim 18\%$ BR)	point-like or shower-like
		hadronic showers ($\tau^\pm \rightarrow \text{hadrons}$, $\sim 65\%$ BR)	
$\bar{\nu}_e$ CC		hadronic and EM shower	
$\bar{\nu}$ NC		hadronic shower	

Figure 2.8: Possible signatures of neutrino-induced events in water/ice Cherenkov detectors. Black dashed lines represent neutrinos, orange ones the muon, red ones the e^-/e^+ generated in electromagnetic (EM) showers, blue ones represent particles in hadronic showers and green ones are the τ leptons. The third diagram from the top is what is called ‘double bang’. Taken from [55]

and so-called ‘catastrophic’ energy losses are visible as electromagnetic showers along the muon track. This peculiarity of muon propagation contributes significantly to the signature observed in neutrino telescopes targeting TeV–PeV neutrinos.

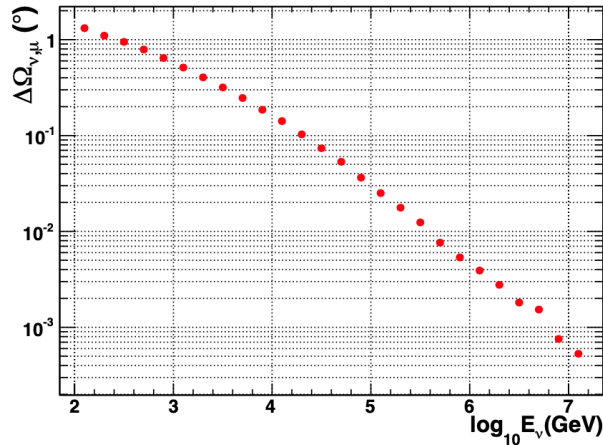


Figure 2.9: Median of the angle between the neutrino and the produced muon directions in function of the neutrino energy, taken from [46]

Electromagnetic and hadronic showers The event signature due to NC, and ν_e and ν_τ CC interactions inside or close to the instrumented volume is a particle shower (often referred to as a shower-like or cascade event). The particle shower constitutes a Cherenkov light source which appears point-like compared to the typical distances between photosensors in neutrino telescopes. This characteristic offers the opportunity to estimate the energy released in a neutrino-induced shower more reliably with respect to track-like events, while the direction determination is more difficult and generally results in a poor angular resolution [56]. The evolution of an electromagnetic shower is characterised by the radiation length X_0 , which represents the average distance after which the energy is reduced by a factor e (in water $X_0 \sim 36$ cm). The average longitudinal profile of the energy deposition, as well as the Cherenkov light production can well be parameterised as:

$$\frac{dE}{dt} = E_{in} b \frac{(bt)^{a-1} e^{-bt}}{\Gamma(a)} \quad (2.8)$$

where $t = x/X_0$ is the number of radiation lengths. a and b have been determined specifically for water from several simulations, and can be written as: $a = 1.85 +$

$0.62 \cdot \ln(E/\text{GeV})$ and $b = 1.85$. The maximum in the longitudinal profile is found at $t_{max} = (a - 1)/b$ and is equivalent to the brightest point in Cherenkov light emission, located ~ 1 m far from the starting point of the shower, for energies around some GeVs. The lateral extension of the energy deposit and Cherenkov light production is restricted to distances below the Molière radius that in water is smaller than 10 cm. The total Cherenkov light yield is proportional to the initial energy with fluctuations smaller than 1%: this allows a very precise calorimetric measurement. The longitudinal development of hadronic showers is very similar to that of an electromagnetic one, apart from the fact that it is driven by hadronic interactions instead of electromagnetic ones. In water the nuclear interaction length is ~ 83 cm. The light is emitted by charged particles with energies above their Cherenkov thresholds and both hadronic and EM showers appear as a point-like burst of light in the detector. However, given the same initial energy, hadronic showers produce less Cherenkov light. The main reason is that hadrons, compared to electrons, have higher energy thresholds for Cherenkov radiation due to their larger masses. With increasing energy, however, the average light yield of hadronic showers approaches that of electromagnetic showers. Moreover hadronic showers show large event-to-event fluctuations in the Cherenkov light yield because of (i) the variation in the hadronic final states and (ii) the interaction of shower particles with the medium during their propagation. In addition, for energies of few GeVs the initial hadronic shower particle directions are not collinear and the space angles between them are $\mathcal{O}(10^\circ)$. Thus, the light emission signature is characterised usually by several Cherenkov cones with different intensity depending on the initial hadron types, their momenta and their interactions in the shower evolution. This leads to a huge variety of different event signatures of hadronic showers with energies of few GeVs. With increasing shower energy, the initial hadrons become more and more collinear, so that the individual Cherenkov cones overlap and the effective angular light distribution approaches that of electromagnetic showers. Therefore telescopes targeting TeV-PeV neutrinos do normally not distinguish between

showers initiated by an electron or a set of hadrons.

An example of the light deposit for the two different signature can be seen in Fig.2.10

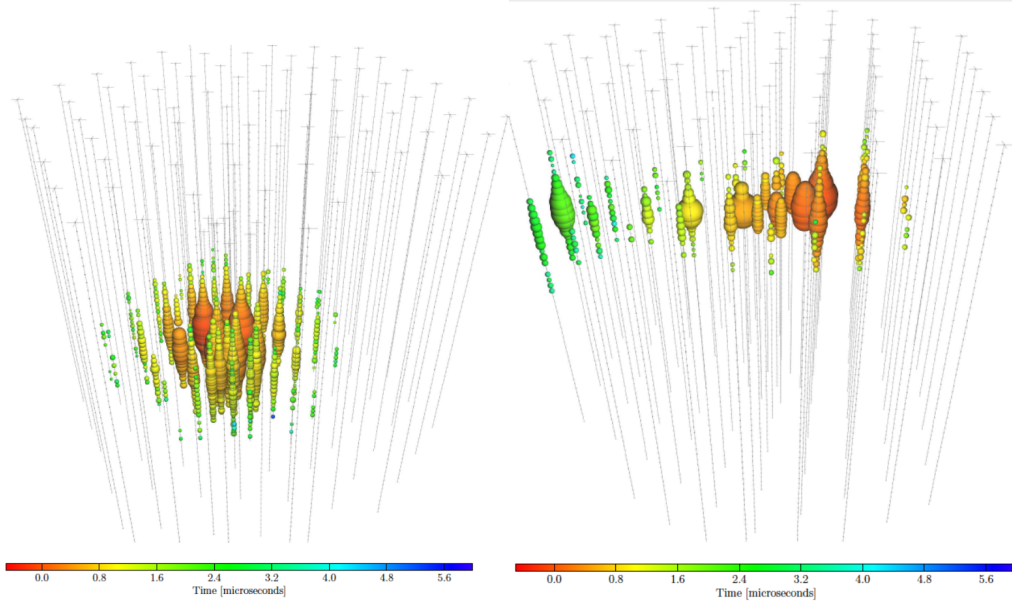
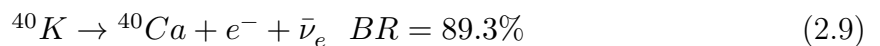


Figure 2.10: Event display of a shower event (left) and track-like event (right). The colours refers to the time evolution of the light deposit. Taken from [57].

2.3.1 Environmental background

The rate of photo-detection is dominated by light produced in the environment where the detector is immersed. There are, in fact, two main sources of background: Cherenkov light produced by electrons, originated in β -decay of radioactive salts dissolved in seawater and bio-luminescence induced by biological organisms.

Radioactivity Seawater contains a small amount ($\sim 0.04\%$) of radioactive isotopes as Potassium-40 (^{40}K), that has two main decay channels:



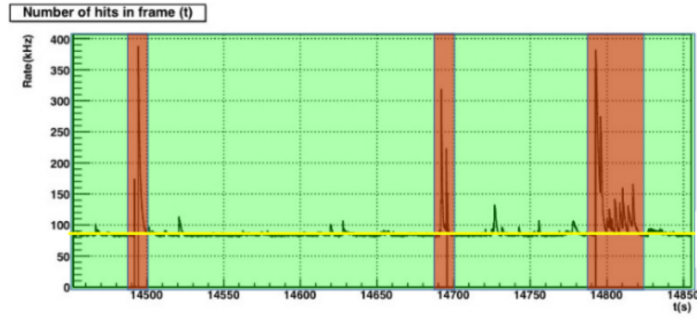
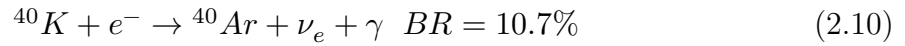


Figure 2.11: Background mean rate measured from a DOM. The yellow line represent the contribution from radioactive, dark current and bacteria bio-luminescence called *baseline*. The red intervals represents the *burst* of few seconds generated by large organisms.



The electrons produced in the first process can achieve a maximal energy of 1.33 MeV and can produce Cherenkov light. Also γ , produced in the second reaction, has an energy of 1.46 MeV which can generate, through Compton scattering, an electron over Cherenkov threshold. Radioactive decays may produce photons in a time window of 1 ns, giving raise to coincidences on neighbouring PMTs.

Dark current (DC) rate This type of background is the rate measured by photosensors without external light sources. It is usually generated by thermal noise inside the PMT or by radioactive decays in the glass sphere or in the optical gel.

Radioactivity and DC gives generally a steady contribution to the background, also known as baseline (see Fig.2.11)

Bio-luminescence It is the light emitted by a large variety of luminescent organisms. The variability in time for this type of background has been studied outlining two main different contributions: (i) variations in time scales of seasons, presumably originated from bacteria, producing a quite constant contribution and (ii) “burst” with duration of

the order of seconds, presumably from larger size organisms.

2.3.2 Physical background

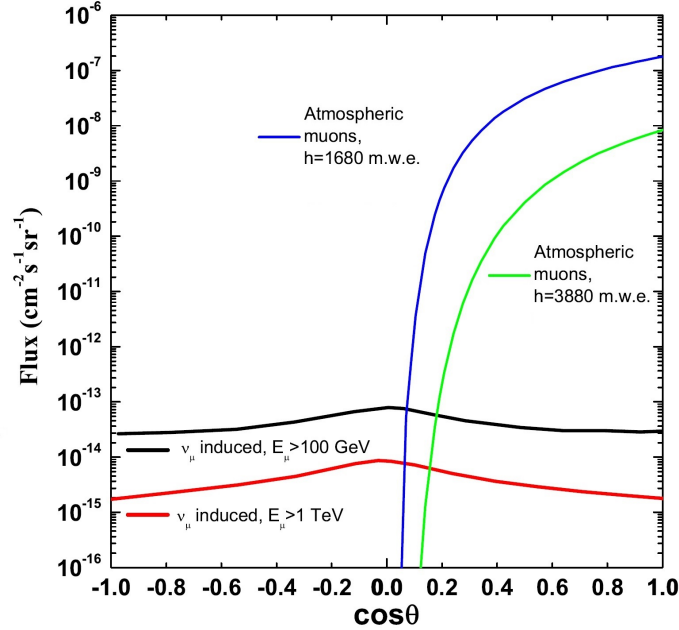


Figure 2.12: Atmospheric muon flux, evaluated following the parameterization in [58], at two different depths (1680 and 3880 metres water equivalent) compared to the flux of muons due to atmospheric muon neutrinos considering two different muon energy thresholds. The neutrino flux is calculated according to [59]. Plot taken from [16].

Muons, originated from the interaction of CRs with the nuclei in the atmosphere, as shown in the previous chapter, represent a great source of background. Most of the muons produced are stopped in the layers of material above the detector, but they can reach the detector from above, depending on their energy and on the zenith angle. This is the main reason why neutrino telescopes are placed under several metres of ice or water, in order to maximise the overburden above that acts as a shield against these muons. In Fig.2.12 the flux of atmospheric muons at different depths is shown, and is a factor $\sim 10^6$

times larger than the flux of muons induced by atmospheric neutrinos interacting inside or in proximity of the detector. Nevertheless, misreconstructed atmospheric muons can mimic an upgoing event signature and may simulate a neutrino-induced signal event. For this reason a precise and efficient event selection is needed in order to reduce this type of background. At the same time events induced by atmospheric neutrinos represent a small but irreducible background to the signal from cosmic neutrinos (blue line in Fig.2.12 is distributed almost uniformly in $\cos \theta_{zenith}$ between -1 and +1).

Chapter 3

The Bologna Common Infrastructure test-bench for KM3NeT data acquisition system

The modular design for building KM3NeT detectors allows for a progressive implementation and data taken even with incomplete detector. The same scalable design is used for the Trigger and Data Acquisition System (TriDAS). In order to reduce the complexity of the hardware inside the optical modules, the “all data to shore” concept is adopted: all the records from photon hits are sent to shore by a computer network which includes both the shore-station and the detector. In the final configuration, the expected data throughput from both sites is up to 500 Gbps. This large traffic is mainly due to environmental optical background (^{40}K decay and bio-luminescence), described in the previous chapter, with a mean rate of $\sim 7\text{-}10$ kHz per PMT. Comparing it with the physical signals expected, coming from astrophysical neutrinos (3/day in ARCA), and atmospheric neutrinos (50.000/year reconstructed in ORCA), it represents a signal-to-noise ratio of about 1 in a million. For this reason the performances required are: nanosecond timing accuracy on the photon arrival time, effective and fast on-shore on-

line trigger algorithms searching for correlations between all the photon hits sent from the detector, rejecting the overwhelming background and also the necessity of expansion of the on-shore DAQ infrastructure to handle an increasing data-rate. In addition, information from the acoustic positioning system of the detection units must be transmitted.

3.1 Data Acquisition system

The Digital Optical Modules (DOM) and the Base-modules are submarine nodes of the global networking infrastructure that, comprising the computing resources of the shore-station, form the global Layer 2 network, called RAW-LAN. It is a large bandwidth LAN which, onshore, exploits 10 GbE and 40 GbE interlinks between the switching and computing resources. The DOMs and Base Modules connections to the shore-stations are instead implemented through 1 GbE links. The largest part of the data-stream sent by the detector to shore is called *Fast Acquisition Data* (FAD), containing the digitised signals from the PMTs, samplings of acoustic environment for detector positioning and a continuous stream of summary information sent by each DOM [60]. In fact, DOMs digitise the signal from the PMT as *photon hits*, defined as integrated electric charge of the PMT signal over a certain threshold, the crossing time and the duration of that time over the threshold, and encode it into an optical data frame. Acoustic signals instead, reaching the piezoelectric sensor, are sampled at a constant frequency and compose an acoustic data frame. Once each DOM has completed optical or acoustic frame, it sends them to shore using a UDP/IP protocol. The bandwidth occupied by the slow-control and by other instrument data streams is negligible. The main characteristic of the RAW-LAN network is its asymmetry, originated after the so-called *optical broadcast* (or simply *broadcast*) architecture adopted for the global optical infrastructure. It consists of few downstream optical links broadcasting slow-control commands to the DOMs by dedicated split point, while upstream links (one per DOM) transport the collected data

3.1. DATA ACQUISITION SYSTEM

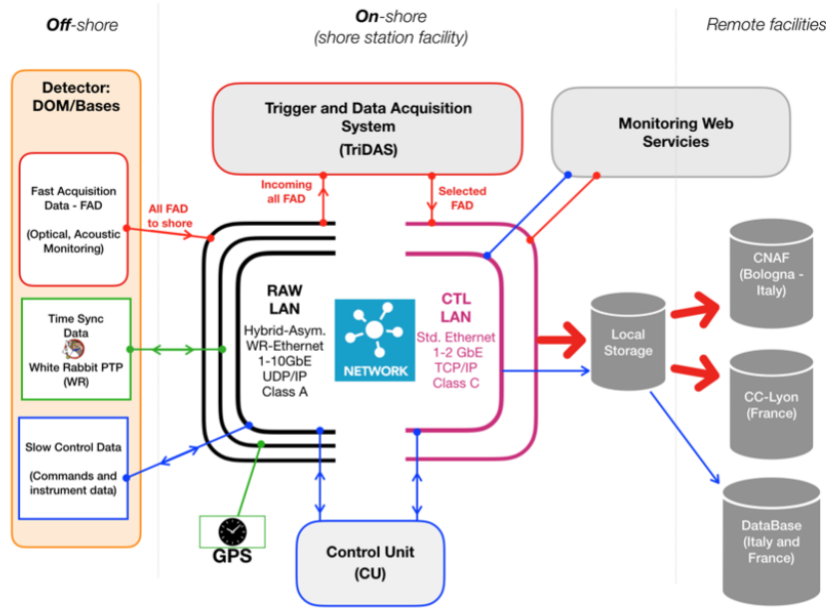


Figure 3.1: Schematic of the DAQ components. Particular attention paid to the network segments and basic elements of the Trigger and computer resources. Figure taken from [61].

to the shore station. It aims at best exploiting the number of optical fibres contained in the many km-long electro-optical cable (EOC) which connects the shore station with the detector. All the DOMs receive therefore the whole information, which can be processed only by the single DOM to which is addressed to. Exploiting these connections, a White Rabbit Switch fabric is used to achieve the required nanosecond synchronisation among the DOMs. The topological asymmetry of the network just described violates the White Rabbit (WR) protocol, therefore a customisation, made by Seven Solutions Company [62], is necessary to optimise and adapt the Master-Slave relation between WRSs and their end-points (i.e. the DOMs and the Base Modules). Lastly the computing farm in the shore-station runs processes that can be subdivided in three groups: the Trigger and Data Acquisition part (TriDAS), the Control Unit (CU) [63] and the monitoring system

[64].

3.1.1 Control Unit

The Control Unit (CU) is a collection of processes and web-servers that represents the user interface to the detector. Among them a dedicated slow control protocol aims to coordinate the TriDAS and the offshore detector. It allows also to start and stop the data acquisition, to segment the operation of the detector in different runs, for which a particular set of configurations for both the DOMs and the TriDAS can be selected. The Control Unit is also responsible for collecting and logging to the central database all the instrument and slow control data. It is composed by the following sub-systems:

- Master Control Program (MCP) is the main user interface and allows to schedule data taking of the experiment;
- TriDAS Manager (TM) guides the computing facility, setting up the TriDAS processes;
- Detector Manager (DM) controls and configures the off-shore detector;
- DataBaseInterface (DBI) provides local database caching and synchronisation with the remote DB;
- DataBaseWriter (DBW) collects instrument and slow-control data and Time Of Arrivals (TOAs) from the acoustic Data Filter (aDF) and writes them to the DB.

3.1.2 TriDAS

The TriDAS is a software collection dedicated to the read-out, aggregation and filtering of the FAD stream which arrives to the shore station. All TriDAS components are interconnected within the RAW-LAN, and managed through the CTL-LAN, which

is also exploited to route the selected data to the storage (local and/or remote) and to publish monitoring data outside the shore-station, as depicted in Fig.3.1.

The first TriDAS stage is an aggregation step, performed by DataQueue processes. Each DataQueue client receives data from a group of DOMs, i.e. a sector of the detector, that are then coherently rearranged according to the precise time interval to which they belong, called Time Slice (TS), of 100 ms and passed to the next TriDAS stage, the on-line filtering processes. These are divided in two sub-groups: the optical (oDF) and acoustic DataFilters (aDF). In this way, each oDF has a complete snapshot of the status of the detector, limited to the TS duration. The selected PMT data is then routed to one DataWriter (DW) process which takes care to write them in a ROOT-based file on a local storage.

Each aDF, differently from the optical case, receives all data from a single DataQueue continuously, thus having the complete time series from a subset of the acoustic sensors. This is required as the acoustic positioning needs to integrate over periods longer than a timeslice. The aim of the aDF is to provide on-line reconstruction of the TOAs of the signals emitted by the acoustic beacons of the acoustic positioning system, in order to compute the position of each DOM with a precision under $\mathcal{O}(10)$ cm. Automatic processes periodically transfer the collected raw-data files to permanent storage devices in the Computing Centres of INFN-CNAF and IN2P3.

3.1.3 Quasi On-Line Analysis and Monitoring system

The Monitoring system comprises a set of programs able to perform fast analysis, visualisation and monitoring of a subset of selected data. A set of plots, continuously update, shows the status of the data taking (PMT and trigger rate counting, fast reconstruction and calibration checks) through a dedicated web-server accessible from outside the shore-station [65]. At the same time the quality of the collected data is checked through programs that run in the background, and properly summarised in the database.

It is composed by:

- ROyWeb which is a web-based program that allows to plot monitored parameters;
- Rainbow Alga which is the 3D event display;
- ROyFit is the fast muon reconstruction software, based on an ANTARES algorithm (further details in the next section).

The software tools described above are exploited not only in the “production sites”, i.e. the ARCA and ORCA shore-stations, but also in different other sites where the detector components are integrated and tested, as well as in test-benches dedicated to DAQ and readout developments. The Automatic Installation And Configuration procedurE (AIACE), was developed to take care of the installation and configuration of all the computing resources required according to a certain experimental setup [66].

3.1.4 RAW DATA LAN

Between the five LAN segments depicted in Fig.3.1, particular attention must be paid to analyse the RAW DATA LAN, which is directly exploited for both data transfer and synchronisation of the detector elements. As anticipated before, the main characteristic of this network layer is the asymmetry arising after the *optical broadcast* architecture. In fact, in the standard WR implementation, a point-to-point connection is established between two communicating devices, which mutually exchange *White Rabbit Precision Time Protocol* (WR-PTP) packets for the time synchronisation. In the KM3NeT context instead, the on-shore master functionalities are split in between the WRS-Broadcast and the WRS-Level1 that share the mastership versus the off-shore endpoints. This architecture is based on WR version 3.3.1 , but the upgrade to more recent versions (4.2 or 5.01) is planned. The switching infrastructure is composed by:

- WRS fabric, which includes WRS-Broadcast plus a number of WRS-Level1 compliant to the number of Base modules;

3.1. DATA ACQUISITION SYSTEM

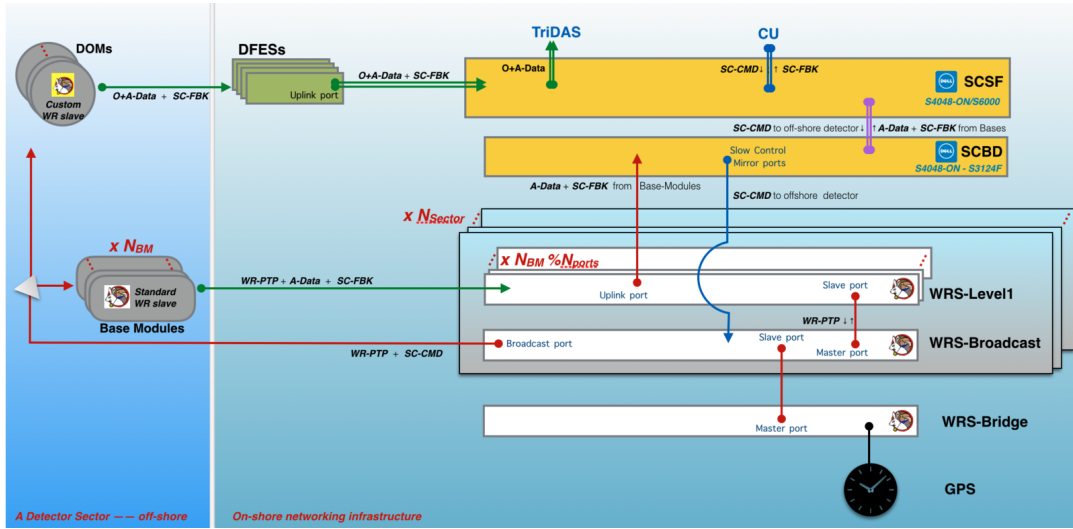


Figure 3.2: Layout of the network connection. Single or double lines represent 1 GbE and 10 GbE connections, respectively. Single directional data-flows are indicated with arrows, while bi-directional connections have only dots. Figure taken from [67]

- Standard Switch fabric, including a number of DOM *Front End Switch* (DFES) elements, sized to host the total number of DOMs; one *Star Centre Switch Fabric* (SCSF) element, which interconnects the TriDAS resources and the optical and acoustic data flows; one *Slow Control and Base Data* (SCBD) element, responsible to connect the standard switch fabric with the White rabbit one.

In order to preserve the stability of the WR infrastructure and reliability of the time-synchronisation mechanism, it was mandatory to minimise the traffic passing through the WRS-Broadcast. This is now possible with the use of a frontier technology, applicable to modern switches, called *Software Defined Networks* (SDN) which is based on the OpenFlow protocol [68]. SDN makes the network programmable by separating the control plane from the data plane. In fact, while traditional switches exploit dedicated hardware appliances that have to be manually configured, SDN technology allows to achieve efficiency and flexibility in managing the entire network as a single unit, for example distributing security information evenly across multiple sites.

3.1.5 Data handling and timeslice

The analog signals produced by the PMT are digitised from the PMT-base board. Here, the analog to digital conversion is finally translated into LVDS signals and routed, via the Octopus boards, to the Central Logic. The front-end firmware is embedded in a Field Programmable Gate Array (FPGA), with a specific hardware logic resource, where 31 Time to Digital Converters (TDCs), one per each PMT of the DOM, are implemented. Each digitises the LVDS signals, obtaining both the arrival time of the pulse and its ToT, creating therefore a *hit*. The TDCs have a dead-time lower than 5 ns, that represents therefore the minimum distance between two consecutive LVDS signals [69]. Once obtained, an Intellectual Property (IP) implementing a state machine organises the data generated by the TDCs, creating User Datagram Protocol (UDP) jumbo frames to be sent to the on-shore station via the CLB optical link. The readout is organised and sent in fixed length time intervals of 100 ms, precisely the “TimeSlice” (TS). Each TS is identified by its start time in Coordinated Universal Time (UTC), contained into a header, and in case of photon data, the subsequent packets contain the photon hits, which are encoded in 6 bytes: 1 byte for the PMT channel, 1 byte for the pulse duration (toT) and 4 bytes for photon hit time with respect to the start of the TS. The timestamps marked in the DOM result from a White-Rabbit PTP core, which implements the White-Rabbit capable Ethernet in the FPGA. If a timeslice satisfies the trigger conditions, meaning that it potentially contains a neutrino event, the hits are collected into a *DAQ Event*, together with all photon hits in the detector in a period of 10 microseconds before and after these hits. These data are sent to the DataWriter which writes all triggered events to file.

3.2 Algorithms for the event triggering

Trigger algorithms, in modern high energy physics experiments, have an enormous importance during data acquisition and data analysis to select events and reduce the background contamination. At the same time it's fundamental to find out the best balance over trigger conditions applied both online and off-line: too loose conditions will cause a large amount of data collected, increasing the computing time and memory usage, but too strict cuts will produce instead an excessive loss of data [60],[48]. The concept of “all-data-to-shore” is at the base of the KM3NeT readout. All the data exceeding a threshold (typically voltage equivalent to 0.3 photo-electrons) are digitised and sent to the shore station. The regarding information is encoded in a pair of values: the start time with 1 ns granularity and the duration of the signal over the predefined threshold, also called *Time over threshold* (ToT), as shown in Fig.3.3. Searching possible space-time correlations between the *hits* is at the base of data reduction on disk [52]. The following criteria are applied to the data on-shore, a part from the first, which is applied off-shore:

- the level-zero filter (L0) is the given threshold for the analogue pulses;
- the level-one (L1) refers to a coincidence of two or more L0 hits from different PMTs in the same optical module, within a fixed time window. The spread of this window is determine by the possible delays occurring in the photon propagation in water, caused for example by scattering, giving typically values of $\Delta T = 10$ ns. The estimated L1 rate per optical module is about 1000 Hz, of which about 600 Hz from ^{40}K decays (in KM3NeT/ARCA environment);
- The level-two filter (L2) is the combination of further L1 hits from different DOMs, exploiting the knowledge of the PMTs orientation inside the DOM itself, reducing by a factor two the data rate.

The basic idea of all the trigger algorithms is that events produce clusters of hits

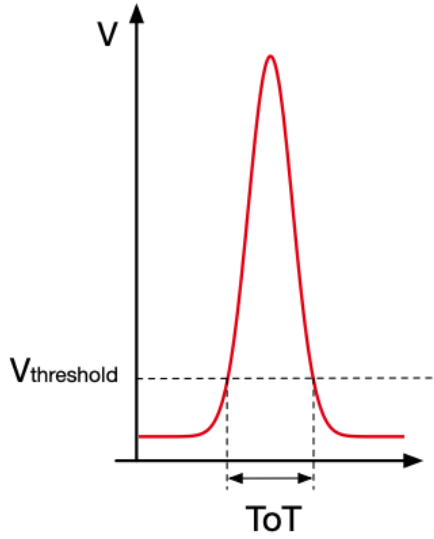


Figure 3.3: Schematic representation of the ToT definition. The time over threshold is measured for the signal which overcome a fixed threshold on the PMT signal. Figure taken from [70].

that are separated in time by light propagation in water, while background light is uncorrelated. The first step is represented by the searching and forming of local clusters of hits that respect the following relation:

$$|\Delta t| < |\Delta r|/c_{water} + T_{extra} \quad (3.1)$$

where Δt and Δr is the time difference and the distance between two hits within a possible cluster, c_{water} the group velocity of photons in water, i.e. $\frac{c}{n}$, and T_{extra} is the additional time window, accounted for timing uncertainties on photon propagation. After this step, to the hit cluster are connected all the other hits that fulfill the following conditions:

- the hits are causally connected to at least 75% of the cluster hits;
- the hits are closer than 50 m to at least 40 % of the cluster hits;

At this point optimised algorithms for different event topology, track-like or shower-like, are operated in parallel on the data: in fact, *Muon trigger* and a *Shower trigger* are defined.

3.2.1 Muon Trigger and reconstruction algorithm

The objective of the event reconstruction is the trajectory and energy determination of ultra-relativistic muons. The main difficulty in the reconstruction of the muon trajectory is the non-linearity of the problem. This is overcome by the use of a pre-fit, providing a suitable set of starting values for the final trajectory fit: this quasi online pre-fit is part of the filtering algorithms at the base of the muon trigger. Apart from providing an excellent up-down separation, this algorithm is very fast and therefore well-qualified for online applications. The starting point are some approximations, like *line shape* detector, neglecting therefore distortions due to sea current, the DOM geometry is considered to be point-like and the muon track is assumed to be a straight line (i.e. multiple scattering is ignored). Except for special cases, like the one in which detector line and muon track are parallel (exactly vertical track), the point of closest approach, called *hot spot*, of the muon track to the detector line can be determined, because most of the Cherenkov light is expected to be seen in proximity of this point. After the step described above of hit clustering, the step of *hit selection* is performed, which aims to avoid random hits from the optical background or scattered late hits. The DOMs belonging to a single string are numbered consecutively along the z-axis, and for a given DOM in position i , the adjacent and next-to-adjacent ones are those at floor $i \pm j$ with $j = 1, 2$. To correlate the hits between these DOMs, the arrival time of the photons must be within the interval:

$$\Delta t < j \Delta z \frac{n}{c} + t_s \quad (3.2)$$

where Δz is the vertical distance between adjacent DOMs, n the refractive index of the medium and t_s the additional time delay. Considering the vertical spacing of the

DOMs in KM3NeT/ARCA of 36 m, and $t_s = 10$ ns, one finds $\Delta t < 170$ ns for adjacent and $\Delta t < 330$ ns for next-to-adjacent DOMs. Using *hot spot* as seed, hits are then added to the list of selected hits. From this point on, the hit selection is based only on timing information. The expected hit times on the string DOMs are calculated by the asymptotes of the hyperbola, in z-t plane as shown in Fig.3.4. At this point the hit

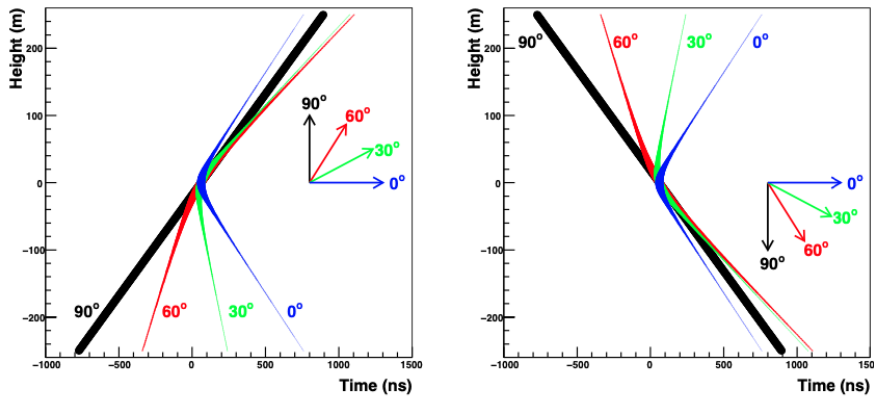


Figure 3.4: The arrival time of Cherenkov light generated by a muon track on a single detector line. **Left:** upward-going muons; **right:** downward-going muons. Figure taken from [71].

finding procedure has finished and the subsequent fitting procedure can start, combining the gathered information from adjacent strings. The particle is assumed to move with the speed of light in vacuum, and its trajectory can be parameterised as follow (see Fig.3.5):

$$\vec{p}(t) = \vec{q} + c(t - t_0) \vec{u} \quad (3.3)$$

where \vec{q} is the point through which the particle passes at time $t = t_0$ and moves in the direction \vec{u} . The track is therefore defined with 5 parameters: \vec{q} and θ, ϕ polar angles defining the \vec{u} versor in spherical coordinates. Considering the string placed at (0,0) point in x-y plane, we are able to determine the parameters of closest approach or *hot*

spot of the muon track to the detector string:

$$z_c = \frac{q_z - u_z(\vec{q} \cdot \vec{u})}{1 - u_z^2} \quad (3.4)$$

$$t_c = t_0 + \frac{q_z u_z - (\vec{q} \cdot \vec{u})}{c(1 - u_z^2)} \quad (3.5)$$

$$d_c = \sqrt{p_x^2(t_c) + p_y^2(t_c)} \quad (3.6)$$

A single detector string is invariant against rotation of the coordinate system around

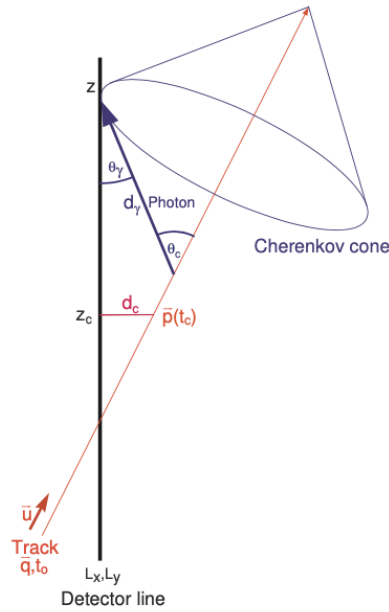


Figure 3.5: Illustration of the muon track trajectory, and of the variables used to parameterise it. Figure taken from [71].

z-axis. This means that the track is fully determined with only 4 parameters. To finally performed the track fit, it is necessary to know the arrival time t_γ of Cherenkov photons at the detector line, their travel path d_γ and their inclination respect to the detector string, $\cos\theta_\gamma$. All these three values can be obtained as follows:

$$t_\gamma(z) = (t_c - t_0) + \frac{1}{c} \left((z - z_c)u_z + \frac{n^2 - 1}{n} d_\gamma(z) \right) \quad (3.7)$$

$$d_\gamma(z) = \frac{n}{\sqrt{n^2 - 1}} \sqrt{d_c^2 + (z - z_c)^2 (1 - u_z^2)} \quad (3.8)$$

$$\cos\theta_\gamma(z) = (1 - u_z^2) \frac{z - z_c}{d_\gamma(z)} + \frac{u_z}{n}. \quad (3.9)$$

Based on eq.(3.7), that represents the analytic expression of the hyperbole depicted in Fig.3.4, the time difference between two hits must satisfy the inequality at the base of the muon trigger:

$$|(t_i - t_j) c - (z_i - z_j)| \leq \sqrt{(x_i - x_j)^2 + (y_i - y_j)^2} \tan(\theta_C) \quad (3.10)$$

where t_i and t_j are the times of the hits, and x, y, z the corresponding coordinates[71]. With the requirement of four (or more) L1 hits, this filter shows a very small contribution of random coincidences, improving the signal-to-noise ratio (S/N) of an L1 hit by a factor at least 10^4 compared to the general causality relation. At this point the offline fit can be carried out with the parameter estimation, performed using the Levenberg-Marquardt method, in which all five independent trajectory parameters are fitted simultaneously. Once the trajectory has been estimated, also the reconstructed energy of the muon E_{reco} can be calculated [72].

3.2.2 Shower trigger

Comparing the evolution of the light inside a cascade with the dimensions of the telescope, typically the emitted light is assumed to be point-like. In order to evaluate the light distribution, in fact, the mean longitudinal development of an electromagnetic or hadronic shower in water must be evaluated, as described in the previous chapter, and its angular emission distribution respect to θ angle and respect to x-y plane, as shown on the left and on the right respectively in Fig.3.6. These contributions allow to define a probability $P^{\gamma,emit.}(\theta)$ for a photon to be emitted with a given angle in the shower development. Its analytical expression was obtained through several dedicated

MC simulations and expressed by [73]

$$P^{\gamma, emit.}(\theta) \propto e^{b \cdot (|\cos(\theta) - 1/n|)^a} \cdot \frac{e^{-d/\lambda_{ass}}}{d^2} \quad (3.11)$$

in which the first term is derived directly from MC, where a and b are respectively $a = 0.35$ and $b = -5.40$, while the second term takes into account the absorption of the photon during the propagation and the distribution over the solid angle ($\propto 1/d^2$). On the left of Fig.(3.6) both these two contributions to the angular emission distribution are evaluated.

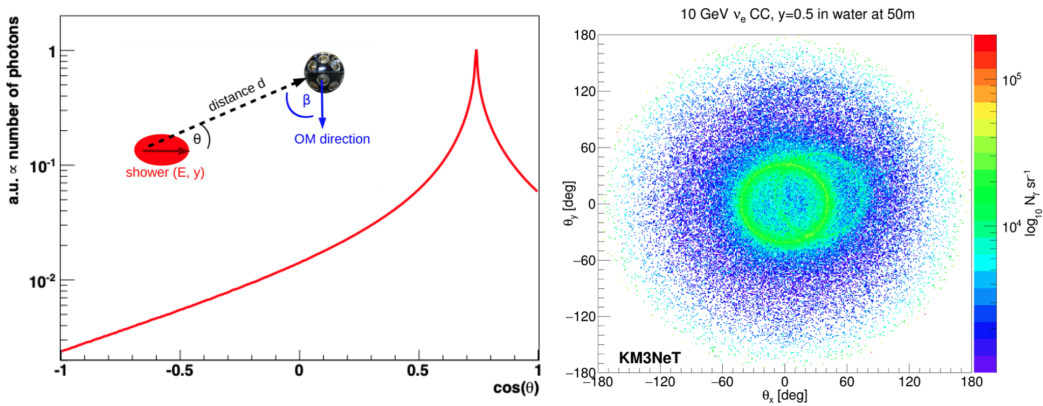


Figure 3.6: **left:** the angular distribution respect to θ angle is shown, taking into account the contributions of eq.(3.11); **right:** the uniform light distribution in the x-y plane derived from MC simulations around the shower axis, for a 10 GeV ν_e . Figure taken from [47].

As a consequence, the maximum photon travel distance (D_{\max}) can be defined, consisting in the maximum distance that a photon can travel, and therefore limiting the possible distance between DOMs. Therefore the maximum time difference ΔT between two causally connected hits separated by a distance d is equal to:

$$\Delta T = \begin{cases} d/c_{\text{water}} + T_{\text{extra}}, & \text{if } d < D_{\max}/2 \\ (D_{\max} - d)/c_{\text{water}} + T_{\text{extra}}, & \text{if } d > D_{\max}/2 \end{cases} \quad (3.12)$$

These conditions help to reduce the number of photon hits to be considered in each event and the width of the time window obtained with the causal relation. The default KM3NeT cascade reconstruction algorithm instead follows two stages; after a fit of the shower vertex based on the hit times, the shower direction and energy are estimated using the distribution of PMTs being hit or not. In the work of this thesis only track-like events are built and emulated with the OctoPAES boards (described in the next section), even if the boards are designed to emulate also shower events. Thus, the trigger algorithm most intensely used will be the muon trigger.

3.3 BCI: experimental setup

The BCI is the acronym for *Bologna Common Infrastructure*. This is a unique setup, overall the KM3NeT collaboration, able to recreate all the data processing effects due to a real implementation of the full DAQ chain inside a controlled environment. In fact, the nature of KM3NeT detectors, being at a depth of ~ 2500 m and ~ 3500 m under the sea level, and the modularity required for their construction, makes of this laboratory a central node for testing new developments before the final deployment. The BCI offers a full detection unit (DU) size test bench, as shown in Fig.3.7, comprising therefore 18 CLBs acting as DOMs, 1 CLB acting as DU-Base and all the electronics and power supply required for the correct functioning of the apparatus. The Base is powered via a dedicated board, implying the use of a 375 V power supply, then branched to the “backbone” segment, which supplies, in real implementation, all the DOMs within the string, but here powering only one DOM-CLB 6 (availability of only 1 DC/DC converter). The rest of the CLBs are independently powered by means of a ELC 12V-25A power supply. Respect to the ones deployed at the bottom of the sea, the BCI DOMs are missing the outer casing, the pressure resistant glass sphere, all the PMTs and related PMT bases and the two electronic boards deputy to the connection of the PMT bases

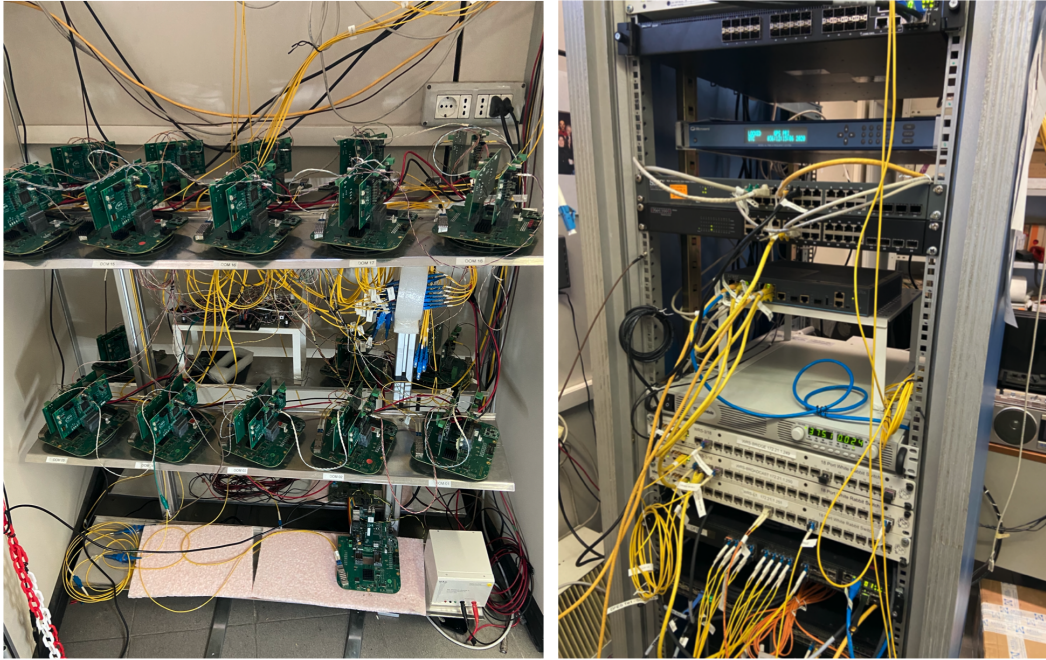


Figure 3.7: **left:** phase-1, 1 DU size test bench at the BCI, with the OctoPAES system implemented and wired; **right** The rack-mountable elements (switches, White Rabbit, GPS, power-supply) properly placed on rack.

to the CLB, called Octopus. Inside a real DOM the Octopus LARGE connects 19 PMT bases placed in the bottom hemisphere, and the Octopus SMALL connects the remaining 12 PMT bases in the upper hemisphere. Moreover all the optical connections from the DU to the on-shore station are implemented, and are compliant to the Broadcast scenario. This means that the optical fibre line, coming from on-shore, is split off-shore at the level of each CLB. Instead dedicated optical lines are built from each CLB back to the on-shore switch fabric. In order to recreate the delays produced by the signal propagation inside the kilometre long electro-optical cable running on the seabed, specific delay elements were introduced. Inside the BCI laboratory is also implemented all the network infrastructure, corresponding to all the processes required to transport UDP packets from the computing farm to the DU and viceversa. A schematic overview

of the BCI connections between the DU and the on-shore station is depicted in Fig.3.2. On-shore the networking facility is composed by:

- 1x GPS;
- 3x White rabbit Switch (Bridge, WRS-Broadcast, WRS-Level1);
- 1x DELL S4048-ON which implements the SDN of instances “SCSF” and “SCBD”;
- 1x DELL N4032F which acts as a “DFES”.

The White Rabbit Switches (WRS) are at the core of the *ns* time synchronisation of the CLBs. The master clock is generated by a GPS receiver installed on-shore with a frequency of 10 MHz. It is provided to the WRS fabric. On its turn, the WRS broadcast distributes to the CLBs the clock information, and the Pulse Per Second (PPS) that is reconstructed inside the FPGA of the CLB. The clock information and the PPS are encoded according to the Synchron Ethernet standard, within the WR-PTP packets. To pass the digital information to the CLB, optical transceiver are used in order to allow a continuous communication with the on-shore hardware through the system of optical fibre. The CLB is at this point able to reconstruct the clock through the implementation of a Phase Locked Loop (PLL). The sub-nanosecond synchronisation achieved, allows to time correlate detected events between the various CLBs. For this reason, the CLB timestamps the data sent on-shore.

For what concerns the computing resources implemented at the BCI, they are organised according to the production structure as shown in Fig.3.8:

- a BCI bastion server that is the portal for users and the hypervisor of the virtual machine to the SDN controller (ssh km3net@fcmserver2.bo.infn.it);
- a Control Unit server hosting CU services, described in the previous section (ssh km3net@bci_cu);

- a DAQ server hosting the DataQueue, JDataFilters, the JDataWriter, the JLigier deputy to the transfer the selected data from any DataFilter to the Data Writer, the acoustic data filter and the CLBSwissKnife for monitoring the status of the CLBs (ssh km3net@bci_daq1);
- a SDN controller server;
- a monitoring server installed on a virtual machine on the bastion (ssh km3net@supernova).

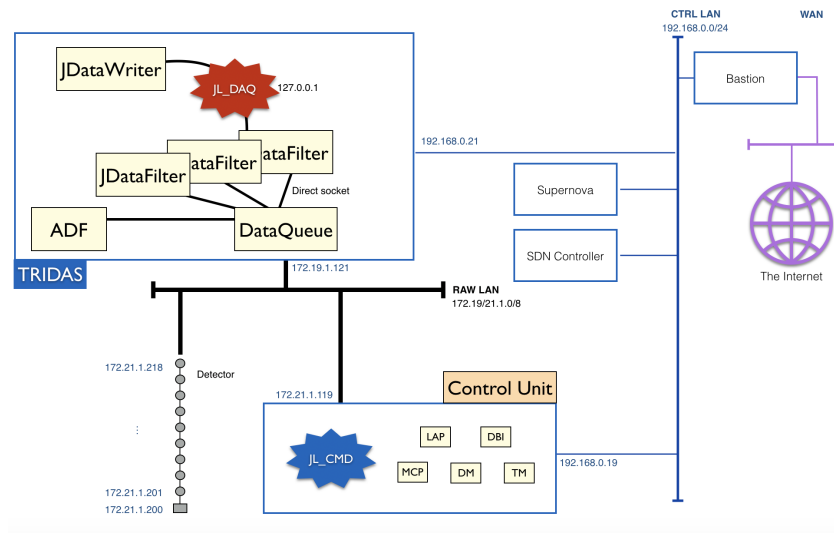


Figure 3.8: Schematic representation of the network topology implemented at the BCI laboratory.

3.4 OctoPAES

The OctoPAES boards were developed by the KM3NeT collaboration together with the Bologna INFN electronic section, in order to emulate, in the context of the BCI, the behaviour of the corresponding PMTs and Octopus boards of the standard DOM



Figure 3.9: In this figure is shown an OctoPAES board, with the specific connector, the dip switch and all the hardware implementations.

implementation. The name in fact is the acronym for *Photon and Acoustic Emulation of Signals*, outlining therefore the possibility to emulate optical and acoustic signals. As in the DOM, where the Octopus Large and Octopus Small are needed, at the BCI test bench each CLB hosts two OctoPAES boards, plugged into the CLB with the same specific connector (10M04SCE144I7G) of the Octopus boards, emulating signals for 19 (OctoPAES LARGE) and 12 (OctoPAES SMALL) PMTs respectively. The OctoPAES board can be configured in Large or Small mode, thanks to a dip switch mounted on it. For what concerns the emulation of the PMT signals, the OctoPAES boards allow to select among different PMT single-rates and to provide the user with per-PMT configurable hit patterns encoded in the so-called MIF file. It is a binary file that is uploaded in the ROM of the board, during the flashing of the firmware inside the CPLD. The file is organised in 128 pages, each one containing 32 rows. The first 31 rows correspond to the 31 PMTs of a DOM. The 32th row is left for the implementation of the waveform for the acoustic emulation (which is not discussed here). Each row comprises 256 digits. In the case of the PMT signal emulation, each digit represents a tick of the OctoPAES

clock, which operates at 80 MHz, so a tick corresponds to an interval of 12.5 ns. By switching the due digits from 0 to 1, it is possible to recreate inside the same DOM, and in between different ones the hits as if they were caused by the passage of a muon with a precise direction. The rate of injection of these hits in the BCI DAQ system can be set by outside, simply changing a jumper on the board, and selecting some predefined frequencies, typically 1, 100 Hz or 1, 5 kHz. It is important to highlight however that the signal injection is not continuous: in fact the time available for the emulation of the hits on a single PMT is $3.2 \mu\text{s}$ ($256 \text{ digits} \times 12.5 \text{ ns}$), while with an injection frequency of 5 kHz this corresponds to a period of $200 \mu\text{s}$. At the same time considering the usual time segmentation made by the CLB, in TimeSlices (TS) of 100 ms, however an high payload on the system can be produced, with 500 bunches of data injected for each TS. Of particular importance, in order to have a hit emission over different DOMs/CLBs coherent with a general and computed time structure, is the time calibration of all the 36 OctoPAES boards (2×18 CLBs). Moreover, both the white rabbit protocol and the physical delays of a particle inside the detector requires a synchronisation of the order of at most tens of ns. Further information on the strategy adopted to calibrate the system will be given in the next chapter.

3.4.1 OctoPAES firmware and wiring topology

The main contributions of my thesis work consisted of the design, the implementation and the tests of different versions of the OctoPAES firmware for different layouts of connections between the boards. In particular, I aimed at verifying the robustness of the system and its stability and reliability in terms of time-synchronisation between the emulated data. I worked in tight cooperation with the Electronics Laboratory of INFN-Sezione di Bologna, where the OctoPAES boards were designed. The following list shows the evolution of the BCI setup since the beginning of my thesis. My activities covered all the described stages, which relate to the various changes in the OctoPAES firmware

and the consequent changes in the experimental setup. Items from 1 to 4 were actually realised and represented the core part of my experimental work at the BCI. Item 5 refers to a completed design, although its implementation is still under finalisation, and represents the outline of the setup evolution.

1. OctoPAES in Master stand alone mode (i.e. an internal clock is used; the hit emulation is started and stopped by pressing the due button on the board panel). The implemented firmware includes a simple state machine providing only “running” and “not running” modes. In running state, the hits are emulated always at a constant rate, determined by some jumper position on the board panel, allowing the following values: 5 Hz, 10 Hz, 1 kHz 100 kHz. The purpose of this firmware is that of generating a constant data-stream for testing the performance of the DAQ system under different throughput.
2. One Master to many Slave OctoPAES boards. The clock distribution is implemented in daisy-chain, with the OctoPAES Large on CLB 1 acting as a Master. The start and stop signals for hit emulation is propagated by piggybacking the clock distribution, via special embedded signals;
3. all Slave OctoPAES boards. In this configuration, a further board is required to distribute the clock and the start/stop signal. We realised this new Master board by means of a Kintex KC705. The clock is still distributed in daisy-chain, while the start and stop signals are triggered via parallel connections of the Kintex board to all the OctoPAES boards;
4. still all Slave OctoPAES boards and KC705 as Master, but clock and start/stop signals distributed through parallel connections.
5. the same hardware setup as in point 4. In this version of the firmware, the state machine is modified in order to switch between background and signal hits emu-

lation, properly alternating the due MIF pages. In order to reproduce a standard condition as measured with the KM3NeT/ARCA telescope, the background hits are emulated at the rate of 5 kHz while the signal hits are added at 1 or 10 Hz.

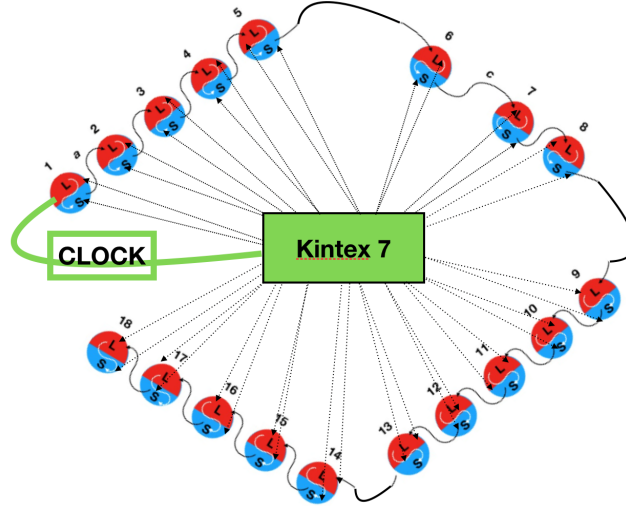


Figure 3.10: Schematic overview of the connections implemented for the OctoPAES system, with the external KC705 board acting as a master, and transmitting the start/stop signal in parallel.

As described below, the validation of the OctoPAES effectiveness with firmware n.2 revealed a big issue due to the synchronisation of the start/stop of hit emulation along the boards. For this reason we decided to introduce an auxiliary board, the Kintex KC 705, accomplishing with two tasks: act as source of the clock to be distributed to the OctoPAES according to a daisy-chain scheme; triggered the emulation start/stop to the OctoPAES via dedicated parallel connections, as shown in Fig.3.10. We used two complementary investigations to check the performance of the implemented firmware, focusing on the relative delays among the hit emulated by the OctoPAES boards with respect to the first one in the daisy-chain. The first check consisted of direct measurements performed with the oscilloscope: probes were connected to specific check-points

on the OctoPAES CPLD pins to measure the hit emulation time. The second check consisted of analysing the data recorded in root-files at the end of the on-line processing chain by the TriDAS. For this purpose I've developed a dedicated set of software tools written in Python, which will be further described in detail in Section 3.4.2.

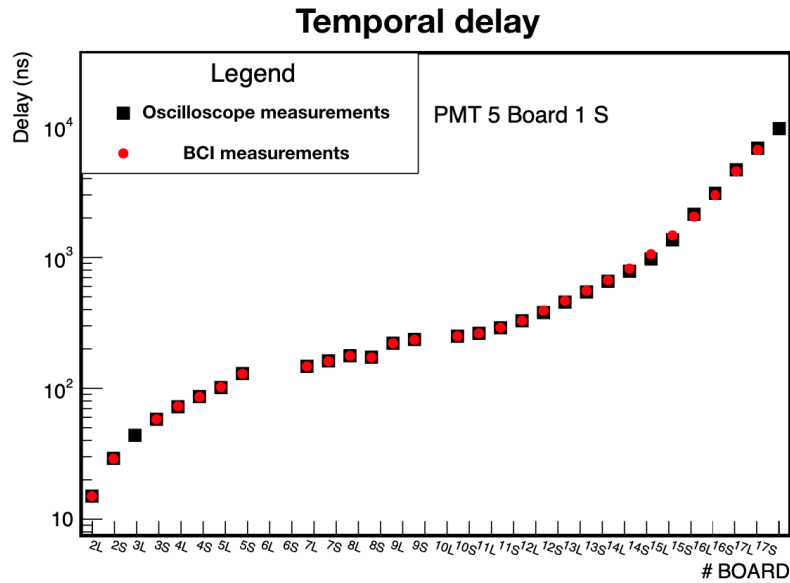


Figure 3.11: Relative delays of the hit timestamps emulated by different OctoPAES boards (L = Large, S = Small) with respect to those from OctoPAES Small PMT 5 mounted on CLB-DOM 1.

Applying direct and software measurements within the layout scenario n.2 led to the same results: increasing delays were measured as progressing along the daisy-chain, growing larger than some microseconds, as shown Fig.3.11. Although we put in evidence an important flaw in the system design, thanks to the described checks I could validate the effectiveness of the developed tool for measuring the hit delays with a software analysis approach. The use of my software tools boosted the measurement sessions with respect to the use of the oscilloscope. A significant improvement was introduced with the parallel distribution of start/stop from the KC 705, i.e. scenario n.3 of the above

list. As shown in the left panel for Fig.3.12, the spread among the relative delays was now limited within 20 ns. Another problem encountered in the firmware development was reaching the reproducibility of the delays after stopping and restarting the system. The right panel of Fig.3.12 reports the difference among delays calculated before and after the stop/restart of the OctoPAES system. The red box highlights a shift of 12.5 ns (i.e. a clock tick) for two OctoPAES boards after a stop-restart cycle.

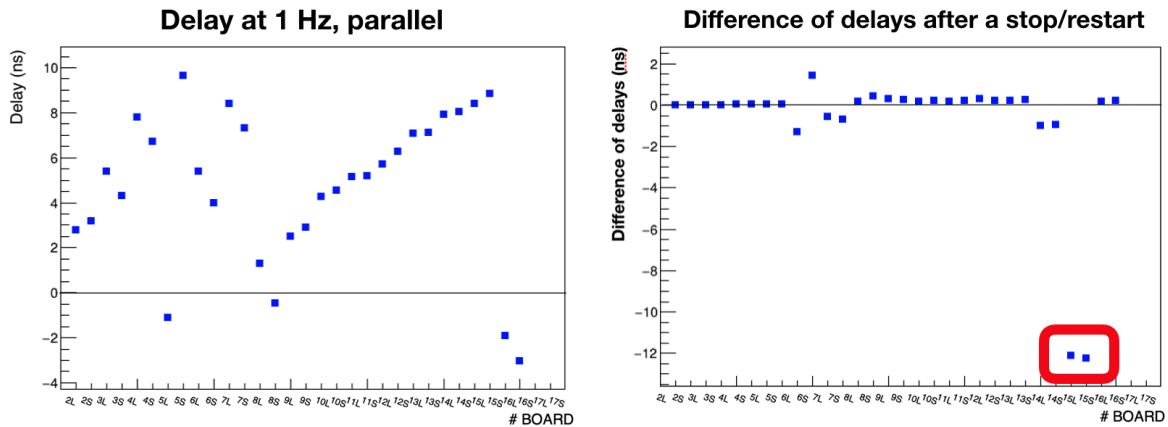


Figure 3.12: **left:** Delays of the OctoPAES boards respect to the reference one (DOM 1, LARGE). **Right:** difference of the delays, calculated before and after a stop/restart procedure of the OctoPAES system.

We finally solved this problem by optimising, in the OctoPAES firmware, the recognition mechanism to detect the start/stop pattern emitted by the KC705. In order to facilitate the visualisation of the results of the various attempts, I developed a dedicated monitoring software which analyses on-line the relative delays between the hits injected by the various OctoPAES. As output the program produces plots that are published on the Web by a dedicated web-server. Fig.3.13 shows an example of the monitoring plots (major details are reported in the caption of the figure). The monitoring program is kept running during a stop and restart of the OctoPAES system allowing to register the delays before and after the procedure: the purple vertical lines indicates respectively the

stop and restart time, and the blue dots are the measured delays. The same procedure

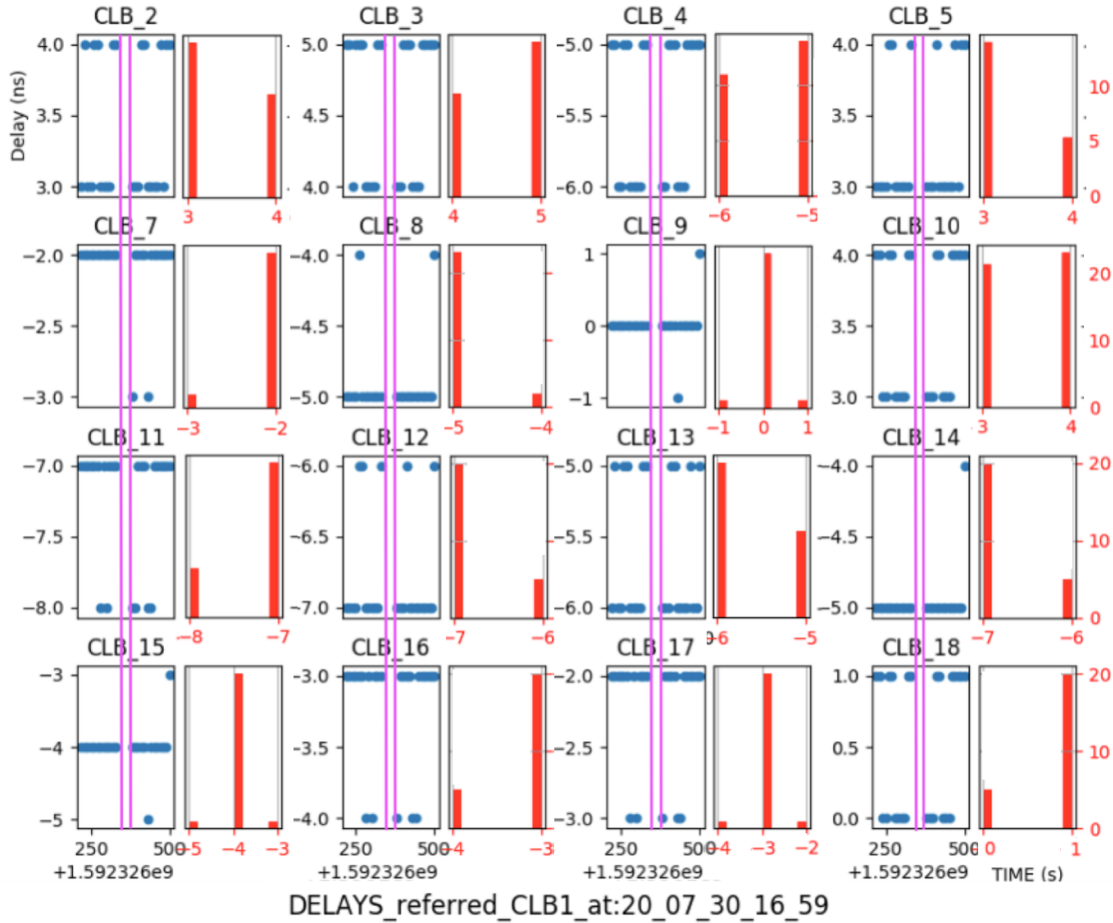


Figure 3.13: Online analysis program developed for the monitoring of the delays of the OctoPAES boards. In this case the purple vertical lines highlight the stop and consequent restart of the OctoPAES system.

was repeated during a power-cycle of the entire DU: also in this case the delays remain constant. In this way we demonstrated to have realised a stable mechanism for distributing the start and stop signals to the OctoPAES boards. This point is essential to deterministically relate the timing of the injected hits among all the OctoPAES boards.

A further optimisation of the firmware concerned the clock distribution mechanism. As previously described, in version 3 of the firmware the clock is distributed in daisy-chain, and each OctoPAES, thanks to a phase locked loop implemented inside its own CPLD, is able to reconstruct this clock signal and to keep the phase constant. The distribution to the next board at this point can be made: (i) in serial mode, waiting for the locking of the board that in turn re-generates the clock with the same phase respect to the original, or (ii) in parallel distributing to all the boards the same original clock, but with the possibility of a signal degradation, specifically on the most distant boards in the chain. In order to reduce the dead-time, needed to each board to lock its own clock to the receiving clock phase, this supplementary parallel configuration for clock distribution was tested and finally chosen as valid. Eventually, it was evaluated also the possibility to extract the clock signal for the OctoPAES boards directly from their own related CLB to which they are connected. Indeed, all the CLBs of the setup are synchronised by the White Rabbit infrastructure, as already explained in Section 3.1.5. However some CLB hardware constraints and some problems, in the possible observation of the micro-OOS (explained in detailed in the next chapter), made us discard this possibility.

3.4.2 Online delay display tool

Fig.3.14 shows the processing chain applied to the optical data-stream by the on-line data acquisition system (the TriDAS, described in Section 3.1.2) and other processes for the (quasi-)online analysis running on the computing facilities of the shore-station.

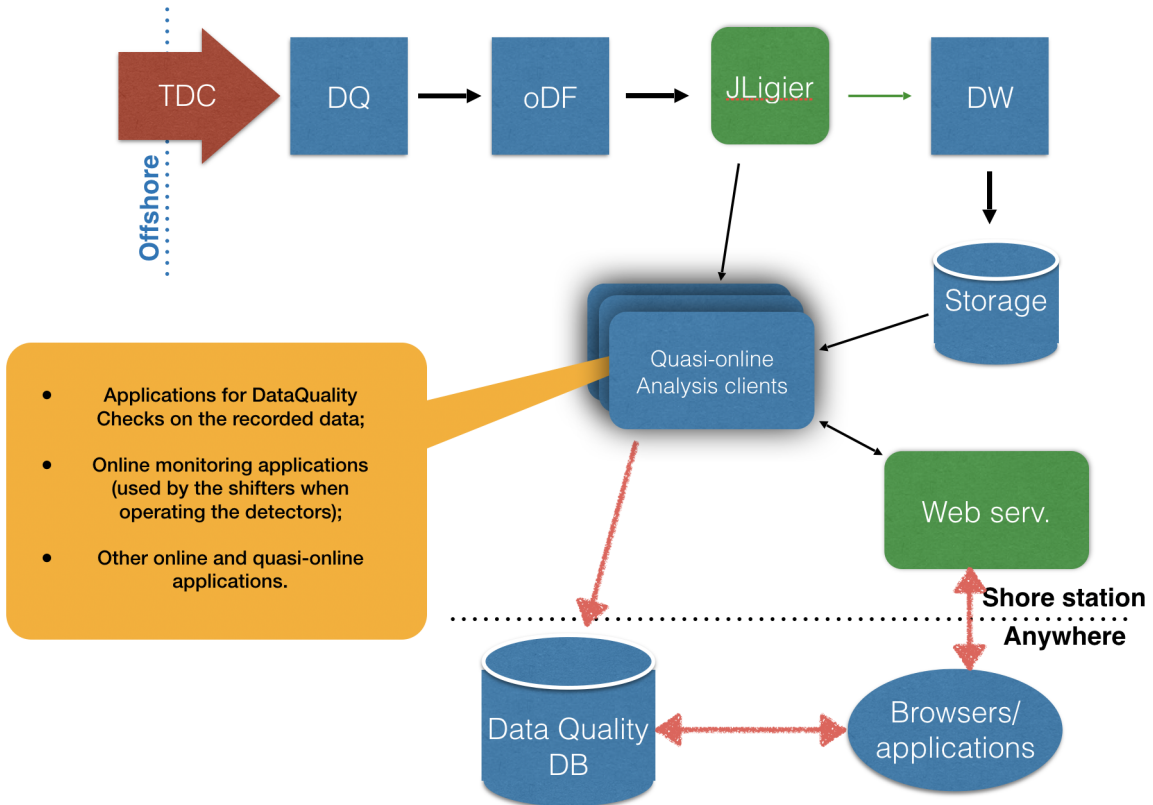


Figure 3.14: Flux of the data: the TDC information passes through the DataQueue, the optical DataFilters and to the JLigier. Finally the data are sent to the DataWriter and written on disk. The online analysis clients interface with the JLigier and retrieve the required information.

It is noteworthy the pivot role of the JLigier process, represented in a green box in Fig.3.14, which handle the incoming information and distribute it on a number of clients. The JLigier is a dispatcher client, which connects processes according to a “many (m)

Tag	Description
IO_TSL0	information on all the hits in a given Timeslice
IO_TSL1	only those hits that are seeds of L1 trigger algorithms
IO_TSL2	only those hits that are seeds of L2 trigger algorithms
IO_EVT	all the hits associated to track-like or shower-like events
IO_SUM	summary information concerning the parameters which characterise a Timeslice (i.e. hit-rate/PMT/DOM)

Table 3.1: Tridas tag with a brief description of the data stream associated.

to many (n)” $m : n$ protocol over Ethernet. The JLigier is capable to multiplex the distribution of the same information to multiple destinations, according to the due tag subscription.

Part of the work of this thesis was just focused on the development of an online tool capable to measure the time delay among the OctoPAES boards. The python program developed was implemented within one of the most common and used software framework for analysis, developed by KM3NeT collaboration : KM3Pipe [74]. It is capable to connect to the BCI JLigier, and gather all the information with the specified tags as they are defined in the TriDAS (see Table 3.1).

The information retrieved from the JLigier is parsed, according to the data format implemented in KM3Pipe, and combined in order to extract the delay values between the hits of a given channel of a generic OctoPAES board and a reference one. In particular, the chosen reference channel was n.12 of the CLB n.1, i.e. from the related “Large” OctoPAES board. For this purpose I created a dedicated MIF file capable to produce simultaneous hits only on channels 0 (OctoPAES Small) and 12 (OctoPAES Large). It was chosen a hit injection frequency of ~ 5 kHz (to be precise 5,31 kHz) for all the OctoPAES boards, which implied the generation of 530-531 hits per TimeSlice (of duration of 100 ms) from each OctoPAES board. The measurement of the delay of a channel with

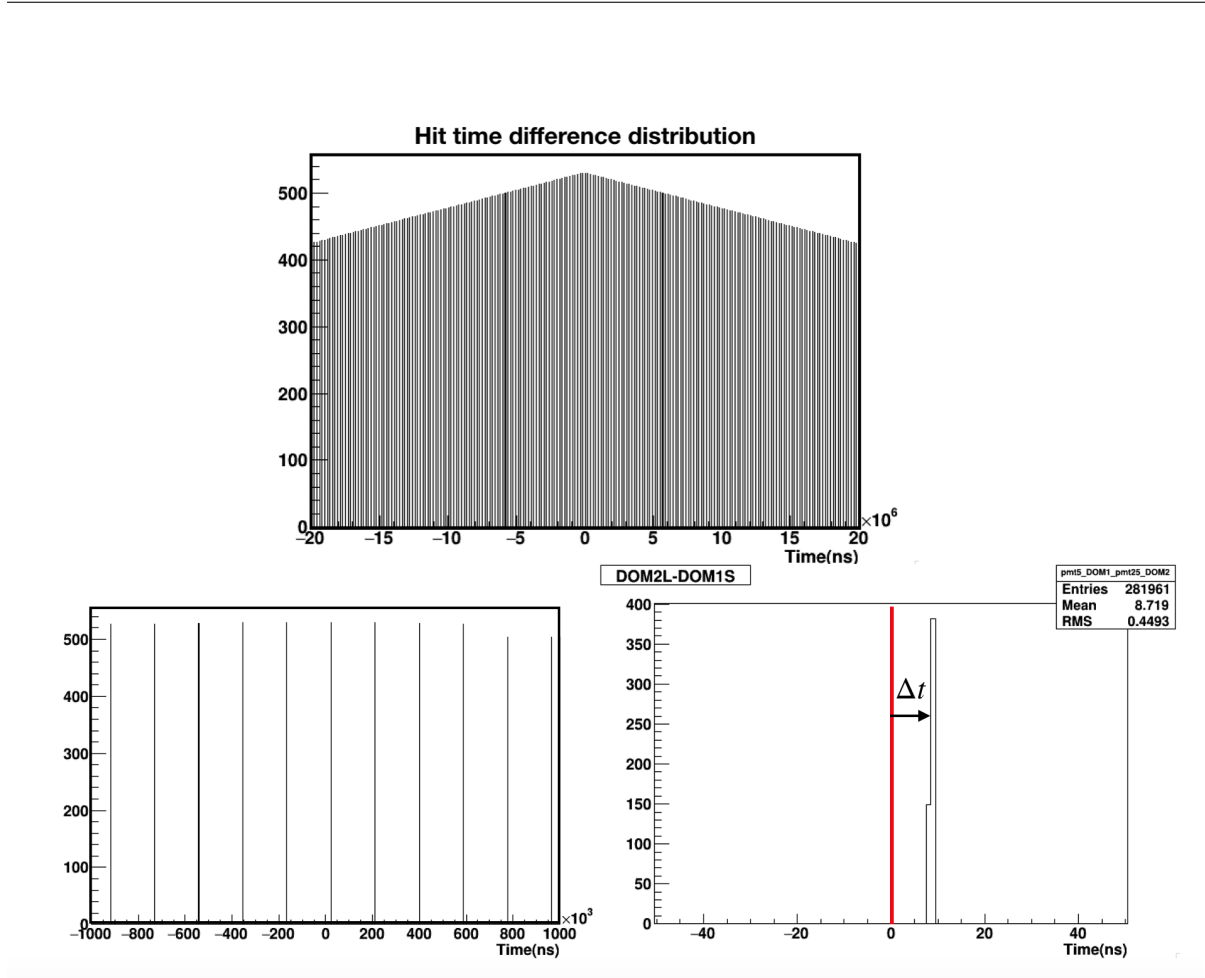


Figure 3.15: **top:** triangular distribution obtained from the difference of the time-hits on a generic OctoPAES board respect to the reference board, chosen to be 1L; **bottom-left:** Zoom in a symmetric set around zero, looking at the peak-to-peak distance just equal to $200\mu\text{s}$; **bottom-right:** central peak of the distribution, evaluating its shift respect to zero reveals the delay of a given board respect to the reference one.

respect to the reference one is performed in the following way: for each TimeSlice, it is computed the the time-difference of all the hits of the tested channel with respect to all the hits of the reference channel. Collecting the results in a histogram, a triangular distribution, as that shown in Fig.3.15, is obtained.

Zooming into the region around 0, as shown on the bottom of Fig.3.15, it is apparent

that the hits are separated by $200 \mu\text{s}$, which confirms that the actual hit-rate is 5 kHz, according to the MIF design. This also means that the DAQ system itself does not introduce any possible macroscopic shift or delay in the data. The searched delay is obtained by measuring the distance in time of the distribution peak and zero.

The program allows to set the frequency of the measurement. For our tasks we found convenient to analyse one TimeSlice per minute, and to produce a summary plot, as that shown in Fig.3.13 every hour. The plot is then loaded in a repository which is made accessible from a dedicated web server also from outside the local network of the laboratory.

In case of extended data taking, lasting even for days (e.g. see Section 4.3 about the search for the Micro Out-of-sync) we needed to keep monitoring the hit-delays for long duration runs. For this reason, I had to improve the performance of my software: by means of dedicated circular buffers algorithms, I optimised the memory usage on the machine where the program was executed. The code of the developed software is maintained and available from the the following GIT repository [75].

Chapter 4

Emulating neutrino induced muon tracks with the OctoPAES boards

The Bologna Common Infrastructure (BCI) test-bench offers a unique opportunity to test and validate new updates, concerning off-shore electronics, the on-shore hardware and the network facilities and all software tools deputed to the detector control and to the data readout. At the same time, with the introduction of the OctoPAES boards, lots of possibilities have been opened. In fact, thanks to the possibility to design and implement the wanted patterns of the photon hits (as well as the acoustics signals) that are injected in the DAQ system by several CLBs, the emulation of the main features of one detector string are reproduced almost realistically in the BCI test-bench. In particular, trigger performances for single string detector, nanosecond time synchronisation and its stability over long periods can be evaluated. Among them, particular attention was paid in attempting to reproduce one of the main issue of DAQ system, discovered in KM3NeT/ARCA telescope: the micro Out Of Synchronisation (micro-OOS) issue. It consists of an erratic loss of synchronisation of the DOMs with respect to the reference timing provided by the GPS and distributed by on-shore White Rabbit switching infrastructure, producing therefore a loss in trigger performances. The nanosecond time

synchronisation is fundamental to perform effective space-time correlations among the detected hits, and to identify those that are possibly due the muons or showers from the interactions of primary neutrinos.

4.1 Micro-OOS issue

The peculiar asymmetry developed for the optical broadcast scenario is based on a customisation of the White Rabbit (WR) protocol made by Seven Solutions. The WRS-BC (broadcast) and WRS-L1 (Level-1) are just customisation of the firmware, derived from the standard WR release, based on v3.3.1. Naturally new WR firmware releases have been developed during the years, and recently a stable one was released, v5.0.1, but it has not been yet used as reference for KM3NeT customisation. The micro-OOS issue is a problem which affects the synchronisation of the DOMs when using a WRS-BC based on v4.2. This phenomenon was found in KM3NeT/ARCA shore station, the only site where was tested. It consists of $\mathcal{O}(1)$ μs size de-synchronisation of DOMs respect to the common timing distributed from the GPS, with a variation back/forth with respect to the event time. It was noticed that this issue typically occurs not in a precise moment respect to the starting time of the run, but within 3 days before the last power-cycle of the DU.

Event time residual The first technique used to discover and study the micro-OOS issue was the event time-residual. Considering in fact track-like events, the resulting muon trajectory can be fit as a straight line. The best fit obtained in this way is called *best-track*, and it's possible to compute the timings that would be recorded from the related emission of light, called *best predicted timings*. If the best track was exactly equal to the real particle trajectory, the timing difference between the best predicted timings and the measured ones would be always equal to zero. This difference is just called *time residual*, and usually is distributed around zero, as shown in Fig.4.1.

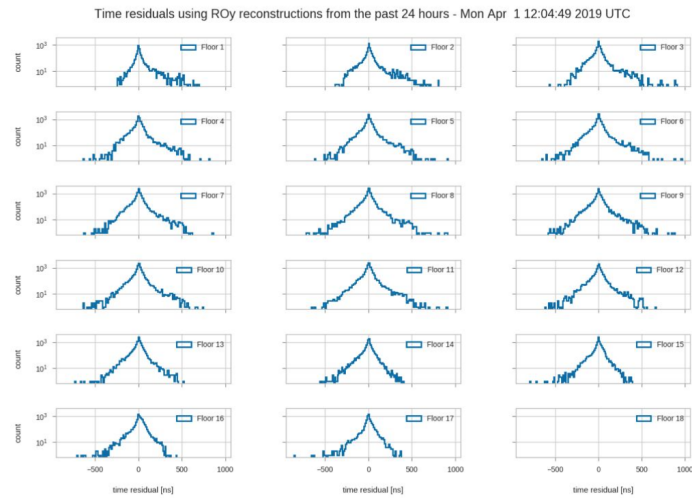


Figure 4.1: Time residual distributions for the 18 DOMs within a string. All the distributions are peaked precisely at zero, indicating the correct functioning of the time synchronisation.

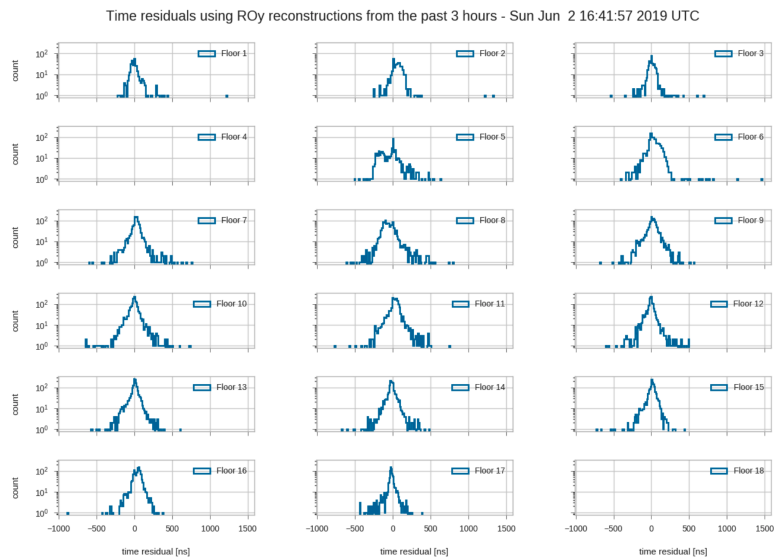


Figure 4.2: Time residual distributions for the 18 DOMs within a string. Some of the distributions present some peculiarity as: widening of the central peak or just a second peak, not centred on zero. This indicates the presence of the micro-OOS issue.

When the micro-OOS occurs, one or more DOMs lose the synchronisation, producing hit times constantly shifted of a given quantity which is usually of $\mathcal{O}(1) \mu s$, but which was observed even up to few ms. This peculiarity produces in the residual distribution a widening of the central peak, or for example the appearance of a second peak, as shown in Fig.4.2.

DOM and Base CLB firmware A small digression on the differences between CLB-DOM and CLB-Base firmware is needed in order to explain the successive tests undertaken. In fact, the CLB-Base firmware was developed following the connection scheme on the left of Fig.4.3. It undergoes with the name of *Full WR loop connection*, and was developed considering the CLB-Base as a pure WR-slave. The CLB-DOM firmware

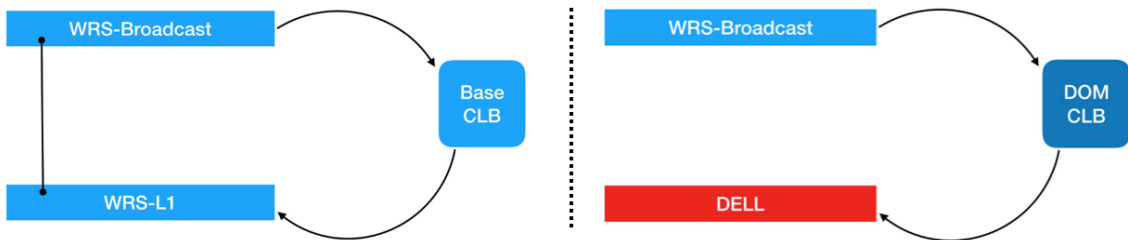


Figure 4.3: left: WR Loop connection for the CLB-Base, that in this configuration is a pure WR slave. Here the “loop” consists of the circular routing of the WR-PTP packets that are exchanged and processed by the three elements: on-shore, the WRS Broadcast and L1 which, both, act as Master to the Base CLB, which is the off-shore slave endpoint. **Right:** hybrid implementation of the CLB-DOM connection. Here the “WR Loop” is interrupted at the DOM: WR-PTP packets are sent by the WRS-Broadcast to the detector off-shore, but the DOMs do not reply with any WR-PTP back to shore. The traffic from the DOMs is addressed to a different switching fabric, represented by the standard switch DELL.

instead was modified in order to speed up the *Link-up* phase, whose duty is to finalise the

initialisation of CLB-WR state machine. Differently from CLB-Base, the DOM is not yet anymore a standard WR-slave node. In fact, it does not send any WR-PTP feedback to WRS-L1 to allow fine-tune phase-corrections. Such a scenario divert from the standard WR concept, and from the broadcast scenario, that guarantees the self-calibrating sub-nanosecond timing. This allows however to route the data from the DOMs directly to a standard switch, as shown on the right panel of Fig.4.3.

Preliminary tests After the appearance of the micro-OOS, multiple tests were conducted in the ARCA shore station to better constrain the problem. The issue appears just with the introduction of WRS custom firmware based on v4.2. An hardware issue however was excluded during the tests with the usage of a second brand new WRS with the same implementation of the v4.2 WRS release. Putting back in place the old WRS, based on v3.3.1, produced the disappearance of this issue, suggesting that it is strictly related to the WRS-BC v4.2. A first test was done by Seven Solutions, with a setup compliant to the Full-WR loop, as depicted on the left of Fig.4.3. A pair of WRS-BC/L1 v4.2 was used, and a SPEC Board with the CLB-Base firmware installed on it. The test was carried out for 15 days, measuring the delay between the PPS sent by the WRS-BC and the one reconstructed by the SPEC board. Fig.4.4 shows 5 continuous days of data-taking, during which the measured delay showed that no micro-OOS was reproduced.

The test proved that micro-OOS does not affect WR-slave included in the Full WR Loop, like the CLB-Base. Thus the possible origin of the micro-OOS issue is due probably to a mismatch between the WRS-BC v4.2 and the CLB-DOM firmware. For this reason further tests have been conducted at the BCI. We repeated the same test done by Seven Solution at the BCI, measuring this time the delay of the PPS between two consecutive CLBs (n.3 and n.4). This test produced again a constant value of $\mathcal{O}(100)$ ps, over periods of several days, partially excluding the CLB-DOM firmware and the hybrid configuration

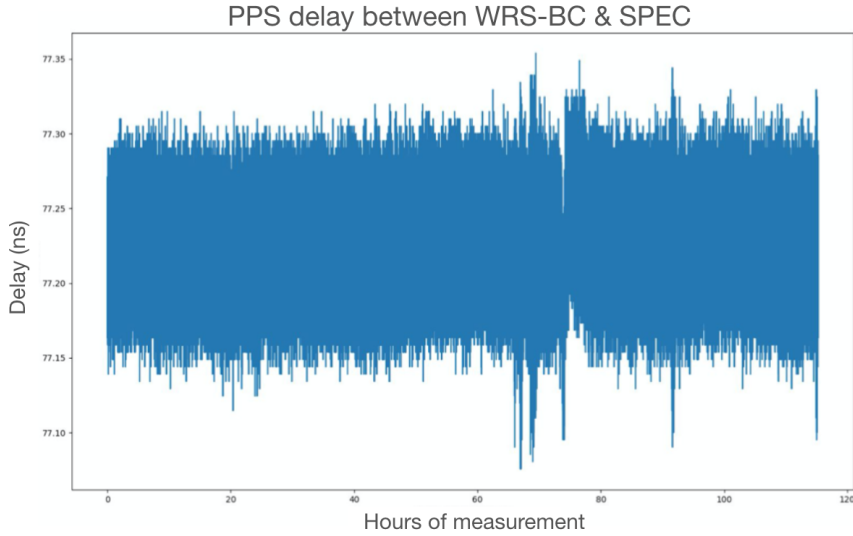


Figure 4.4: Seven Solution measurement of the PPS delay between the WRS-BC v4.2 and the SPEC board implementing a Base-like f/w. The delay remains constant at ~ 77 ns, assuring that no micro-OOS has occurred.

as cause of the micro-OOS issue. Other investigations carried out will be deepen in the next sections, but were all directed to look for the appearance of the micro-OOS under different and various data-taking conditions capable to stress the detector and the DAQ system. In particular, the evaluation of its appearance in correlation to a greater number of working CLB-DOMs, or in correlation with a critic throughput coming from the CLBs, and just modulated thanks to the OctoPAES boards.

4.2 Muon emulation and MIF

The OctoPAES boards offer the possibility to manipulate the injection of photon hits in the TDCs of the CLB. This provides us with the opportunity to try to recreate the micro-OOS issue testing different data-taking conditions and payloads for the DAQ system, and also the possibility to emulate events as if they were caused by the passage

of a real particle, but in a controlled and accessible environment as the BCI. The time signature of the different events are encoded in the MIF file: a binary format loaded in the ROM of the OctoPAES board during the flashing of the firmware.

4.2.1 MIF file

The MIF file is the way through which the calculated physical properties of an event are encoded in a binary format and injected in the OctoPAES+CLB system. It is a

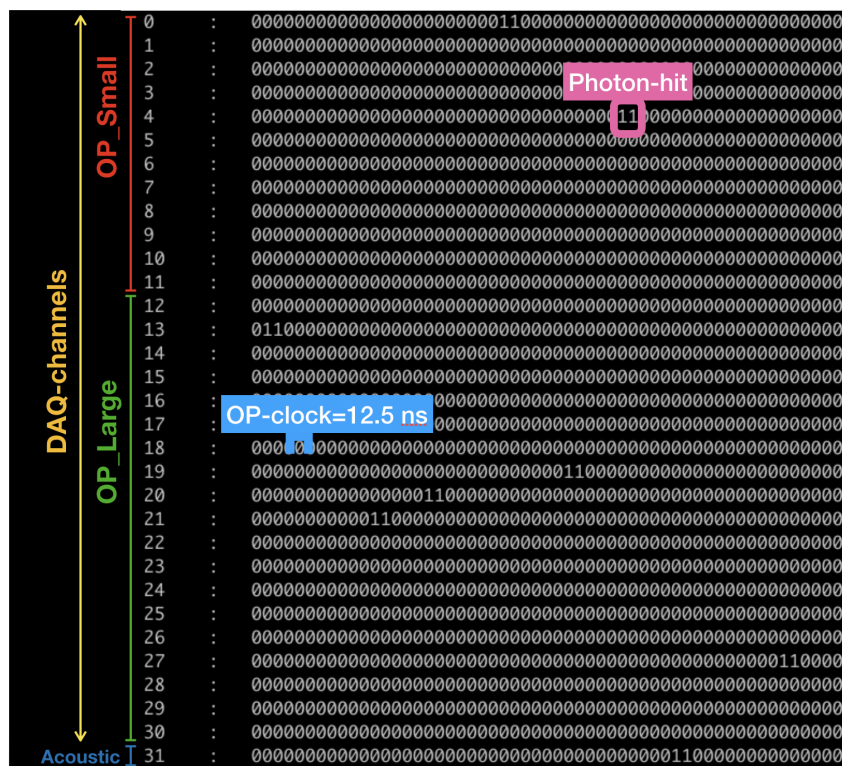


Figure 4.5: A page of the MIF file is shown, highlighting the division among the 31 PMTs channels between OctoPaes Small and Large.

memory location of 4096 rows, each of them representing a time window for the emulation of a signal on a single PMT or on one acoustic channel. The file is organised in pages, one for each DOM. A page is composed of 31 rows for the emulation of the photon hits

on the 31 PMTs inside the DOM itself, and another row for the emulation of the acoustic signal. In turn, each row contains 256 bits, each of them representing a time window of 12.5 ns, equal to the OctoPAES clock selected in the firmware, as summarised in Fig.4.5. In order to create a hit, we need simply to switch the bit (from 0 to 1) in the right location inside the row. Once created a hit, what we want to do is to correlate different hits within the same DOM, and between different DOMs, in order to recreate the precise time structure of a real event.

In order to justify the way we characterised the emulated hits by the OctoPAES, it is important to consider here the relevant requirements for good signals and the trigger conditions that are on-board the CLB and by the TriDAS DataFilter algorithms. So we need to recall the three implemented trigger levels: the L0 condition implemented in the TDC front-ends sets a threshold of 0.3 photo-electrons for the amplitude of the hit electrical pulse; although short duration pulses can be recorded, we decided to emulate hits with pulse duration over the threshold close to 26.5 ns, which is the expected time over threshold of a single photo-electron. In order to achieve this, a valid hit is obtained by concatenating two consecutive bits set to 1. At the same time, in the DataFilter process the L1 condition imposes the coincidence of two or more L0 hits inside the same DOM, within a time window of ~ 25 ns. In particular for this trigger condition properly configuring the filtering algorithms via the runsetups, it is possible to tune the constraint on the cosine of the angle between the directions of two hit PMTs. Finally, the L2 level trigger searches for correlations in between L1 triggered hits on different DOMs, and is just at this point where we had to calculate the physical delays between the arrival time of the photons on one DOM and on the adjacent ones. This delay is then translated into the nearest integer multiple of the OctoPAES clock, representing the distance, computed as number of bits, between two hits that must be placed in correspondence of adjacent DOMs-pages.

Our final purpose will be to finalise a dedicated firmware capable to implement a

state machine that injects a background page with a selected frequency of 5 kHz, and signal pages at 1 or 10 Hz. Since more hit patterns can be concatenated in the MIF file, the right signal page to be activated can be selected via a 12-bit address, whose Mean Significant Bits (MSBs) are defined by the corresponding configuration of a dip switch device mounted on the OctoPAES board. The above mentioned frequency values, for both background and signal, are chosen to approximate the ones measured in the KM3NeT/ARCA deployment site. The consequent *background page* in the MIF file was created inserting an hit (two consecutive bits=1) in a random location over the 256 bits in a row. The probability distribution of a hit over the 256 bits is assumed to be uniform, being the nature of this event completely deterministic and not poissonian ¹.

To keep the environment and the resulting data clean from spurious signals, we decide to not insert coincident hits originated from background, avoiding therefore to trigger the L1 condition. Another useful MIF page configuration was what we called the *calibration page*, in which only two coincident hits are inserted on channel 0 (OctoPAES Small) and on channel 12 (OctoPAES Large). Being in fact placed in the same location with respect to the starting point of the row, such hits satisfy the L1 condition. By measuring the time difference between the occurrence of L1 coincidences among the available CLBs, we were able to estimate the delays of one OctoPAES board respect to the others (see calibration section). Lastly, the *signal pages*, one for each DOM are computed according to the precise determination of the arrival time of the photons on different DOMs, considering the distribution of their arrival time in function of the string height (see eq.(3.7)).

¹In case of poissonian events, as the one measured in deployment sites, considering the single PMT rate of ~ 7 kHz (T_c the corresponding period), we can calculate the L1 rate in a TimeSlice (100 ms):

$$P = 2\nu^2 dt T_c \tag{4.1}$$

$$R_2 = 2\nu^2 T_c \quad \text{rate on two different PMTs} \tag{4.2}$$

$$R_{\text{DOM}}^{TS} = \frac{31!}{29!2!} R_2 \times 100ms \tag{4.3}$$

4.2.2 GUI for MIF creation

The creation of the MIF file was automatized thanks to a *Graphical User Interface* (GUI) that takes, as input, the physical parameters of the muon trajectory that we want to emulate and translates it in the MIF file.

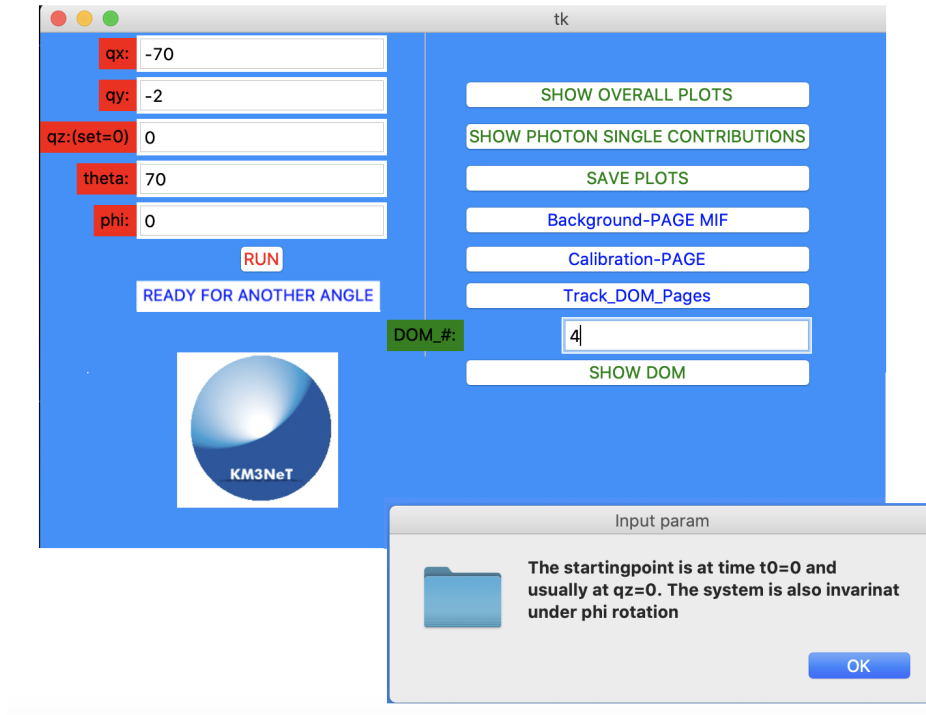


Figure 4.6: The window of the GUI for the MIF creation. Before accessing to the GUI itself a pop-up window (grey one) reminds users the starting conditions chosen for the further parameter insertion. The starting vector \vec{q} and the polar angles (θ and ϕ) defining the \vec{u} versor are required.

Considering the design of the final OctoPAES firmware, still to be finalised, the GUI offers however the possibility to create the first page as background, through *Background-PAGE MIF* button, with no L1 coincidences among the emulated hits, and the second page as calibration with *Calibration-PAGE* button. For both this type of pages, it was

chosen to create the same hit pattern for all the OctoPAES boards: this implies that the background hit signature will be the same on all the DOMs of the BCI DU. The remaining pages of the MIF file are dedicated to the hits which compose the signal events. Since a DU is made of 18 DOMs, which are hit by photons in different ways and at different times, each DOM has a dedicated page in the MIF file. This means that one entire neutrino event requires 18 pages to be completely described. We can see the screen of the GUI in Fig.4.6.

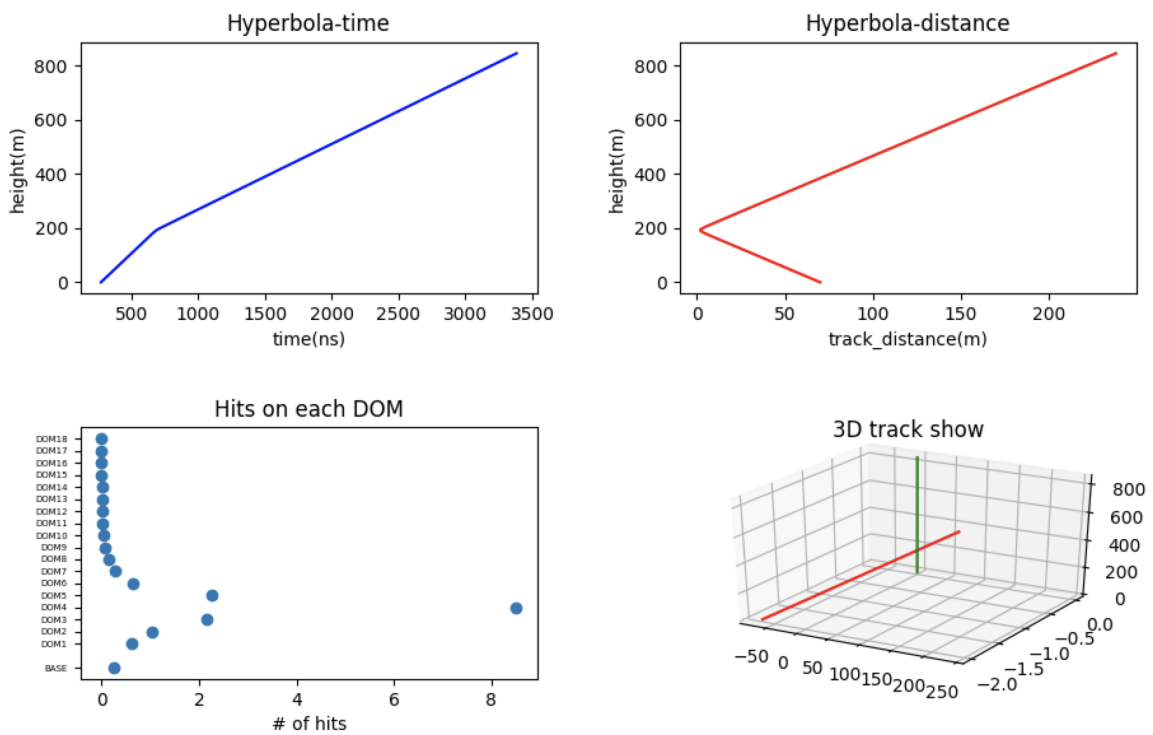


Figure 4.7: **Top-left:** z-t plane representing the hyperbola used to extrapolate the arrival time of the photons on DOMs; **top-right:** horizontal distance of the muon trajectory to the detector string placed in $(x,y) = (0,0)$ point; **down-left:** number of hits on single DOMs; **down-right:** a 3D representation of the muon track (red) and of the detector string (green).

From the input physical parameters of the muon trajectory to the LVDS pulses generated by the OctoPAES boards, we need to take into account many physical effects, above all, photon creation and propagation in water.

As the BCI setup reproduces one DU only, the choice of the starting point of each track, as well as its direction, are relevant parameters which affects the number of photons which can be detected by a DOM. Once the input physical parameters have been chosen, the *SHOW OVERALL PLOTS* button can be clicked, and some explanatory plots of the event pop up.

Fig.4.7 shows from left to right and from top to bottom respectively: the z-t plane, with the hyperbola through which the arrival time of the photons on DOMs is extrapolated, (see eq.3.7); the horizontal distance, calculated in x-y plane, of the track to the detector string, in function of the height of the string itself; the number of photon-hits generated on each DOM of the string and lastly a 3D representation of the track trajectory (in red) and of the detector string (in green).

As we can see from *Hyperbola-distance* graph, the point of closest approach of the track to the detector string is also the point at which the maximum number of photons is registered, producing what was called, in the previous chapter, the *hot spot*.

The distribution of the hit number on different DOMs was obtained taking into account the absorption of photons in the seawater, the PMT quantum efficiency and a geometrical acceptance factor. For what concerns absorption, the distance travelled by photons in function of the height of the string is calculated, as shown on the top of Fig.4.8.

No scattering effects are taken into account, and the quantum efficiency was assumed to be constant, over the optical wavelength, at a value of 30%. The acceptance factor was calculated considering the spherical geometry of the DOM, the photon production, following the Frank-Tamm formula integrated over optical wavelengths, producing the following result:

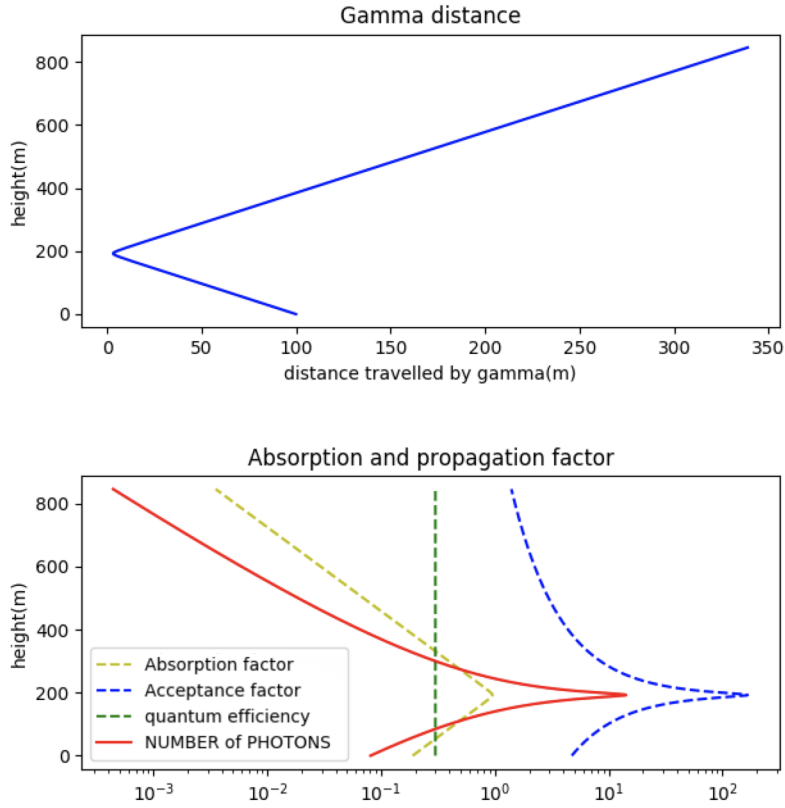


Figure 4.8: **top:** distance travelled by a photon from the emission point to the detector line; **bottom:** the effects taken into account for the photon propagation (absorption, geometrical acceptance, PMT quantum efficiency).

$$\int_{-R}^R \frac{475}{\pi} \sin^2(\theta_c) \cdot \sin^{-1} \left(\frac{(\sqrt{R^2 - h^2})}{\frac{d}{\sin(\theta_c)} + \cotg(\theta_c)h} \right) A_{\text{eff}} dh \quad (4.4)$$

where d is the horizontal distance of the track respect to the DOM, θ_c is the Cherenkov angle for ultra-relativistic particles in seawater, R is the DOM radius ($= 20.0$ cm) and A_{eff} is the effective area of the DOM, or the fraction of the PMT covered surface respect to the DOM surface (this last constant factor do not take into account the asymmetries in the PMT distribution over the DOM surface and neither the differences in the arrival direction of the photons).

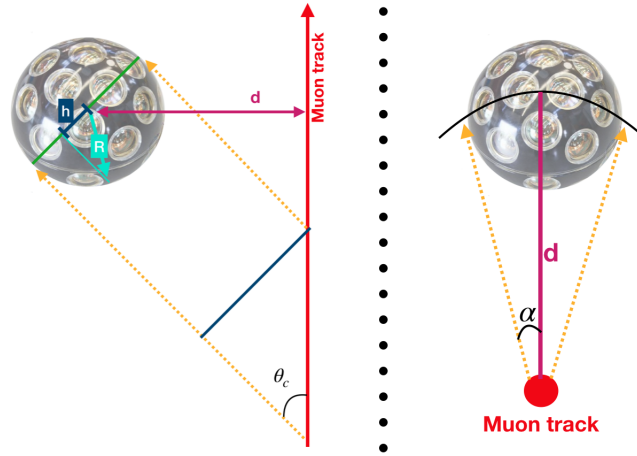


Figure 4.9: Schematic representation (left: side view, right: top view) of the geometrical parameters taken into account for the calculation of the acceptance factor, with the same notation used in eq.(4.4).

Once calculated the number of hits on each DOM, we need to select the right PMTs in order to provide the directional information gathered in the multi-PMT configuration. For doing this the generic photon vector was calculated, imposing the constraint $\vec{u} \cdot \vec{n}_\gamma(t_\gamma^1) = \cos\theta_c$, where \vec{u} is the track vector, and considering the single string placed in $(x,y)=(0,0)$:

$$\vec{n}_\gamma(t_\gamma^1) = \frac{1}{d_\gamma(z)}(-q_x - u_x ct_\gamma^1, -q_y - u_y ct_\gamma^1, z - q_z - u_x ct_\gamma^1) \quad (4.5)$$

with $t_\gamma^1(z)$ is the starting time of the photon:

$$t_\gamma^1(z) = \frac{1}{c}(zu_z - \vec{q} \cdot \vec{u} - \frac{d_\gamma(z)}{n}) = t_\gamma(z) - \frac{d_\gamma(z)n}{c} \quad (4.6)$$

where $t_\gamma(z)$ is given from eq. (3.7), representing the arrival time of the photon on DOM. As proof of the validity of the result of eq. (4.5), in fact we have verified that:

$$\vec{n}_\gamma(t_\gamma^1) \cdot \hat{k} = \cos(\theta_\gamma) \quad (4.7)$$

where $\cos(\theta_\gamma)$ is the one written in eq.(3.9), and $\hat{k} = (0, 0, 1)$ is the z versor. Once the photon versors, impinging on each of the 18 DOMS within the string, are obtained, it is computed their scalar product with each of the 31 versors representing the direction of each PMT in the DOM. These last versors are given by construction, as expressed in Table 4.1, where θ represents the azimuth angle rising from 0 at the DOM ‘north pole’ to 180 degrees at the DOM ‘south pole’, while ϕ defined as 0 along the positive x-axis and positively increasing when rotating from x-axis to y-axis. At this point we select the

Ch.	θ (rad)	ϕ (rad)	dx	dy	dz
22	3.142	0.0	0.0	0.0	-1.0
14	2.587	1.571	0.0	0.527	-0.850
19	2.587	0.524	0.456	0.263	-0.850
25	2.587	-0.524	0.456	-0.263	-0.850
24	2.587	-1.571	0.0	-0.527	-0.850
26	2.587	-2.618	-0.456	-0.263	-0.850
18	2.587	-3.665	-0.456	0.263	-0.850
13	2.159	1.047	0.416	0.720	-0.555
21	2.159	0.0	0.832	0.0	-0.555
29	2.159	-1.047	0.416	-0.720	-0.555
28	2.159	-2.094	-0.416	-0.720	-0.555
20	2.159	-3.142	-0.832	0.0	-0.555
17	2.159	-4.189	-0.416	0.720	-0.555
12	1.870	1.571	0.0	0.955	-0.295
15	1.870	0.524	0.827	0.478	-0.295
23	1.870	-0.524	0.827	-0.478	-0.295
30	1.870	-1.571	0.0	-0.955	-0.295
27	1.870	2.618	-0.827	-0.478	-0.295
16	1.870	-3.665	-0.827	0.478	-0.295

Ch.	θ (rad)	ϕ (rad)	dx	dy	dz
10	1.271	1.047	0.478	0.827	0.295
6	1.271	0.0	0.955	0.0	0.295
3	1.271	-1.047	0.478	-0.827	0.295
2	1.271	-2.094	-0.478	-0.827	0.295
1	1.271	-3.142	-0.955	0.0	0.295
11	1.271	-4.189	-0.478	0.827	0.295
9	0.982	1.571	0.0	0.832	0.555
8	0.982	0.524	0.720	0.416	0.555
4	0.982	-0.524	0.720	-0.416	0.555
0	0.982	-1.571	0.0	-0.832	0.555
5	0.982	-2.618	-0.720	-0.416	0.555
7	0.982	-3.665	-0.720	0.416	0.555

Table 4.1: DAQ channels and corresponding position on a sphere of unit radius given by zenith and azimuth angles (θ - ϕ), while dx, dy, dz represents the projection over the coordinate axis: **left** OctoPAES LARGE, **right** OctoPAES SMALL.

values of the cosine generated by the scalar product of the photon vector with the PMT-vectors in the interval $[-1, 0)$, in order to take only back to back vectors. Taking at this point the absolute value of the cosine, we choose the N PMTs-DAQ Channels generating the greatest scalar product with the photon vector, where N is equal to the number of photon hits calculated before for that precise DOM. Fig.4.10 shows the representation of the hit distribution over the 31 PMTs generated from the GUI on a selected DOM (DOM_# = 4). The hit distribution assumed as uniform over the PMTs in a DOM

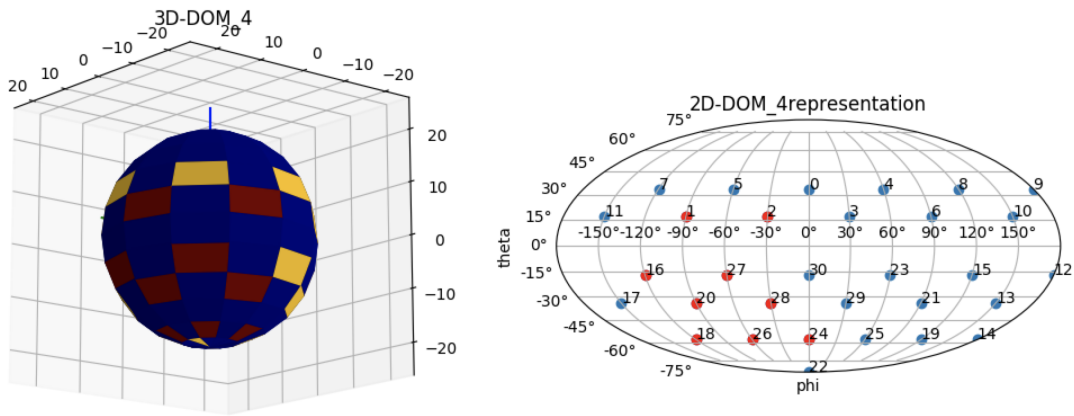


Figure 4.10: DOM representation in 3D and 2D, highlighting the hit PMTs. **Left:** 3D representation, with no hit PMTs (yellow) and selected hit PMTs (red); **right:** 2D representation of the DOM, with the θ angle shifted ($\theta \rightarrow 90 - \theta$) to fit the fixed plot range. Numbers in the plot are the corresponding DAQ Channel number.

is a quite important approximation, derived partially from: (i) the plot of Fig.4.11, showing a quite constant value of the relative collection efficiency in function of the sine of the incident angle, and (ii) studies and considerations derived from the modeling of the PMT response and consequent ToT generation when more hits occur simultaneously. The correlation of the number of photons impinging quite simultaneously on a PMT and

the consequent ToT generated is in fact a particularly difficult measurement due to the precise determination of the initial photon number.

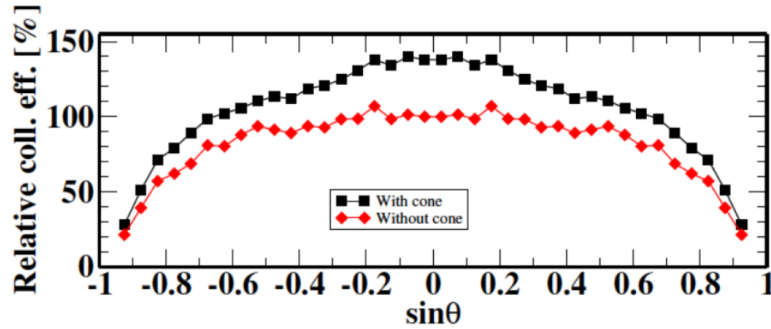


Figure 4.11: Relative collection efficiency in function of the sine of the incident angle respect to the PMT versor, with (black), and without expansion cone (red). Figure taken from [76].

4.2.3 Time calibration

The firmware development, and the consequent time calibration of the OctoPAES system, takes the majority of the efforts in order to achieve, in between the various boards of the experimental setup, a time delay of the order, at least, of tens of nanosecond. In fact, if we want to emulate a neutrino induced signal and to be able to detect the micro-OOS we need to have delays in the system less than or of the same order of magnitude of the micro-OOS itself. First of all it was chosen a MIF file in which all the channels of the OctoPAES boards (Large and Small) within a single CLB have coincident hits. In this way we assure that the delays between channels/PMTs on the same OctoPAES board, due to possible difference in the electrical connection in the pcb, are negligible as shown in Fig.4.12. The bimodal distribution shown was obtained measuring, over several timeslices, the mean of the difference between the hit-time sent by all the 31 channels (comprising OctoPAES Large and Small) and the hit-time of a reference channel, chosen

to be channel 5 on OctoPAES Small within the same CLB (channel 5S). The blue peak therefore is the mean of the delays of the channels on OctoPAES Small (same board respect to the chosen reference channel), while the red peak is the mean of the delays of the channels on the adjacent board (the OctoPAES Large), on the same CLB. The spread of each single peak is given by the quantization error on the time value given by the TDCs, of the order of ~ 1 ns. Once checked that the intra-OctoPAES delays were

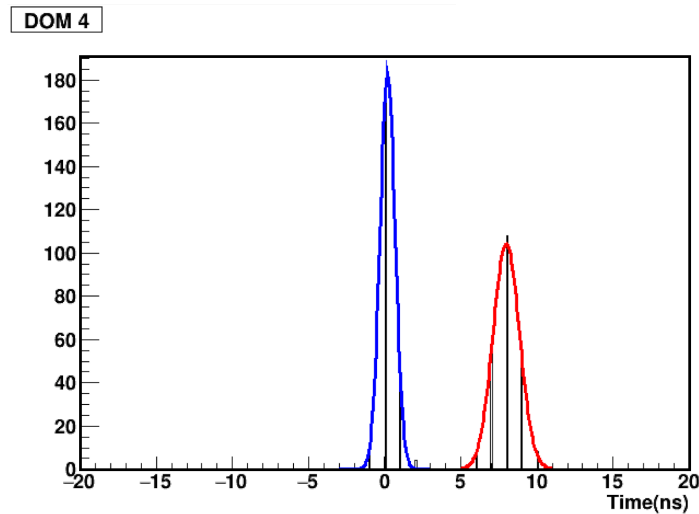


Figure 4.12: Mean of the delays of the hit time injected from the 31 channels, respect to the time of reference one (channel 5S) within a single DOM/CLB, with coincident hits generated by the two OctoPAES boards plugged on it. The spread of the peak is due to quantization error of the TDCs.

compatible with zero, we decided to generate a MIF file for the calibration in which only one channel per board send a hit, in order to keep DAQ system as free as possible from photon hits. For this reason the calibration page, created from the GUI, produced coincident hits on channel 0, on OctoPAES Small (0S) and on channel 12, on OctoPAES Large (12L).

Once the online program developed (see Section 3.4.2) registered each delay value for all the 36 OctoPAES boards, we included such information in the so-called *detector*

file, a file which reports the summary of the detector geometry and the time offsets to correct the synchronisation of each PMT.

CLB Number	OctoPAES type	Delay value (ns)	CLB Number	OctoPAES type	Delay value (ns)
CLB 1	Large	0 (the reference one)	CLB 10	Large	19
	Small	-5		Small	12
CLB 2	Large	19	CLB 11	Large	8
	Small	13		Small	14
CLB 3	Large	20	CLB 12	Large	9
	Small	15		Small	15
CLB 4	Large	10	CLB 13	Large	10
	Small	11		Small	15
CLB 5	Large	19	CLB 14	Large	11
	Small	15		Small	17
CLB 6 (not in use by now)	Large	-	CLB 15	Large	12
	Small	-		Small	18
CLB 7	Large	14	CLB 16	Large	12
	Small	15		Small	6
CLB 8	Large	11	CLB 17	Large	13
	Small	18		Small	8
CLB 9	Large	16	CLB 18	Large	16
	Small	11		Small	10

Table 4.2: OctoPAES delays measured respect to the OctoPAES Large on CLB 1, and inserted in the BCI detector file.

In the case of the BCI experimental setup, only time offsets for each PMT are reported as correction to be applied. For KM3NeT detectors additional information are added, such as the correction offsets for position and rotation of the various DOMs. The time delays measured and introduced in the BCI detector file are shown in Table.4.2. As we can see from Fig.4.13 taken from the online monitoring program that I developed, once the calibrations are inserted in the detector file, the delays between the various boards and the reference one reach the value of 0 or 1 ns. The fluctuation observed between these values is still due to the 1 ns error caused by the quantization time of the TDCs.

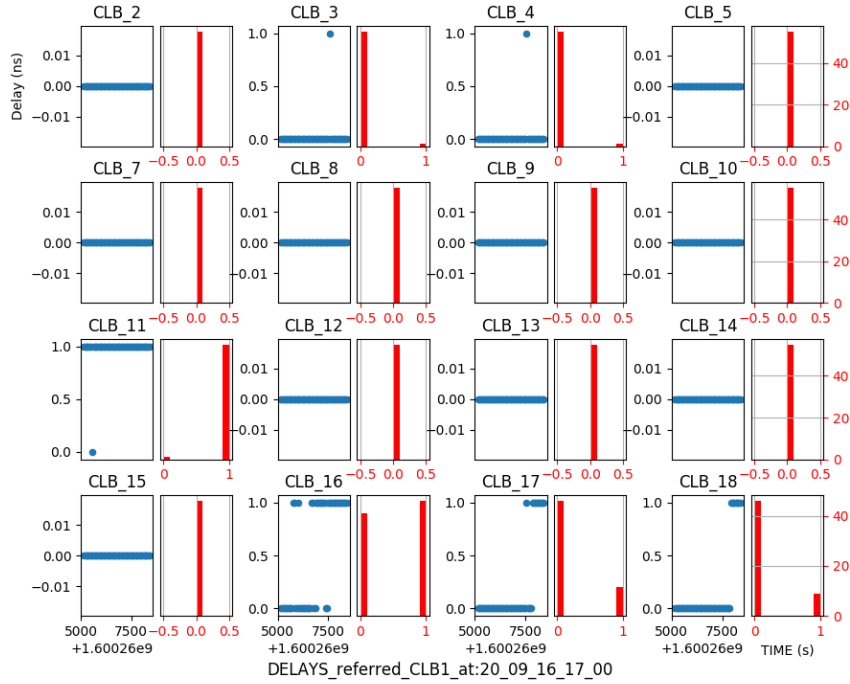


Figure 4.13: The plot originated from the online monitoring program developed, after the insertion of the time calibration in the BCI detector file. The fluctuations between 0 and 1 ns are due to the quantization time of the TDCs.

4.3 Characterisation of the micro-OOS issue at the BCI

The micro-OOS issue was the subject of a long observation campaign at the BCI. Previous tests, conducted both by Seven Solutions and on ARCA shore station, highlight the possible reason of the appearance of the micro-OOS, pointing towards the new version of the WRS custom firmware, based on v4.2. However the phenomenology and the precise cause of this problem was not yet identified. The tests conducted here at the BCI wanted to look for possible correlations between the appearance of the micro-OOS

and the number of active DOMs, or with the throughput of data injected in the DAQ system. Always 17 DOMs of the BCI string were used, in contrast with the single CLB-DOM configuration of the previous tests. In a first phase, the OctoPAES boards were configured with an injection frequency of 1 Hz and was selected the calibration page in the MIF file. The possible appearance of the micro-OOS of one or more CLBs, monitored through the Online Delay Display tool (see Section 3.4.2), can be observed as the shift back or forth of the delay value. Due to the fact that the micro-OOS seems to appear after three days of data-taking from the last power-cycle of the DU, the system is continuously monitored for more than three days. Fig.4.14 shows the monitoring program at the beginning of the observation period and after almost three days of continuous data-taking. With an injection frequency of 1 Hz, only 1 timeslice out of ten is filled with a photon hit and the DAQ system is not put particularly under stress: no micro-OOS was observed. Therefore it was decided to increase the injection frequency up to 1 kHz: in this configuration each timeslice has 100 hits and for each OctoPAES board the difference with the hit time array of the reference DOM was calculated, extracting, as usual, the central peak of the distribution. Also specific delay thresholds were set inside the online python program developed (50 ns, 100 ns, 1 μ s), in order to write on disk the entire time sequence of the hits in case of micro-OOS occurrence. Also with this frequency no micro-OOS was observed. Future tests could include a further increasing in the injection frequency, till 5, 10 kHz or even larger (after 20 kHz the DAQ system is protected with the *High-Rate Veto* condition, which makes the CLB to save only 2000 hits per PMT per timeslices, discarding the supplementary coming hits) or the possible increase of the active PMT/channels, passing from 2 on each DOM to more than 20. Eventually, a probing test would benefit the use of the ultimate firmware for the OctoPAES boards, which implements the combination of a high rate (≥ 5 kHz) uncorrelated background hits mixed to a low rate (1-10 Hz) of signal hits. This would closely approximate the real scenario where the micro-OOS issue was formerly discovered, with the ARCA DU.

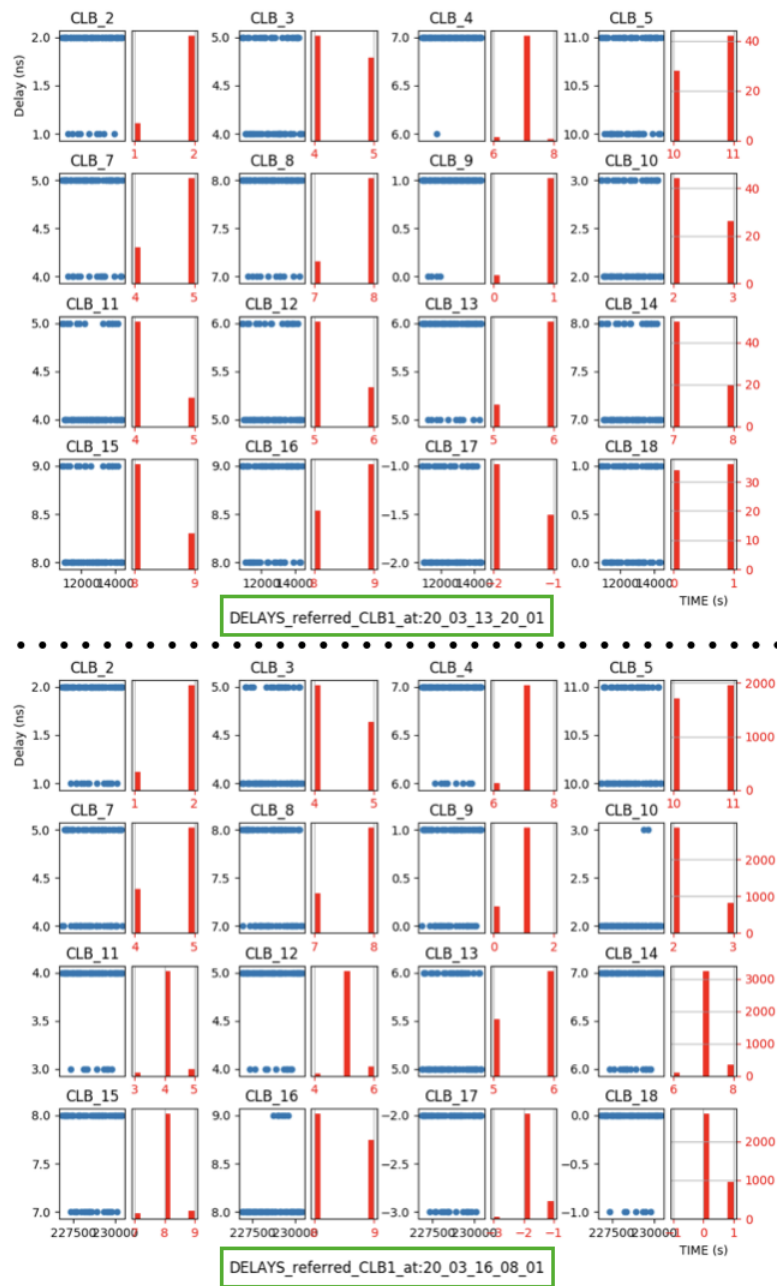


Figure 4.14: Online monitoring for the observation of the appearance of the micro-OOS issue. Delays computed for the OctoPAES Large boards respect to OctoPAES Large on CLB1.

4.4 Other developments: test with convolutional neural network

The BCI represents an ideal environment not only to develop and test new hardware solutions, but also for testing new software, developed by the collaboration, and to evaluate their performances. In the specific, a new framework for deep learning applications, based on Keras, was created in KM3NeT and is actually under development: OrcaSong and OrcaNet [77]. The first one is a project that pre-processes raw KM3NeT data transforming events in images, as shown in Fig.4.15, to be fed then to convolutional neural networks: it is among the most efficient algorithms and considered *de-facto* the standard Deep Learning approach for image classification (more on the architecture chosen and implemented in the next section).

OrcaSong is implemented within the KM3Pipe pipeline workflow [74]. In this context, the framework developed transforms the event raw data to N-dimensional histogram/greyscale image, where N is the number of features considered for each event. Only the hits involved in some trigger seed are considered, recording the PMT ID, its position (x, y, z) and the time of the hit t . Recent works released by the KM3NeT Collaboration show the reconstruction performance of these deep learning methods with respect to more standard ones, based on likelihood maximisation [78]. In this paper it was shown the possibility to perform a first step of classification between neutrino induced events and background, the latter considered here to be composed of both *downgoing* atmospheric muons and environmental random noise. They were also able to perform a classification on the neutrino-event topology, distinguishing between track-like and shower-like events. After these classification steps, further regression neural networks are applied on the resulting neutrino selected events in order to reconstruct the physical parameters like energy, direction (zenith angle) and position of the interaction vertex. My plan for this thesis was to try to adjust and use the same algorithm chain for analysing the data

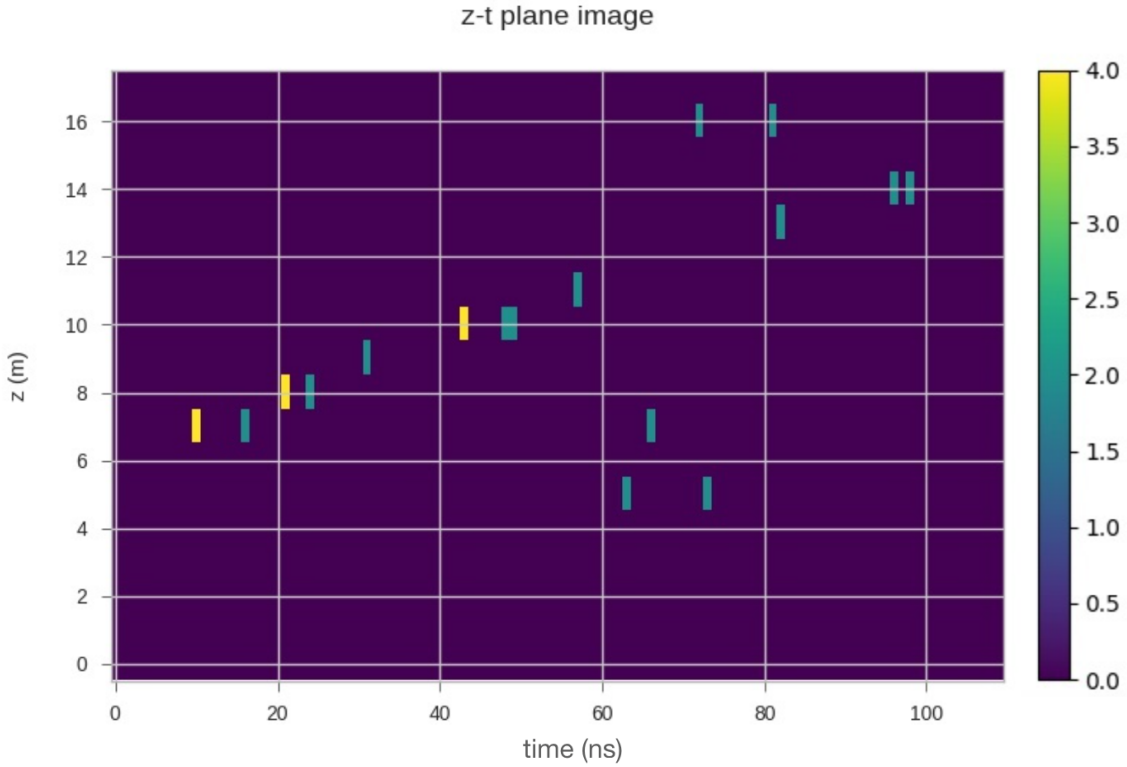


Figure 4.15: Event image (z-t plane) created from OrcaSong software, directly from triggered hits simulated in MonteCarlo production, in this case for ARCA-1. Considering the trigger selection efficiency, in the event we have both photon hits generated from neutrino-induced events, and also some background hits.

recorded at the BCI test-bench, as the muon hits that will be emulated, with the final version of the firmware, by the OctoPAES boards. The general idea was to start from a neutrino-background classifier and then perform a regression on the direction of the particle applying then it on the data injected by the OctoPAES system. The convolutional neural network algorithms were trained on Monte Carlo production made for KM3NeT/ARCA 1 (number indicating the detector configuration, in this case 1 DU), in order to have a detector configuration compliant to the one of the BCI. Looking at the physical properties of the simulated neutrino events, the energy and zenith distributions,

4.4. OTHER DEVELOPMENTS: TEST WITH CONVOLUTIONAL NEURAL NETWORK

as well as the x-y direction of the tracks, are shown in Fig.4.16.

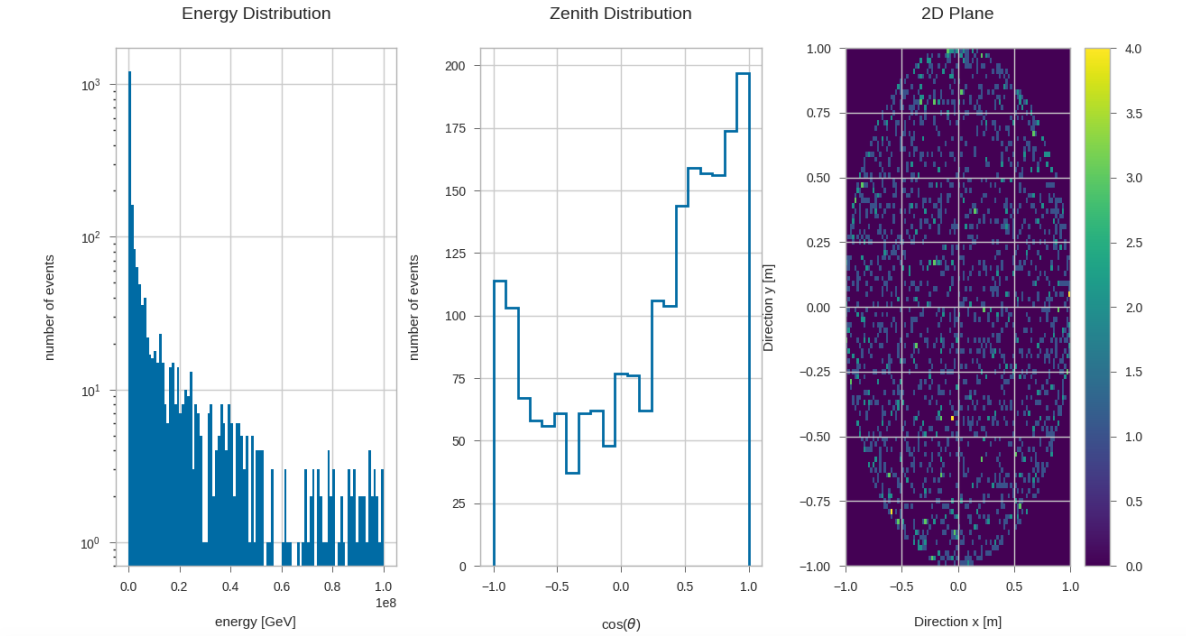


Figure 4.16: Monte Carlo distribution of reconstructed energy, zenith angle and x-y direction for neutrino events in ARCA-1 configuration.

A first trial was done trying to reproduce the classification tasks as in [78], between neutrino induced events and background. Considering the single string configuration of the detector, we have in the event signature a high number of symmetries. At the same time, some events were simulated far from the detector, producing very few photon-hits. Moreover we need to consider also the superposition, in the arrival direction of atmospheric muons and neutrinos coming from above and producing *downgoing* events, (no zenith cuts were performed on the data, following the same choice done in the previous article). Unfortunately, due to the very peculiar detector configuration the classification do not produce the expected results: in fact although attempted to fine-tune the hyperparameters of the designed network, the obtained separation accuracy was always about 50% for both the training and the validation sets. This is completely equivalent to a random picking between neutrino and background.

4.4.1 Regression on zenith angle for neutrino events

Considering the peculiar environment present in the BCI test-bench and the hits that can be emulated with the OctoPAES boards, combining into neutrino induced events and random noise, the latter with no coincidences to make not trigger the L1 condition, we are free from the need of performing a classification step before the possibility of applying a regression task on neutrino physical properties. This re-opened the opportunity to use and evaluate Deep-Learning applications to the BCI data. We in fact considered only neutrino events, generated in Monte Carlo production of ARCA-1, and appended a label dataset filled with the cosine of the zenith angle. The considered features, to take into account for the performance of the regression task, were the hit z position and its time of arrival on PMTs. In the single string configuration, always assumed to be represented according to the nominal vertical positions (i.e. it is not considered any distortion of the string line-shape due to the submarine currents), naturally $x - y$ dimensions are completely unnecessary. It was also evaluated the impact due to the finite horizontal extension of the PMT in the DOM, but it did not produce any significant improvements in the training stage; on the contrary, it increases only RAM and resource consumption. The data pre-processed in this way were then fed to chosen OrcaSong methods that binned the data and save the N-dimensional histogram in dedicated files. The optimal binning was found in previous works of KM3NeT collaboration. It resulted to be as follows: for the z dimension, 1 DOM per bin (therefore dividing the z -axis in 18 bins), and for the t dimension to reach 5-10 ns time resolution (as we can still see in Fig.4.15). The OrcaSong method returns also two important plots, reported in Fig.4.17, showing the distribution of the considered features for the overall events taken into account, with the chosen binning. As shown in Fig.4.17, on the left the hit density is quite uniformly distributed over the ~ 700 metres high of ARCA string, while on the right it is shown the time distribution of neutrino signal hits, relative to the mean time of the triggered

4.4. OTHER DEVELOPMENTS: TEST WITH CONVOLUTIONAL NEURAL NETWORK

hits calculated for each individual event. In fact, since the time range covered by the triggered hits is different for each event, it is defined relative to the mean time of the triggered hits for each event. The selection of a more restrictive time range for the hits,

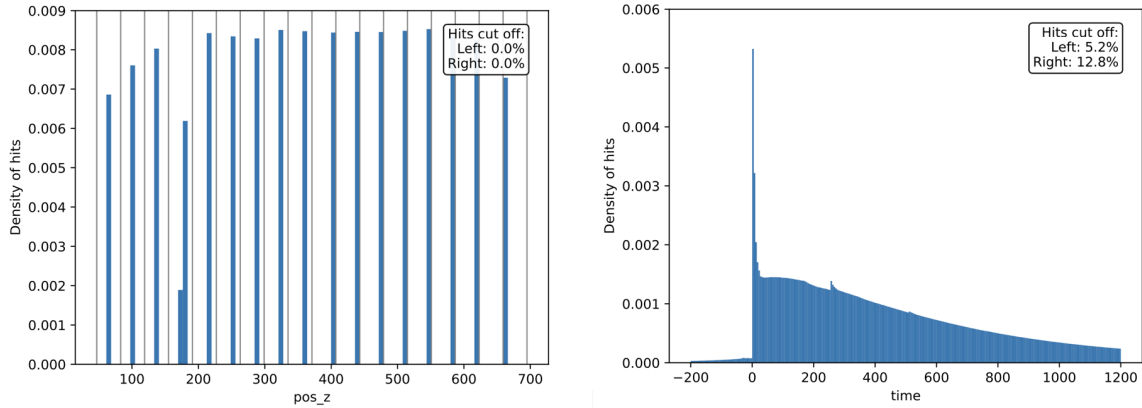


Figure 4.17: left: Distribution of the hit height of all the neutrino hits taken into account, with the same binning chosen for the image creation; **right:** hit time distribution respect to the mean of the triggered hit time for each event. Restricted time range to reduce the dimension of the image.

excluding, as shown on the right of Fig.4.17 in this case on *Right* $\sim 12.8\%$, is done in order to contain the dimensionality of the image and because most of the hits that lie outside the chosen time range are background or late scattered hits, bringing no relevant information. Finally, there were processed and binned around $1,5 \times 10^6$ neutrino events, and then fed to convolutional neural network. The architecture chosen is the one reported in Table 4.3, tuned after several trials and iterations. Particular attention was paid to select the most convenient activation function of the output layer. At first instance, I considered the softsign function, which is represented below, since it has an analytic expression :

$$f(x) = \frac{x}{1 + |x|}, \quad \in (-1, 1). \quad (4.8)$$

4.4. OTHER DEVELOPMENTS: TEST WITH CONVOLUTIONAL NEURAL NETWORK

Layer type	Properties
input layer	z-t images with dimension (18,280,1) (greyscale)
4× convolutional blocks	filters = 8, kernel size (3×3), padding = same, stride = 1
1× batch normalisation layer	
1× activation layer	activation function = relu
1× MaxPooling	filter = 2, stride = 1
1× dropout	dropout rate = 0.25
4× convolutional blocks	filters = 16, kernel size (5×5), padding = same, stride = 1
1× batch normalisation layer	
1× activation layer	activation function = relu
1× MaxPooling	filter = 2, stride = 1
1× dropout	dropout rate = 0.25
2× convolutional blocks	filters = 32, kernel size (7×7), padding = same, stride = 1
1× batch normalisation layer	
1× activation layer	activation function = relu
1× MaxPooling	filter = 2, stride = 1
1× dropout	dropout rate = 0.25
Flatten	
Dense	neurons = 64, activation function = relu
Dense	neurons = 32, activation function = relu
Dense	neurons = 1, activation function = softsign

Table 4.3: Architecture of the convolutional neural network obtained after several iterations.

The choice of the softsign function could be convenient, since its domain is limited in the range (-1,1), and very similar to the one of the cosine of the zenith angle, allowing to bound the output value of the network, avoiding therefore to generate non-physical

4.4. OTHER DEVELOPMENTS: TEST WITH CONVOLUTIONAL NEURAL NETWORK

estimates. From the other side, as it is shown in Fig.4.20, the softsign function introduced has some problems when modeling regions very close to -1 and/or +1. This difficulty is also due to the peculiar signature that track-like events, with $\cos(\text{zenith})$ near -1 or +1, will leave on a single string detector. The architecture chosen above, trained on $1,125 \times 10^6$ neutrino images, for 25 epochs, with a batch size equal to 32, produced the plot in Fig.4.18. The loss function used and reported was the ‘Mean Squared Error’ with ‘Adam’ optimizer. The network weights are saved in a hdf5 file in correspondence of

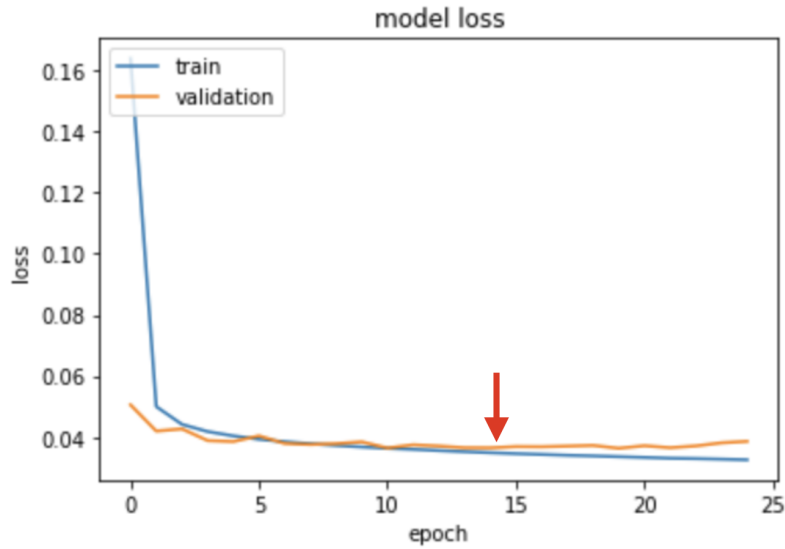


Figure 4.18: Train and validation loss registered at each epoch end. The network converge quite fast in the first epochs, while seems to start to overfit a little on the last epochs.

the minimum validation loss obtained during the training. At this point the model and the weights are used to produce a prediction on a subset of the images. The predictions obtained are shown in the plots of Fig.4.19, where on the left is reported a scatter plot of the predicted cosine of the zenith angle with respect to the real one, (note, only 500 events were plotted over the 100 000 predicted for graphical reasons), while on the right is shown a 2D histogram with all the 100 000 predicted events. The linear regression

4.4. OTHER DEVELOPMENTS: TEST WITH CONVOLUTIONAL NEURAL NETWORK

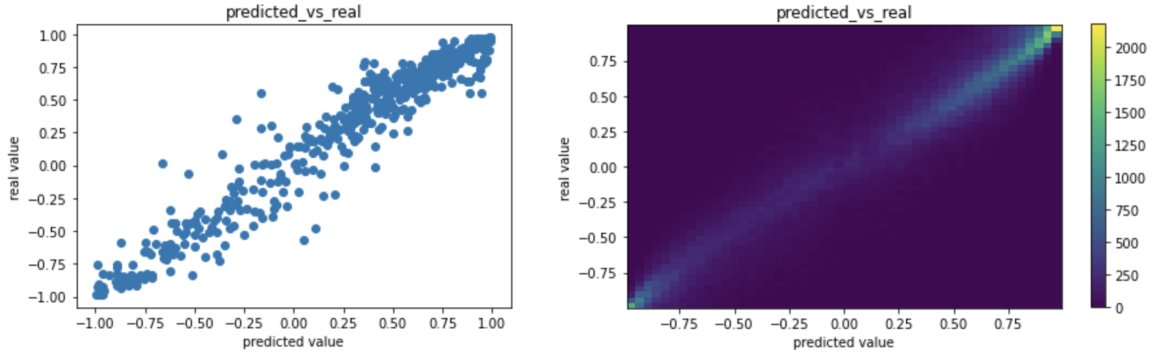


Figure 4.19: **left:** scatter plot showing 500 events, comparing the real values respect to the predicted cosine; **right:** 2D histogram collecting all the 100 000 predicted events respect to the corresponding ones.

produces a coefficient of:

$$R = 0.954 \pm 0.001 \quad (4.9)$$

At the same time, by making an histogram of the predicted cosine overlapped to the distribution of the real (Monte Carlo) values, as shown in Fig.4.20, we are able to calculate the reduced chisquare:

$$\tilde{\chi}^2 = \chi/NDF = 3041/199 = 15.28 \quad (4.10)$$

The code of the developed Deep Learning application is available from the the following GIT repository [79].

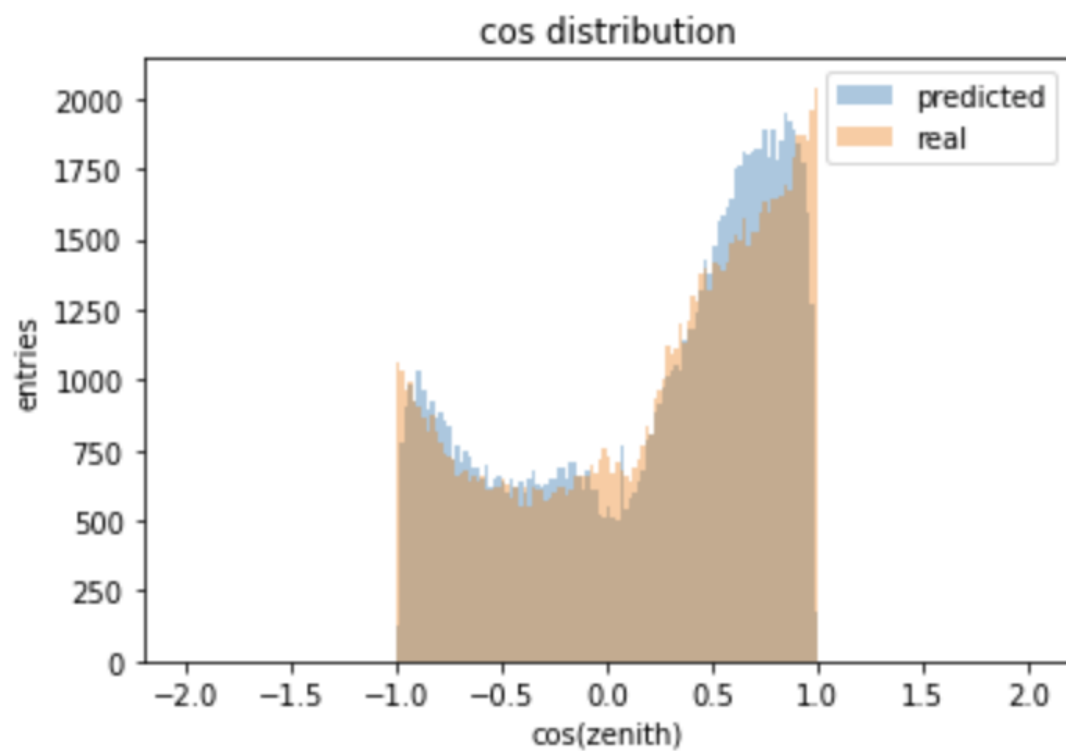


Figure 4.20: Distribution of the Monte Carlo cosine of zenith angle, called here real (in orange) and overlapped to the distribution obtained from the predicted values (in blue).

Conclusions

5.1 Summary

Many questions still remain unanswered in the field of CR physics and of astrophysical neutrinos. The construction or enlargement, in the next future, of neutrino telescopes will allow to measure neutrino fluxes and coincident signals with gravitational waves or γ -rays with a precision never had before, allowing to shed some light on the internal mechanisms of violent astrophysical phenomena. In the specific, KM3NeT detectors will be capable to detect a vast number of astrophysical neutrinos and to reach the angular resolution required to locate their sources in the sky. All the electronics and constructive elements of these detectors however, being placed at the bottom of the Mediterranean Sea, need to be developed and tested with high accuracy. The Bologna Common Infrastructure test-bench represents just a nodal stage for testing new hardware and software solutions for the electronic and data acquisition system of the telescope. In order to extend the possibilities and capabilities of the test-bench, the OctoPAES boards were constructed and developed. In fact, these boards offer the possibility to manipulate the payload on the system and to emulate the passage of particles as in a real detector. The principal objectives of this thesis were therefore the development and test of firmware and software solutions implemented for the OctoPAES system in the context of the BCI test-bench. Within this work, four different working versions of the firmware were produced, tested and validated, reaching important results in term of clock

stability and synchronisation over long periods. Thanks to these goals, the micro-OOS issue, the erratic apparent loss of synchronisation of the KM3NeT ARCA detector, likely due to some bug in the on-shore switching White Rabbit infrastructure, could be studied and an attempt was made in order to reproduce it. Even if an extended observational campaign was carried out for several weeks, varying each time some parameters in the data taking conditions, the micro-OOS never occurred in the BCI test-bench. However this allows us to expand the knowledge regarding this issue and to constraint the limits of its occurrence. A big part of the work was also centred on the study of the muon trigger algorithm, and on the event signature of track-like events on a single-string detector configuration. These studies were all focused on the creation of an important tool, the Graphical User Interface, capable to provide information and to reach, in the MIF file generation, the single PMT granularity. Lastly, a parallel development of reconstruction Deep Learning techniques was also undertaken, exploiting the framework developed by the KM3NeT collaboration. The convolutional neural network, trained on Monte Carlo files containing the hits producing the trigger of the events in a single string detector configuration, are capable to generate interesting results for what the regression of the cosine of the zenith angle of track-like events is concerned.

5.2 Outlook

In the next future important results can be achieved, finalising the development of the firmware v5 of the OctoPAES boards. This new development will allow to recreate, using the BCI DAQ system, the hit rates fully complaint to the KM3NeT/ARCA environment, including the emulation of muon signatures. At the same time, this achievement will allow to apply the trained neural network on track-like events originated from the OctoPAES boards and to compare its performances to more traditional reconstruction algorithms. The possibility to produce an online version of these Deep Learning

5.2. *OUTLOOK*

reconstruction algorithms, capable of a very fast regression on neutrino direction and fundamental in the multi-messenger scenario, is also under study.

Bibliography

- [1] W. Pauli. “The idea of the neutrino”. In: *Physics Today* 31.9 (1978), p. 23. DOI: <https://doi.org/10.1063/1.2995181>. URL: <https://physicstoday.scitation.org/doi/10.1063/1.2995181>.
- [2] C. L. Cowan et al. “Detection of the Free Neutrino: a Confirmation”. In: *Science* 124.3212 (1956), pp. 103–104. ISSN: 0036-8075. DOI: 10.1126/science.124.3212.103. eprint: <https://science.sciencemag.org/content/124/3212/103.full.pdf>. URL: <https://science.sciencemag.org/content/124/3212/103>.
- [3] G. Danby et al. “Observation of High-Energy Neutrino Reactions and the Existence of Two Kinds of Neutrinos”. In: *Phys. Rev. Lett.* 9 (1 July 1962), pp. 36–44. DOI: 10.1103/PhysRevLett.9.36. URL: <https://link.aps.org/doi/10.1103/PhysRevLett.9.36>.
- [4] K. Kodama et al. “Observation of tau neutrino interactions”. In: *Phys. Lett. B* 504 (2001), pp. 218–224. DOI: 10.1016/S0370-2693(01)00307-0. arXiv: [hep-ex/0012035](https://arxiv.org/abs/hep-ex/0012035).
- [5] Y. Fukuda et al. “Evidence for oscillation of atmospheric neutrinos”. In: *Phys. Rev. Lett.* 81 (1998), pp. 1562–1567. DOI: 10.1103/PhysRevLett.81.1562. arXiv: [hep-ex/9807003](https://arxiv.org/abs/hep-ex/9807003).
- [6] C.S. Wu et al. “Experimental Test of Parity Conservation in β Decay”. In: *Phys. Rev.* 105 (1957), pp. 1413–1414. DOI: 10.1103/PhysRev.105.1413.

- [7] L.H. Ryder. *QUANTUM FIELD THEORY*. Cambridge University Press, June 1996.
- [8] C.P. Burgess and G.D. Moore. *The standard model: A primer*. Cambridge University Press, Dec. 2006.
- [9] Daniel Ivan Scully. “Neutrino Induced Coherent Pion Production”. PhD thesis. Warwick U., 2013.
- [10] Raj Gandhi et al. “Neutrino interactions at ultrahigh energies”. In: *Phys. Rev. D* 58 (9 Sept. 1998), p. 093009. DOI: 10.1103/PhysRevD.58.093009. URL: <https://link.aps.org/doi/10.1103/PhysRevD.58.093009>.
- [11] J. Manczak. “Sensitivity of KM3NeT-ARCA detector to Glashow Resonance observation”. In: *36th International Cosmic Ray Conference (ICRC2019)*. Vol. 36. International Cosmic Ray Conference. July 2019, p. 955.
- [12] Carlo Giunti and Chung W. Kim. *Fundamentals of Neutrino Physics and Astrophysics*. Apr. 2007. ISBN: 978-0-19-850871-7.
- [13] B. Pontecorvo. “Neutrino Experiments and the Problem of Conservation of Leptonic Charge”. In: *Sov. Phys. JETP* 26 (1968), pp. 984–988.
- [14] Ziro Maki, Masami Nakagawa, and Shoichi Sakata. “Remarks on the unified model of elementary particles”. In: *Prog. Theor. Phys.* 28 (1962), pp. 870–880. DOI: 10.1143/PTP.28.870.
- [15] K. Abe, R. Akutsu, and A. et al. Ali. “Constraint on the matter–antimatter symmetry-violating phase in neutrino oscillations.” In: *Nature* 580 (2020), pp. 339–344. DOI: <https://doi.org/10.1038/s41586-020-2177-0>.
- [16] T. Chiarusi and M. Spurio. “High-Energy Astrophysics with Neutrino Telescopes”. In: *Eur. Phys. J. C* 65 (2010), pp. 649–701. DOI: 10.1140/epjc/s10052-009-1230-9.

- [17] Thomas K. Gaisser, Ralph Engel, and Elisa Resconi. *Cosmic Rays and Particle Physics*. 2nd ed. Cambridge University Press, 2016. DOI: 10.1017/CB09781139192194.
- [18] Maurizio Spurio. *Probes of Multimessenger Astrophysics: Charged cosmic rays, neutrinos, γ -rays and gravitational waves*. Springer, 2018. DOI: 10.1007/978-3-319-96854-4.
- [19] ENRICO Fermi. “On the Origin of the Cosmic Radiation”. In: *Phys. Rev.* 75 (8 Apr. 1949), pp. 1169–1174. DOI: 10.1103/PhysRev.75.1169. URL: <https://link.aps.org/doi/10.1103/PhysRev.75.1169>.
- [20] Ya. M. Khazan V. L. Ginzburg and V. S. Ptuskin. “Origin of cosmic rays: Galactic models with halo”. In: *Astrophysics and space science* 68 (1980), pp. 295–314. DOI: <https://doi.org/10.1007/BF00639701>.
- [21] G.T. Zatsepin and V.A. Kuzmin. “Upper limit of the spectrum of cosmic rays”. In: *JETP Lett.* 4 (1966), pp. 78–80.
- [22] Kenneth Greisen. “End to the cosmic ray spectrum?” In: *Phys. Rev. Lett.* 16 (1966), pp. 748–750. DOI: 10.1103/PhysRevLett.16.748.
- [23] A. Aab and P. et al Abreu. “Inferences on mass composition and tests of hadronic interactions from 0.3 to 100 EeV using the water-Cherenkov detectors of the Pierre Auger Observatory”. In: *Phys. Rev. D* 96 (12 Dec. 2017), p. 122003. DOI: 10.1103/PhysRevD.96.122003. URL: <https://link.aps.org/doi/10.1103/PhysRevD.96.122003>.
- [24] A. Abramowski et al H. Abdalla. “H.E.S.S. observations of RX J1713.7–3946 with improved angular and spectral resolution: Evidence for gamma-ray emission extending beyond the X-ray emitting shell”. In: *A&A* 612 (Apr. 2018). DOI: <https://doi.org/10.1051/0004-6361/201629790>.

- [25] B.P. Abbott et al. “Multi-messenger Observations of a Binary Neutron Star Merger”. In: *Astrophys. J. Lett.* 848.2 (2017), p. L12. DOI: 10.3847/2041-8213/aa91c9. arXiv: 1710.05833 [astro-ph.HE].
- [26] E Costa et al. “Discovery of an X-ray afterglow associated with the -ray burst of 28 February 1997”. In: *nature* 387 (June 1997), p. 783. DOI: 10.1038/42885.
- [27] V. S. Berezinsky and V. V. Volynsky. “Generation Function of High Energy Cosmic Neutrinos (i) Pp-Neutrinos”. In: *International Cosmic Ray Conference*. Vol. 10. International Cosmic Ray Conference. Jan. 1979, p. 326.
- [28] Andrea Palladino, Maurizio Spurio, and Francesco Vissani. “Neutrino Telescopes and High-Energy Cosmic Neutrinos”. In: *Universe* 6.2 (2020), p. 30. DOI: 10.3390/universe6020030. arXiv: 2009.01919 [astro-ph.HE].
- [29] E. Yen. “New Scaling Variable and Early Scaling in Single Particle Inclusive Distributions for Hadron-Hadron Collisions”. In: *Phys. Rev. D* 10 (1974), p. 836. DOI: 10.1103/PhysRevD.10.836.
- [30] Eli Waxman and John N. Bahcall. “High-energy neutrinos from astrophysical sources: An Upper bound”. In: *Phys. Rev. D* 59 (1999), p. 023002. DOI: 10.1103/PhysRevD.59.023002. arXiv: hep-ph/9807282.
- [31] M.G. Aartsen et al. “First observation of PeV-energy neutrinos with IceCube”. In: *Phys. Rev. Lett.* 111 (2013), p. 021103. DOI: 10.1103/PhysRevLett.111.021103. arXiv: 1304.5356 [astro-ph.HE].
- [32] M. G. Aartsen et al. “OBSERVATION AND CHARACTERIZATION OF A COSMIC MUON NEUTRINO FLUX FROM THE NORTHERN HEMISPHERE USING SIX YEARS OF ICECUBE DATA”. In: *The Astrophysical Journal* 833.1 (Dec. 2016), p. 3. ISSN: 1538-4357. DOI: 10.3847/0004-637x/833/1/3. URL: <http://dx.doi.org/10.3847/0004-637X/833/1/3>.

- [33] Markus Ahlers and Francis Halzen. “Opening a New Window onto the Universe with IceCube”. In: *Prog. Part. Nucl. Phys.* 102 (2018), pp. 73–88. DOI: 10.1016/j.pnpnp.2018.05.001. arXiv: 1805.11112 [astro-ph.HE].
- [34] R. Abbott et al. B. P. Abbott. “Observation of Gravitational Waves from a Binary Black Hole Merger”. In: *Phys. Rev. Lett.* 116 (6 Feb. 2016), p. 061102. DOI: 10.1103/PhysRevLett.116.061102. URL: <https://link.aps.org/doi/10.1103/PhysRevLett.116.061102>.
- [35] B. P. Abbott R. Abbott et al. “Multi-messenger Observations of a Binary Neutron Star Merger”. In: *The Astrophysical Journal* 848.2 (Oct. 2017), p. L12. DOI: 10.3847/2041-8213/aa91c9. URL: <https://doi.org/10.3847%5C%2F2041-8213%5C%2Faa91c9>.
- [36] A. Albert et al. “Search for High-energy Neutrinos from Binary Neutron Star Merger GW170817 with ANTARES, IceCube, and the Pierre Auger Observatory”. In: *The Astrophysical Journal* 850.2 (Nov. 2017), p. L35. DOI: 10.3847/2041-8213/aa9aed. URL: <https://doi.org/10.3847%5C%2F2041-8213%5C%2Faa9aed>.
- [37] Matteo Sanguineti and on collaborations on. “ANTARES and KM3NeT: The latest results of the neutrino telescopes in the Mediterranean”. In: *Universe* 5 (Feb. 2019), p. 65. DOI: 10.3390/universe5020065.
- [38] Riccardo Sturani. “Gravitational Waves and Neutrinos”. In: *Prospects in Neutrino Physics*. Apr. 2018, pp. 107–118. arXiv: 1804.03001 [hep-ph].
- [39] Maxim Dvornikov. “Neutrino oscillations in gravitational waves”. In: *J. Phys. Conf. Ser.* 1435.1 (2020), p. 012005. DOI: 10.1088/1742-6596/1435/1/012005. arXiv: 1910.01415 [hep-ph].
- [40] *On high energy neutrino physics. Proceedings, 10th International Conference on High-Energy Physics (ICHEP 60): Rochester, NY, USA, 25 Aug - 1 Sep 1960*. Rochester: U. Rochester, 1960, pp. 578–581.

- [41] *The New Window into the Universe*. URL: <https://www.phys.hawaii.edu/~dumand/pict/grieder/DUMAND.htm> (visited on 2020).
- [42] S. Barwick et al. “AMANDA: South pole neutrino detector”. In: *AIP Conf. Proc.* 272 (1993). Ed. by Y. Suzuki and K. Nakamura, pp. 1250–1253. DOI: 10.1063/1.43263.
- [43] *IceCube Explained*. URL: <https://icecube.wisc.edu/about/overview> (visited on 2020).
- [44] *Baikal-GVD home page*. URL: <https://baikalgvd.jinr.ru> (visited on 2020).
- [45] *ANTARES home page*. URL: <https://antares.in2p3.fr> (visited on 2020).
- [46] Agata Trovato. “Development of reconstruction algorithms for large volume neutrino telescopes and their application to the KM3NeT detector”. PhD thesis. Catania U., SSC, 2014.
- [47] Jannik Hofestädt. “Measuring the neutrino mass hierarchy with KM3NeT/ORCA”. In: *J. Phys. Conf. Ser.* 1342.1 (2020). Ed. by Ken Clark et al., p. 012028. DOI: 10.1088/1742-6596/1342/1/012028.
- [48] Chiara De Sio. “Event triggering and deep learning for particle identification in KM3NeT”. PhD thesis. Salerno U., 2018.
- [49] *KM3NET NEUTRINO TELESCOPE IN THE MEDITERRANEAN*. URL: <https://www.km3net.org> (visited on 2020).
- [50] A Margiotta. “Status of the KM3NeT project”. In: *Journal of Instrumentation* 9.04 (Apr. 2014), pp. C04020–C04020. DOI: 10.1088/1748-0221/9/04/c04020. URL: <https://doi.org/10.1088/1748-0221/9/04/c04020>.
- [51] *KM3NeT technical design report- Part3*. URL: <https://www.km3net.org/wp-content/uploads/2015/07/KM3NeT-TDR-Part3.pdf> (visited on 2020).

- [52] S. Adrian-Martinez et al. “Letter of intent for KM3NeT 2.0”. In: *J. Phys. G* 43.8 (2016), p. 084001. DOI: 10.1088/0954-3899/43/8/084001. arXiv: 1601.07459 [astro-ph.IM].
- [53] Karel Melis, Aart Heijboer, and Maarten de Jong. “KM3NeT/ARCA Event Reconstruction Algorithms”. In: *PoS ICRC2017* (2018), p. 950. DOI: 10.22323/1.301.0950.
- [54] M. De Jong. “KM3NeT: The Next Generation Neutrino Telescope”. In: *33th International Cosmic Ray Conference (ICRC2013)*. International Cosmic Ray Conference. 2013, p. 891.
- [55] M.G. Aartsen et al. “Measurement of Atmospheric Neutrino Oscillations at 6–56 GeV with IceCube DeepCore”. In: *Phys. Rev. Lett.* 120.7 (2018), p. 071801. DOI: 10.1103/PhysRevLett.120.071801. arXiv: 1707.07081 [hep-ex].
- [56] S. Adrián-Martínez et al. “Intrinsic limits on resolutions in muon- and electron-neutrino charged-current events in the KM3NeT/ORCA detector”. In: *JHEP* 05 (2017), p. 008. DOI: 10.1007/JHEP05(2017)008. arXiv: 1612.05621 [physics.ins-det].
- [57] M.G. Aartsen et al. “Evidence for High-Energy Extraterrestrial Neutrinos at the IceCube Detector”. In: *Science* 342 (2013), p. 1242856. DOI: 10.1126/science.1242856. arXiv: 1311.5238 [astro-ph.HE].
- [58] Y. Becherini et al. “A Parameterisation of single and multiple muons in the deep water or ice”. In: *Astropart. Phys.* 25 (2006), pp. 1–13. DOI: 10.1016/j.astropartphys.2005.10.005. arXiv: hep-ph/0507228.
- [59] Vivek Agrawal et al. “Atmospheric neutrino flux above 1 GeV”. In: *Phys. Rev. D* 53 (3 Feb. 1996), pp. 1314–1323. DOI: 10.1103/PhysRevD.53.1314. URL: <https://link.aps.org/doi/10.1103/PhysRevD.53.1314>.

- [60] Pellegrino, Carmelo and Chiarusi, Tommaso. “The Trigger and Data Acquisition System for the KM3NeT neutrino telescope”. In: *EPJ Web of Conferences* 116 (2016), p. 05005. DOI: 10.1051/epjconf/201611605005. URL: <https://doi.org/10.1051/epjconf/201611605005>.
- [61] *KM3NeT Data Acquisition and and Trigger System*. URL: <https://pos.sissa.it/358/848/pdf> (visited on 2020).
- [62] *SSC-The seven solution company*. URL: <http://sevensols.com> (visited on 2020).
- [63] S. Aiello et al. “The Control Unit of the KM3NeT Data Acquisition System”. In: *Computer Physics Communications* 256 (2020), p. 107433. ISSN: 0010-4655. DOI: <https://doi.org/10.1016/j.cpc.2020.107433>. URL: <http://www.sciencedirect.com/science/article/pii/S0010465520301909>.
- [64] T Chiarusi et al. “The Trigger and Data Acquisition System for the KM3NeT-Italy neutrino telescope”. In: *Journal of Physics: Conference Series* 898 (Oct. 2017), p. 032042. DOI: 10.1088/1742-6596/898/3/032042. URL: <https://doi.org/10.1088/1742-6596/898/3/032042>.
- [65] Tamas Gal. “Live monitoring and quasi-online event reconstruction for KM3NeT”. In: *EPJ Web Conf.* 116 (2016). Ed. by A. Capone et al., p. 05003. DOI: 10.1051/epjconf/201611605003.
- [66] E. Giorgio. “The Automatic Installation And Configuration Procedure for the data acquisition system of KM3NeT”. In: *36th International Cosmic Ray Conference (ICRC2019)*. International Cosmic Ray Conference. 2019, p. 898.
- [67] Tommaso Chiarusi et al. “The Software Defined Networks implementation for the KM3NeT networking infrastructure”. In: *PoS ICRC2017* (2018), p. 940. DOI: 10.22323/1.301.0940.
- [68] Paul Goransson Chuck Black Timothy Culver. *Software Defined Networks: A Comprehensive Approach*. 2nd ed. Elsevier, 2017. ISBN: 9780128045794.

- [69] Annarita Margiotta et al. “KM3NeT front-end and readout electronics system: hardware, firmware, and software”. In: *Journal of Astronomical Telescopes, Instruments, and Systems* 5 (Dec. 2019), p. 1. DOI: 10.1117/1.JATIS.5.4.046001.
- [70] K Georgakopoulou et al. “A 100 ps multi-time over threshold data acquisition system for cosmic ray detection”. In: *Measurement Science and Technology* 29.11 (Sept. 2018), p. 115001. DOI: 10.1088/1361-6501/aadc48. URL: <https://doi.org/10.1088/1361-6501/aadc48>.
- [71] J.A. Aguilar et al. “A fast algorithm for muon track reconstruction and its application to the ANTARES neutrino telescope”. In: *Astropart. Phys.* 34 (2011), pp. 652–662. DOI: 10.1016/j.astropartphys.2011.01.003. arXiv: 1105.4116 [astro-ph.IM].
- [72] Karel Melis, Aart Heijboer, and Maarten de Jong. “KM3NeT/ARCA Event Reconstruction Algorithms”. In: *PoS ICRC2017* (2018), p. 950. DOI: 10.22323/1.301.0950.
- [73] R. Mirani. “Parametrisation of em-showers in the antares detector-volume”. PhD thesis. Universiteit van Amsterdam, 2002.
- [74] *KM3PIPE*. 2020. URL: <https://km3py.pages.km3net.de/km3pipe/index.html> (visited on 2020).
- [75] *OOS_{live_m}* monitoring. 2020. URL: https://github.com/francescofilippini6/OOS_live_monitoring (visited on 2020).
- [76] S. Adrian-Martinez et al. “Expansion cone for the 3-inch PMTs of the KM3NeT optical modules”. In: *JINST* 8 (2013), T03006. DOI: 10.1088/1748-0221/8/03/T03006.
- [77] *OrcaSong: Preprocessing KM3NeT data for DL*. 2020. URL: <https://ml.pages.km3net.de/OrcaSong/> (visited on 2020).

BIBLIOGRAPHY

- [78] Sebastiano Aiello et al. “Event reconstruction for KM3NeT/ORCA using convolutional neural networks”. In: (Apr. 2020). arXiv: 2004.08254 [astro-ph.IM].
- [79] *Software_computer*. 2020. URL: https://github.com/francescofilippini6/Software_computer (visited on 2020).

Acknowledgements

First of all I would like to thank Prof.ssa Annarita Margiotta and Dr. Tommaso Chiarusi for always being present, for believing in me and for the infinite number of suggestions and advice. For the passion that drives them, and that they have been able to convey to me.

I would like to express my gratitude also to all the members of the ANTARES-KM3NeT Bologna group, for admitting me and for the constant encouragement and support.

A special thank goes also to Dr. Gabriele Balbi, of the Bologna INFN electronic section, for the patience and the availability always demonstrated.

To the BCI group, especially Dr. Emidio Giorgio of INFN-Laboratori Nazionali del Sud for the the many times he resolved the mistakes that I did in the laboratory.

I would like to make a special thanks to all my family for the constant support given, for making me feel free to follow my passions.

To Giorgia for the love demonstrated, despite the distance.

To my room mates and to all my friends.